Progress in Oceanography 159 (2017) 45–72

Contents lists available at ScienceDirect

Progress in Oceanography

journal homepage: www.elsevier.com/locate/pocean

Review

Uncertainties and applications of satellite-derived coastal water quality products

Guangming Zheng[a,b,*], Paul M. DiGiacomo[a]

[a] NOAA/NESDIS Center for Satellite Applications and Research, 5830 University Research Court, College Park, MD 20740, USA
[b] Global Science & Technology, Inc., 7855 Walker Drive, Suite 200, Greenbelt, MD 20770, USA

ARTICLE INFO

Keywords:
Light absorption
Light scattering
Light backscattering
Water-leaving radiance
Remote-sensing reflectance
Water quality
Pollutants
Pathogens
Chlorophyll
Suspended particles
Suspended sediment
Chromophoric dissolved organic matter

ABSTRACT

Recent and forthcoming launches of a plethora of ocean color radiometry sensors, coupled with increasingly adopted free and open data policies are expected to boost usage of satellite ocean color data and drive the demand to use these data in a quantitative and routine manner. Here we review factors that introduce uncertainties to various satellite-derived water quality products and recommend approaches to minimize the uncertainty of a specific product. We show that the regression relationships between remote-sensing reflectance and water turbidity (in terms of nephelometric units) established for different regions tend to converge and therefore it is plausible to develop a global satellite water turbidity product derived using a single algorithm. In contrast, solutions to derive suspended particulate matter concentration are much less generalizable; in one case it might be more accurate to estimate this parameter based on satellite-derived particulate backscattering coefficient, whereas in another the nonagal particulate absorption coefficient might be a better proxy. Regarding satellite-derived chlorophyll concentration, known to be subject to large uncertainties in coastal waters, studies summarized here clearly indicate that the accuracy of classical reflectance band-ratio algorithms depends largely on the contribution of phytoplankton to total light absorption coefficient as well as the degree of correlation between phytoplankton and the dominant nonalgal contributions. Our review also indicates that currently available satellite-derived water quality products are restricted to optically significant materials, whereas many users are interested in toxins, nutrients, pollutants, and pathogens. Presently, proxies or indicators for these constituents are inconsistently (and often incorrectly) developed and applied. Progress in this general direction will remain slow unless, (i) optical oceanographers and environmental scientists start collaborating more closely and make optical and environmental measurements in parallel, (ii) more efforts are devoted to identifying optical, ecological, and environmental forerunners of autochthonous water quality issues (e.g., onsite growth of pathogens), and, (iii) environmental processes associated with the source, transport, and transformation of allochthonous issues (e.g., transport of nutrients) are better understood. Accompanying these challenges, the need still exists to conduct fundamental research in satellite ocean color radiometry, including development of more robust atmospheric correction methods as well as inverse models for coastal regions where optical properties of both aerosols and hydrosols are complex.

1. Introduction

Coastal (marine, estuarine, and inland) zones are among the most important and valuable regions in the world from both an ecological and a socio-economic perspective. They are extremely productive, supplying living aquatic (e.g., fisheries; diverse benthic habitats) and other natural resources (e.g., oil, gas, minerals, and water). They are also hubs of commerce and transportation, and the most heavily populated and urbanized regions on earth. As such, coastal pollution is a significant and growing problem in both developed and developing nations. Contaminants such as oil, toxic chemicals, heavy metals, bacteria, viruses, nutrients, and sediments can adversely impact human health and coastal ecosystems and thus have significant environmental and socio-economic ramifications (e.g., Islam and Tanaka, 2004; IOCCG, 2008; Karydis and Kitsiou, 2013).

It can be difficult to identify sources of pollution in coastal zones, as well as monitoring and forecasting the subsequent fate, transport, and impacts of contaminants. In particular, coastal zones are interfacial regions where atmospheric, aquatic, and terrestrial domains converge (Karydis and Kitsiou, 2013) and are typically characterized by complex

* Corresponding author at: NOAA/NESDIS Center for Satellite Applications and Research, 5830 University Research Court, College Park, MD 20740, USA.
E-mail address: guangming.zheng@noaa.gov (G. Zheng).

http://dx.doi.org/10.1016/j.pocean.2017.08.007
Received 12 December 2016; Received in revised form 29 August 2017; Accepted 30 August 2017
Available online 01 September 2017

Nomenclature

Acronyms

AVIRIS	Airborne Visible/Infrared Imaging Spectrometer
CDOM	Chromophoric Dissolved Organic Matter
Chl-*a*	Chlorophyll-*a*
DOC	Dissolved Organic Carbon
EPA	Environmental Protection Agency
FIB	Fecal Indicator Bacteria
FNRU	Formazin Nephelometric Ratio Unit
FNU	Formazin Nephelometric Unit
GCOM-C	Global Change Observation Mission-Climate
GEO	Group on Earth Observations
GEOSS	Global Earth Observation System of Systems
GOCI	Geostationary Ocean Color Imager
HAB	Harmful Algal Bloom
HICO	Hyperspectral Imager for the Coastal Ocean
IOCCG	International Ocean Color Coordinating Group
IOP	Inherent Optical Property
ISO	International Organization for Standardization
JPSS	Joint Polar Satellite System
MAA	Mycosporine-like Amino Acid
MERIS	MEdium Resolution Imaging Spectrometer
MODIS	MODerate-resolution Imaging Spectroradiometer
MSI	Multi-Spectral Imager
NIR	Near-Infrared
NOMAD	NASA bio-Optical Marine Algorithm Dataset
NTRU	Nephelometric Turbidity Ratio Unit
NTU	Nephelometric Turbidity Unit
OCR	Ocean Color Radiometry
OLCI	Ocean and Land Color Instrument
OLI	Operational Land Imager
PACE	Plankton, Aerosol, Cloud, and ocean Ecosystem
PSU	practical salinity units
RGB	Red-Green-Blue (Image)
SAR	Synthetic Aperture Radar
SeaWiFS	Sea-viewing Wide Field-of-view Sensor
SeaBASS	SeaWiFS Bio-optical Archive and Storage System
SGLI	Second-generation GLobal Imager
SNR	Signal-to-Noise Ratio
SPF	Scattering phase function
SPM	Suspended Particulate Matter
SWIR	Shortwave Infrared
TOA	top of atmosphere
UV	Ultraviolet
VIIRS	Visible Infrared Imager Radiometer Suite

List of symbols

λ	wavelength of light in vacuum
a	total absorption coefficient of bulk water
a_d	absorption coefficient of organic detritus and heterotrophic microorganisms
a_g	absorption coefficient of CDOM
a_g^*	DOC-specific absorption coefficient of CDOM, $= a_g$/[DOC]
a_m	absorption coefficient of mineral particles
a_p	absorption coefficient of suspended particles
a_p^*	mass-specific absorption coefficient of suspended particles, $= a_p$/[SPM]
a_{ph}	absorption coefficient of phytoplankton
a_{ph}^*	chlorophyll-specific absorption coefficient of phytoplankton, $= a_{ph}$/[Chl-*a*]
a_w	absorption coefficient of pure water
b	total scattering coefficient of bulk water
b_b	total backscattering coefficient of bulk water
b_{bd}	backscattering coefficient of organic detritus and heterotrophic microorganisms
b_{bm}	backscattering coefficient of mineral particles
b_{bp}	backscattering coefficient of suspended particles
b_{bph}	backscattering coefficient of phytoplankton
b_{bw}	backscattering coefficient of pure water
b_p	total scattering coefficient of suspended particles
b_p^*	mass-specific scattering coefficient of suspended particles, $= b_p$/[SPM]
b_s	light side-scattering coefficient
b_w	total scattering coefficient of pure water
c	beam attenuation coefficient of bulk water
D	diameter parameter characterizing size of a particle
D_{V50}	median diameter of particle volume distribution
F_0	extraterrestrial solar irradiance
K_d	diffuse attenuation coefficient of downwelling irradiance
K_d^{tr}	minimum K_d of the water body within 410–665 nm
$\overline{K_d}$	average K_d within the first optical depth
L_{TOA}	radiance at top of atmosphere
L_u	upwelling radiance
L_w	water-leaving radiance
m	complex refractive index relative to water, $\equiv n + i\,n'$
n'	imaginary part of the refractive index relative to water
n	real part of the refractive index relative to water
nL_w	normalized water-leaving radiance
n_w	real refractive index of water
Q_a	single-particle absorption efficiency factor
Q_{bb}	single-particle backscattering efficiency factor
R_{rs}	remote-sensing reflectance just above water surface
r_{rs}	remote-sensing reflectance just below water surface
S_d	exponential-law spectral slope of nonalgal particulate absorption coefficient
S_g	exponential-law spectral slope of CDOM absorption coefficient
V	volume of a particle
γ	power-law spectral slope of backscattering coefficients
θ	scattering angle relative to the incident direction
θ'	underwater nadir angle of the upwelling radiance
θ_{sun}	solar zenith angle
σ_a	single-particle absorption cross section
σ_b	single-particle total scattering cross section
σ_{bb}	single-particle backscattering cross section
φ	azimuth angle of the upwelling radiance
ω_o	single-scattering albedo, $\equiv b/(a + b)$
ω_b	$\equiv b_b/(a + b_b)$

dynamics, including small-scale, ephemeral, and episodic processes and phenomena. Pollution inputs can be localized within one of these domains (e.g., an offshore oil spill that does not reach land) or else be transboundary in nature (e.g., urban or agricultural runoff discharged into an ocean or lake, or an offshore oil spill or sewage discharge transported onshore). Pollution sources can also be characterized as either "point" or "nonpoint" types. Point sources of pollution in the coastal environment are singular and localized and include discharge from a shore-based industrial or municipal wastewater treatment plant, or from a ship or other offshore structure (e.g., oil platform). Nonpoint sources of pollution in the coastal environment come from many diffuse sources and can include stormwater runoff as well as atmospheric deposition.

Remote sensing can be a valuable tool to identify or infer the presence of point- and nonpoint-source contaminants (natural and anthropogenic), and related processes and phenomena (e.g., runoff plumes, Harmful Algal Blooms (HABs)). The information obtained from remote-sensing data and products can help users such as managers and policy-makers assess, monitor, forecast, and mitigate coastal pollution and its impacts. Advantages provided by remotely sensed observations, particularly from space-based platforms, can include synoptic coverage from local to global scales, relatively frequent temporal revisits, extended time-series, consistent measurements, and the ability to observe a broad range of geophysical and biological/ecological parameters at a low cost (to the user). Conversely, remote-sensing platforms are unable to directly measure and quantify specific contaminants (e.g., pollutants and pathogens), to detect subsurface distributions, or to optically observe an area covered by clouds or fog. Further, spatial resolution and revisit frequency of remotely sensed observations can potentially be inadequate for certain applications or in some locales. As such, remote sensing does not supplant the need for *in situ* observations but rather serve as a complementary capability.

Remote sensing data can be obtained from multiple assets including satellite, sub-orbital (e.g., aircraft), and ground-based platforms. Satellites provide unique Earth observation capabilities for users because the cost and complexity of working with satellite data is often reduced given the significant infrastructure already implemented by space agencies and downstream data providers. This is often not the case for other platforms (e.g., sub-orbital). For example, flight operations are generally limited in duration, as is their spatial coverage, and as such their application for monitoring coastal water quality is presently infrequent and typically limited to dedicated, intensively coordinated field campaigns of significant events (e.g., in response to the Deepwater Horizon oil spill). Further, sub-orbital data acquisition can be a far more complex proposition for users in terms of dealing with operating costs and complexities in scheduling, weather, and flight logistics, as well as crucial data processing, calibration, and validation activities. Similarly, there are also significant costs associated with installation, operation, and maintenance of ground-based platforms.

Given the many advantages and benefits of space-based observations (i.e., global coverage, routine and sustained acquisitions from multiple platforms, free and open access to processed data), this review will focus on data products derived from satellite optical sensors. The use of optical satellite data for water quality monitoring, primarily Ocean Color Radiometry (OCR) or visible spectral radiometry, and the broader applications and societal benefits of OCR data have been detailed in previous reports (e.g., IOCCG, 2008) and papers (e.g., Mouw et al., 2015). Additionally, under the auspices of the Global Earth Observation System of Systems (GEOSS) being implemented by Group on Earth Observations (GEO), there is a GEO Water Quality Community of Practice (also known as *AquaWatch*) that has held several workshops to date and is now working to develop a global water quality observing and forecasting system for coastal and inland waters, which will be heavily reliant on OCR data (GEO, 2007, 2011; Dekker et al., 2015).

To date, satellite remote-sensing observations have frequently been utilized in more of an ad hoc and/or qualitative manner (e.g., the presence/absence or general location of a feature) for coastal pollution applications, but there is a burgeoning desire by coastal managers and decision-makers to obtain and utilize satellite-derived data for quantitative assessments on a routine and sustained basis (e.g., identifying trends over time, monitoring compliance with water quality standards). These efforts are being facilitated by the ever increasing availability of high-quality and fit-for-purpose OCR data.

The past several years have seen launches of the Visible Infrared Imager Radiometer Suite (VIIRS) on Suomi-NPP, the Operational Land Imager (OLI) on Landsat-8, the Multi-Spectral Imager (MSI) on Sentinel-2a and -2b, and the Ocean and Land Color Instrument (OLCI) on Sentinel-3a. Launches of the Sentinel-3b, and Joint Polar Satellite System (JPSS) platforms are forthcoming at the time of writing, as well as the Second-generation GLobal Imager (SGLI) on Global Change Observation Mission-Climate (GCOM-C), and the Plankton, Aerosol, Cloud, and ocean Ecosystem (PACE) mission. Collectively these sensors are ushering in a new era by exponentially increasing the availability of satellite data and derived products for use in water quality assessments, monitoring, and forecasting efforts. In addition, the free and open data policies that are increasingly being adopted globally, in accordance with GEOSS data sharing principles, are expected to boost the growth of OCR data usage across different user sectors, including academia, industry, resource management, and governments. Commercial products and services in particular are expected to flourish during this new era.

Given these burgeoning opportunities, a necessary task is to synthesize existing information and address knowledge gaps regarding uncertainties of different satellite water quality products. This will help ensure that a more informed decision can be made by users as to which product is best fit for their specific needs and applications. Several articles and reports have addressed various aspects of water color remote sensing for water quality applications (IOCCG, 2008; Matthews, 2011; Odermatt et al., 2012; Blondeau-Patissier et al., 2014; Mouw et al., 2015). However, the uncertainty aspect needs to be revisited in greater detail and from a mechanistic standpoint. In particular, users require a comprehensive primer that provides a stepwise progression of product generation and uncertainty accumulation across various levels of satellite data processing. This contribution addresses this need and makes recommendations to selecting appropriate satellite products for monitoring, assessing, and forecasting coastal water quality. While the approaches and information conveyed here are generally applicable also to inland waters, our primary focus here will be on the use and applications of OCR data in coastal marine and estuarine waters.

2. Existing and upcoming satellite ocean color radiometric sensors

Radiometric data in and around the visible spectral domain can be obtained from multiple satellite sensors. A summary on technical specifications of various sensors is provided by National Research Council (Yoder et al., 2011), and more details are available on the IOCCG website (http://ioccg.org) and in various IOCCG reports (e.g., IOCCG, 2012a). Most optical sensors are onboard polar-orbiting, sun-synchronous satellites positioned at an altitude of 700–850 km above sea level, such as the Sea-viewing Wide Field-of-view Sensor (SeaWiFS), MODerate-resolution Imaging Spectroradiometer (MODIS), MEdium Resolution Imaging Spectrometer (MERIS), VIIRS, OLCI, SGLI, PACE, OLI (on Landsat-8), and MSI (on Sentinel-2). These sensors provide global coverage with variable revisit frequency depending on latitude and size of swath. For example, VIIRS has the widest swath of ~3000 km and can revisit the same spot on the equator at least daily; whereas the swath size of OLI is only 185 km and its equatorial revisit frequency is every ~16 days. In contrast to low Earth orbits, geostationary satellites are fixed relative to the rotating earth at an orbit 35,786 km above sea level. They provide the most frequent sampling (up to one image every several minutes) but spatially are limited to a specific region, or field of view. To date Geostationary Ocean Color Imager (GOCI) is the only ocean color sensor positioned in geostationary orbit, which covers a 2500 km × 2500 km region centered at the Korean Peninsula (Choi et al., 2012). Further details on opportunities, requirements, and future plans for geostationary OCR is provided in IOCCG (2012b) Report #12.

There can be some important differences in spectral bands available on these OCR sensors. MODIS and VIIRS have shortwave infrared (SWIR) bands that enable more robust atmospheric corrections in turbid coastal waters (Wang and Shi, 2007; Wang et al., 2009b). MERIS has a 709 nm band that has proved useful in the study and monitoring of algal blooms under the premise that the algal light absorption coefficient approaches or surpasses that of pure water around the red absorption peak of chlorophyll (Gower et al., 2005, 2008). The band around 685 nm is important for detection of phytoplankton fluorescence (Gower and Borstad, 1990; Roesler and Perry, 1995; Gower et al.,

1999; Hu et al., 2005), which is available on MODIS and MERIS but not on SeaWiFS and VIIRS. The upcoming SGLI is designed with a 380-nm band which will support improved characterization of absorbing aerosols (Shi and Wang, 2007), Chromophoric Dissolved Organic Matter (CDOM) plumes (Wei and Lee, 2015) and phytoplankton containing Mycosporine-like Amino Acids (MAAs) (Kahru and Mitchell, 1998). Hyperspectral spectrometers such as Hyperspectral Imager for the Coastal Ocean (HICO) and the upcoming PACE can resolve subtle spectral features such as phytoplankton absorption peaks and shoulders associated with accessory pigments (Lucke et al., 2011).

Spatial resolution also varies with sensor and across bands for a given sensor. Specifically, SeaWiFS and PACE provide 1-km data at all bands. MODIS and VIIRS have similar resolutions (750–1000 m) and a few extra bands enabled with higher resolution (250–375 m). In comparison, MERIS, OLCI, and SGLI provide data at up to 250–300 m resolution across all their visible bands. The highest spatial resolution among openly and freely available satellite OCR data is enabled by sensors like OLI (Landsat-8) and MSI (Sentinel-2) at 10–30 m, with lower signal-to-noise ratio (SNR), reduced spectral coverage, and coarser spectral resolution. For example, a typical SNR at ~443 nm is 225 for Landsat-8 sensor (Irons et al., 2012) and 129 for Sentinel-2 sensor (Drusch et al., 2012), in comparison with an on-orbit SNR of 794 for SeaWiFS (Eplee et al., 2012), 1400 for MODIS-Aqua (Xiong and Barnes, 2003) and ~800 for VIIRS (Xiong et al., 2014). The bandwidths of individual visible-light channels of Landsat-8 and Sentinel-2 sensors are 20–75 nm, compared with 10–20 nm for the moderate-resolution sensors.

Despite all the aforementioned differences, all OCR sensors are positioned above the top of atmosphere (TOA) which is ~480 km above sea level and passively sense the sun-illuminated earth. Therefore OCR measurements are subject to influences from air molecules, aerosols, cloud, sun glint, and underwater bubbles which are unwanted from a water quality monitoring standpoint. Under favorable conditions these unwanted contributions can generally be accounted for, making it possible to derive water optical properties and water quality parameters. The most optically significant parameters widely used for water quality purposes include water turbidity and clarity, concentrations of suspended particulate matter (SPM) and Chlorophyll-*a* (Chl-*a*), phytoplankton fluorescence, the light absorption coefficient of CDOM, $a_g(\lambda)$, etc. These parameters can be used to infer presence of contaminants and pathogens that do not generate a direct optical effect. In Section 3, we review various sources of uncertainties introduced in the derivation of satellite water quality parameters.

3. Theories and observations for understanding uncertainties in satellite water quality parameters

The connectivity between directly measurable light signal and desired water quality parameters is subject to varying degrees of uncertainties. Conceptually we can categorize satellite-derived variables into different tiers based on how many uncertainty sources are associated with each variable, which is shown in Fig. 1. Variables in each tier have uncertainties accumulated from all tiers above. In other words, we expect generally least uncertainty in Tier-1 variables and most uncertainty in Tier-5 variables. Note that Fig. 1 holds regardless of what approach is used to derive a satellite water quality product, either via an Inherent Optical Property (IOP)-based inversion method that explicitly derives variables belonging to the intermediate tiers, or via a reflectance band-ratio algorithm that bypasses the intermediate variables. Below, we provide an overview of the uncertainties tier-by-tier.

3.1. Tier-1 to Tier-2: Deriving water-leaving radiance from sensor-level signal

Light signal detected from satellite sensor $L_{TOA}(\lambda)$, which itself is subject to instrument calibration errors, is attributable to multiple sources which may not be relevant to water quality assessment. The ultimately desired portion of signal is carried in the upwelling light that emerges from below the water surface and has not been reflected by the bottom, which is referred to as the water-leaving radiance $L_w(\lambda)$. Other

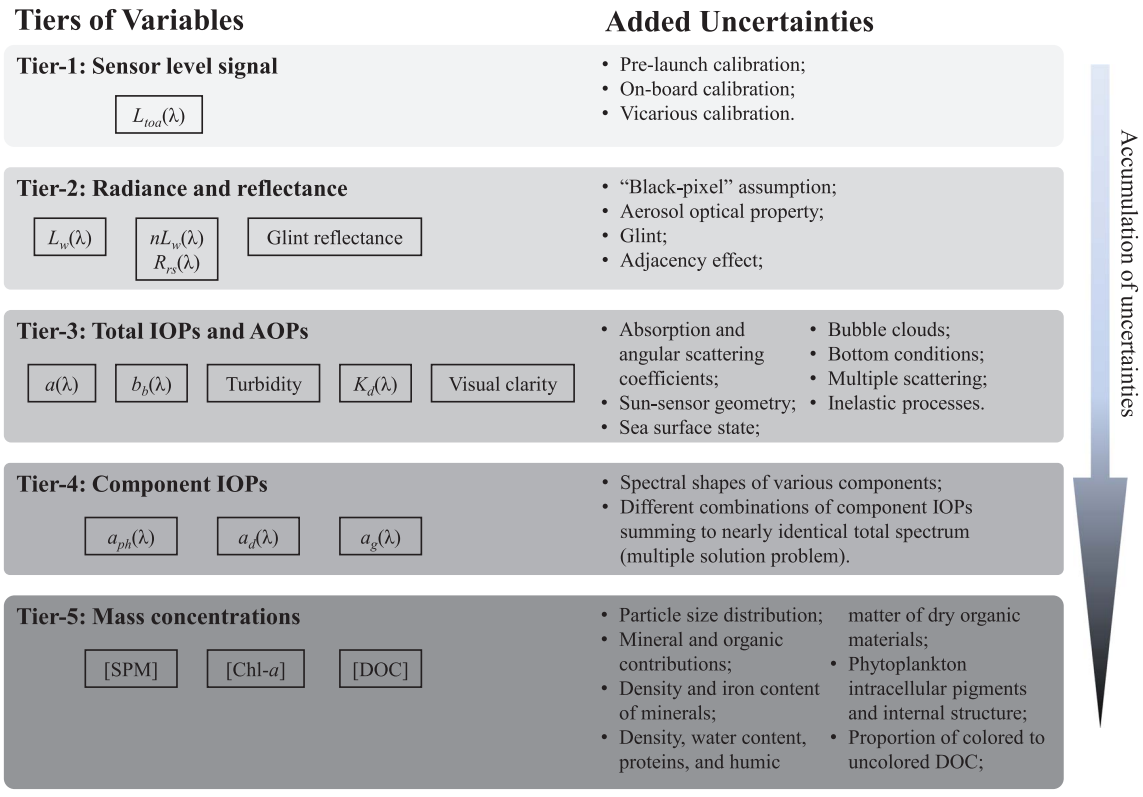

Fig. 1. Tiers of satellite-derived water quality parameters and associated uncertainties introduced at each tier.

portions of signal are generally unwanted for water quality assessment except for special cases such as oil spill detection and bottom type evaluation. The biggest portion comes from atmospheric molecules and aerosols which contribute ~90–99% to the total signal measured by satellite, depending on light wavelength and water brightness (IOCCG, 2010). Another source of noise arises from the direct reflection of light at the air-water interface, i.e., sun and sky glint, which can be used to detect changes of surface roughness caused by surfactants and oil slicks (Hu et al., 2009), but has nothing to do with optical properties of the water interior. Occasionally, underwater bubbles such as those in white caps and ship wakes can enhance $L_w(\lambda)$ through strong backscattering and weak absorption (Zhang et al., 1998; Stramski and Tegowski, 2001; Terrill et al., 2001). Finally, water pixels located in the vicinity of brighter surfaces such as land, ice, or clouds are subject to the so-called "adjacency effect", where light originated from brighter pixels is scattered into the field of view of neighboring water pixels.

The process of subtracting atmospheric, glint, and bubble contributions from satellite-measured $L_{TOA}(\lambda)$ is referred to as the "atmospheric correction" (Gordon and Wang, 1994; IOCCG, 2010). A detailed discussion about atmospheric correction theory and process has been made elsewhere (e.g., IOCCG, 2010) and is not included here. However, we note that atmospheric correction is one of the most challenging problems in satellite water quality remote sensing owing largely to the small water contribution to $L_{TOA}(\lambda)$. In addition, a particular difficulty in coastal and inland waters is the presence of absorbing aerosols such as dust, black carbon, and brown carbon. The presence of absorbing aerosols invalidates typical assumptions about the spectral shape of aerosol reflectance, which is critical to implementing atmospheric corrections that rely on spectral extrapolation of aerosol reflectance from the near-infrared (NIR) or SWIR bands to short wavelengths.

After applying atmospheric correction to $L_{TOA}(\lambda)$, the water-leaving radiance $L_w(\lambda)$ can be obtained. A commonly used variable in satellite OCR is the normalized water-leaving radiance, $nL_w(\lambda)$, which is essentially the $L_w(\lambda)$ one would get if the atmosphere were absent and the sun were directly overhead. The $nL_w(\lambda)$ is practically equivalent to satellite-derived $R_{rs}(\lambda)$ with the only difference being a factor of $F_0(\lambda)$. The $L_w(\lambda)$, $nL_w(\lambda)$, and $R_{rs}(\lambda)$ are subject to similar number of uncertainties sources and are considered Tier-2 variables here.

3.2. Tier-2 to Tier-3: Inverting $R_{rs}(\lambda)$ to derive total absorption and backscattering coefficients

Depending on light wavelength and water properties, $R_{rs}(\lambda)$ can be directly proportional to, inversely proportional to, or essentially invariant with the concentrations of optically significant substances in water, whereas IOPs like $a(\lambda)$ and $b_b(\lambda)$ always covary positively with their concentrations. Thus the remote detection of optically active substance generally boils down to the derivation of $a(\lambda)$ and $b_b(\lambda)$ from $R_{rs}(\lambda)$. Note that this step is still implicitly carried out even when an inverse model does not explicitly derives the IOPs. Like any inversion problem, the inversion of $R_{rs}(\lambda)$ is underconstrained, primarily because at most visible bands more output variables are desired than the number of given conditions. To derive $b_b(\lambda)$ and $a(\lambda)$, assumptions must be made about the magnitudes or spectral shapes of their components, which inevitably introduce uncertainties. In this section we review these uncertainties as well as variability of $R_{rs}(\lambda)$ caused by environmental factors as well as inelastic and multiple-scattering processes. Because of these uncertainties introduced in the derivation of $a(\lambda)$ and $b_b(\lambda)$, we categorize them as Tier-3 variables (Fig. 1). Influence of vertical inhomogeneity of IOPs on $R_{rs}(\lambda)$ is left out of this review for simplicity and readers are referred to studies made by Zaneveld (1982), Forget et al. (2001), Stramska and Stramski (2005), Kutser et al. (2008), and Yang et al. (2013).

3.2.1. Sun-sensor geometry

In this section we discuss angular variability of the upwelling light field below the water surface, $L_u(\theta', \theta_{sun}, \varphi, \lambda)$, which is the underwater counterpart of $L_w(\lambda)$, in the angular range that is relevant to satellite remote sensing. Standard operational satellite data processing software already addresses this variability but errors may still arise from departure of the actual angular shape of $L_u(\theta', \theta_{sun}, \varphi, \lambda)$ from model parameterization, especially for turbid waters with more variable particulate scattering.

For pixels in a satellite swath, θ' is 0 at nadir and increases towards the edge of swath. Taking into account both cross-track and along-track angular ranges, maximum above-water view angle is 51–59° (equivalent to $\theta' = 35$–$40°$) for SeaWiFS, MODIS, VIIRS, and SGLI, ~35° (equivalent to $\theta' = 25°$) for MERIS and OLCI, and 7.5–12° (equivalent to $\theta' = 6$–$9°$) for OLI (Landsat-8) and MSI (Sentinel-2).

Theoretical computations made for open ocean waters suggest that the angular variation of $L_u(\theta', \theta_{sun}, \varphi, \lambda)$ is bigger for larger θ_{sun}, greater range of θ', higher particulate scatter, and is spectrally dependent (Morel and Gentili, 1993, 1996; Morel et al., 2002). Let us consider the worst scenario in the case of moderate resolution sensors with maximum $\theta' = 40°$. Using a Petzold (1972) scattering phase function (SPF), Morel and Gentili (1996) show that the variability of $L_u(\theta', \theta_{sun}, \varphi, \lambda)$ within a 40°-cone centered around nadir is 10–75% for [Chl-a] = 0.03–3 mg m^{-3} and $\theta_{sun} = 0$–$75°$. Simulations made by Morel et al. (2002) using theoretical SPFs calculated for various sized spheroids suggest that this variability is about 0–100% for [Chl-a] = 0.03–10 mg m^{-3} (same θ_{sun} range). Park and Ruddick (2005) show a much smaller variability of ~12% ([Chl-a] = 0.3–3 mg m^{-3}, Fournier and Forand (1994) SPFs), largely owing to the relatively small θ_{sun} (30°) used in their simulations.

In situ measurements of angular distribution of upwelling light field near surface are consistent with theoretical simulations. In a clear-water lake, measurements made by Tyler (1958) with $\theta_{sun} = 56.6°$ show that the total $L_u(\theta', \theta_{sun}, \varphi, \lambda)$ integrated across the spectral range of 430–546 nm varies by ~40% within the 40°-cone. In subtropical Pacific, a single snapshot in the blue spectral range made by Voss et al. (2007) with [Chl-a] = 0.11 mg m^{-3} shows a 20% variability within the 40°-cone (θ_{sun} unspecified). Field measurements of bidirectional variability in the angular range defined by the 40°-cone are not available at other geographical locations, although variability within larger angular ranges is reported in a few studies (Gleason et al., 2012; Antoine et al., 2013). For example, within the Snell cone (defined by the critical angle, 48.5°) $L_u(\theta', \theta_{sun}, \varphi, \lambda)$ at 406–560 nm varies by 40–50% in clear waters in the Mediterranean Sea with $\theta_{sun} = 7.4°$, and by 50–70% in clear waters in the Beaufort Sea with $\theta_{sun} = 60.5°$ (Antoine et al., 2013).

In situ observations also suggest that variability of $L_u(\theta', \theta_{sun}, \varphi, \lambda)$ is likely to be higher in turbid waters compared with clear waters. *In situ* data obtained in coastal waters in the Rhone River plume in the Mediterranean Sea show that $L_u(\theta', \theta_{sun}, \varphi, \lambda)$ varies by 100–140% within the entire Snell cone, which approximately doubles the variability in clear waters (Antoine et al., 2013). Similarly, the variability is ~200% within a 45°-cone in the Chesapeake Bay, New York Bight, and Monterey Bay, which is also around twice its variability in clear waters in the Pacific Ocean and the Ligurian Sea (Gleason et al., 2012).

3.2.2. Bottom boundary conditions

The magnitude of $R_{rs}(\lambda)$ can also be affected by light reflected from bottom of water if water is sufficiently clear and shallow. A rule of thumb to determine whether the water bottom is visible to the satellite at a given wavelength is to assess the value of the first optical depth, $1/\overline{K_d}(\lambda)$, above which 90% of the diffusely reflected light originates (Gordon and McCluney, 1975). If the actual water depth is deeper than $1/\overline{K_d}(\lambda)$, a negligible contribution (< 10%) from bottom reflection can be expected in satellite-derived $R_{rs}(\lambda)$; otherwise the water should be treated as optically shallow and both bottom and water column contributions must be taken into account, e.g., using algorithms given by Lee et al. (1998) and Mobley et al. (2005). In this case the uncertainty in satellite-derived water properties is expected to increase but it is now

possible to remotely assess benthic habitats such as seagrass beds and coral reefs (e.g., Dierssen et al., 2003; Mobley et al., 2005) and estimate bathymetry. Note that the same location can be optically shallow or deep depending on water turbidity even without a change in water depth.

3.2.3. Inelastic processes

Spectral $R_{rs}(\lambda)$ is driven by both elastic and inelastic processes but the derivation of IOPs is based only on the elastic fraction. Inelastic signals are contributed by water Raman scattering, phytoplankton fluorescence, and CDOM fluorescence. Their contributions to $R_{rs}(\lambda)$ are difficult to quantify, which depend on spectral distribution of incident solar irradiance, elastic absorption and scattering properties of the bulk water, wavelengths of excitation and emission, optical properties of the substance that produces the inelastic effect, and efficiency of the inelastic process (~quantum yield) (Mobley, 1994; Babin et al., 1996; Gordon, 1999; Morel et al., 2002).

Raman scattering is characterized by a frequency shift (ranging within 3100–3700 cm^{-1} for water molecules) in scattered photon compared with the incident photon regardless of incident wavelength (Waters, 1995). Roughly one in ten photons scattered by water molecules are Raman-scattered to another wavelength (Mobley, 1994). The impact of Raman scattering on $R_{rs}(\lambda)$ is significant in clear waters (< 10% in the blue, and ~15% at > 470 nm (Gordon, 1999)) but can be accounted for using empirical approaches (Lee et al., 2013; Westberry et al., 2013). Raman scattering is typically negligible across the visible spectrum in turbid waters because elastic scattering by suspended particles dwarfs all molecular scattering (Morel et al., 2002), and strong absorption by CDOM and suspended particles depletes photons at the excitation wavelengths.

Phytoplankton and CDOM fluorescence can significantly affect certain parts of the $R_{rs}(\lambda)$ spectrum despite the low probability of these inelastic processes, e.g., 1–5% for chlorophyll fluorescence (Gordon, 1979; Mobley, 1994), and 0.5–1.5% for CDOM fluorescence (Mobley, 1994). This is because the emission wavelength of pure substance excited by any incident light is fixed within a small spectral range, creating a concentrating effect where light energy captured across the UV–visible spectrum is focused onto a narrow band in the form of fluorescence.

Phytoplankton pigments are groups of chemically similar substances and their fluorescence can introduce peaks to $R_{rs}(\lambda)$ spectrum. For example, spectral features near 683–710 nm in the $R_{rs}(\lambda)$ spectrum associated with chlorophyll fluorescence have been used to detect phytoplankton blooms in open oceans (e.g., Neville and Gower, 1977; Hu et al., 2015) and coastal waters (e.g., Gower et al., 2005; Hu et al., 2005). However, the contribution of chlorophyll fluorescence to $R_{rs}(\lambda)$ can be diminished by competition from elastic particulate scattering and/or non-phytoplankton absorption at the excitation wavelengths of chlorophyll fluorescence (Gilerson et al., 2007; McKee et al., 2007b).

The fluorescence of CDOM is spectrally broad owing to its chemical diversity. Across the visible spectrum, CDOM fluorescence contributes the most to $R_{rs}(\lambda)$ at the green portion (Hawes et al., 1992; Mobley, 1994; Huot et al., 2007), reported to be 6.5–8.5% in the Golf of Mexico (Hawes et al., 1992) and 10–20% in the CDOM-dominated Lunenburg Bay, Canada (Huot et al., 2007). Low contributions in the blue portion are associated with the shortage of solar UV irradiance which serves as the excitation source (Mobley, 1994). Lower contributions towards longer wavelengths are associated with the fast spectral decay of CDOM absorption coefficient because a photon must first be absorbed before it can be emitted as fluorescence.

3.2.4. Multiple-scattering effect

Whereas the desired $a(\lambda)$ and $b_b(\lambda)$ are single-scattering properties, in coastal and inland waters $R_{rs}(\lambda)$ is contributed predominantly by multiple-scattered photons. Single scattering dominates only within a top layer on the order of $1/4c(\lambda)$ thick (Jonasz and Fournier, 2011) considering that water-leaving photons have to complete a round trip in and out of the water. As a rule of thumb, this layer is < 7% of the first optical depth, calculated using the formula $\overline{K_d}(\lambda) = \sqrt{a(\lambda)[a(\lambda) + 0.255b(\lambda)]}$ (Kirk, 1984) and $\omega_0(\lambda) > 0.8$ for natural suspended particles (Babin et al., 2003a; Stramski et al., 2007, 2015). Monte Carlo simulations by Chami et al. (2006) show that the majority of remote-sensing signal is contributed by multiple-scattered light even for clear waters with the b_b:a ratio as low as ~0.03; in most turbid waters, up to ~94% of $R_{rs}(\lambda)$ is contributed by multiple scattering.

Multiple scattering introduces nonlinearity to the relationship between $R_{rs}(\lambda)$ and the ratio of $b_b/(a + b_b)$, hereafter $\omega_b(\lambda)$, but the nonlinear relationship between $r_{rs}(\lambda)$ and $\omega_b(\lambda)$ appears to be robust for a broad range of water properties, where $r_{rs}(\lambda)$ stands for the counterpart of $R_{rs}(\lambda)$ just below surface. For clear and moderately turbid waters ($\omega_b(\lambda) < \sim 0.2$), Gordon et al. (1988) suggest that a quadratic function in the form of $r_{rs}(\lambda) = g_1\,\omega_b(\lambda) + g_2\,\omega_b(\lambda)^2$ can be used to describe this nonlinear relationship, where g_1 and g_2 are coefficients determined based on Monte Carlo simulations at various Sun angles and using an oceanic-coastal mean particulate SPF reported by Petzold (1972) (personal communications with H. R. Gordon). The regression formulas obtained by Jerome et al. (1996) and Lee et al. (1999) based on similar simulations agree with that of Gordon's within ~12% for $\omega_b(\lambda) < 0.2$. Radiative transfer simulations made by Morel et al. (2002) and Park and Ruddick (2005) based on theoretical SPFs confirm the low variability in the $r_{rs}(\lambda)$-vs-$\omega_b(\lambda)$ relationship in this $\omega_b(\lambda)$ range. However, for larger $\omega_b(\lambda)$ values, these $r_{rs}(\lambda)$-vs-$\omega_b(\lambda)$ formulas tend to diverge, subjecting the inversion of $r_{rs}(\lambda)$ for $a(\lambda)$ and $b_b(\lambda)$ to significantly larger uncertainties in turbid waters.

The divergence of these $r_{rs}(\lambda)$-vs-$\omega_b(\lambda)$ formulas at higher turbidity might be caused by increased contribution to $r_{rs}(\lambda)$ from forward scattered light because when multiple-scattering dominates, not only backscattered but also forward scattered light (in a single-collision sense) contributes significantly to $R_{rs}(\lambda)$ (Park and Ruddick, 2005; Chami et al., 2006; Piskozub and McKee, 2011). It remains to be tested in future research whether there exists an optimal angular range in turbid waters, covering both backward and forward angular domains, over which the integrated volume scattering function correlates the best with $r_{rs}(\lambda)$, and how that optimal angular range changes with water turbidity. The good proportionality found between $r_{rs}(\lambda)$ and total $b(\lambda)/a(\lambda)$ in coastal waters of Great Bay (New Jersey), the Mississippi Sound, and Lake Superior (Sydor et al., 2002) implies a great likelihood that such optimal angular ranges exist.

3.2.5. Variability of molecular and particulate scattering coefficients

The total spectral backscattering coefficients of bulk water $b_b(\lambda)$ is contributed by water molecules, $b_{bw}(\lambda)$, and suspended particles, $b_{bp}(\lambda)$. The derivation of $a(\lambda)$ and $b_b(\lambda)$ from $R_{rs}(\lambda)$ always necessitates assumptions on spectral shapes of $b_{bp}(\lambda)$, or $a(\lambda)$, or their combinations. The $b_{bw}(\lambda)$ is considered as known but its magnitude varies with water temperature and salinity which can be important when $b_{bw}(\lambda)$ dominates against $b_{bp}(\lambda)$.

Both $b_{bw}(\lambda)$ and $b_{bp}(\lambda)$ generally follow a power law $\sim\lambda^{-\gamma}$. Here we show a normalized spectrum of $b_{bw}(\lambda)$ calculated using the formula given by Buiteveld et al. (1994) with a depolarization ratio of 0.039 (Fig. 2). The spectral slope γ is well estimated with a small uncertainty (~1%), and is considered invariable with temperature and salinity (Buiteveld et al., 1994; Twardowski et al., 2007; Zhang et al., 2009a), although the magnitude of $b_{bw}(\lambda)$ does vary with these parameters.

The $b_{bp}(\lambda)$ typically also follow a power law spectral shape for natural particle assemblages. This is generally the case even for phytoplankton-dominated natural particle assemblages (Neukermans et al., 2014). Finer spectral features of $b_{bp}(\lambda)$ associated with anomalous dispersion around strong absorption bands (Morel and Bricaud, 1986) cannot be excluded but are rarely observed in nature especially in coastal and inland waters; most reports of such features are made for

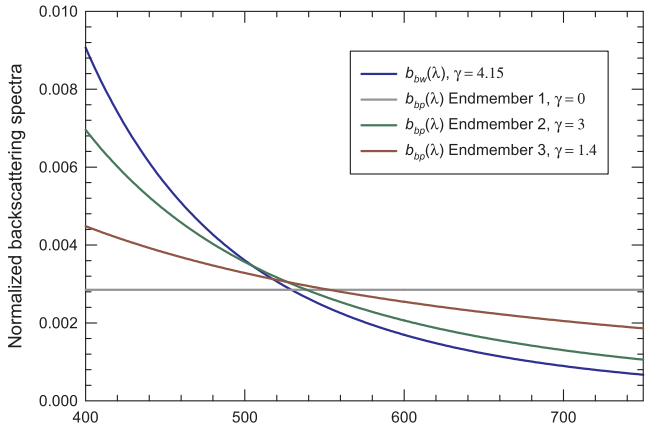

Fig. 2. Representative endmembers of particulate backscattering coefficient $b_{bp}(\lambda)$ normalized by its integral over the entire spectrum. Endmenber 1 represents the lower bound of the power spectral slope, γ, in natural waters; 2 the upper bound of γ in open oceans; and 3 the upper bound of γ in coastal waters. Pure-water backscattering coefficient $b_{bw}(\lambda)$ is also shown for comparison.

phytoplankton cultures which tend to be dominated by algal cells with quasi-monodispersed size distribution (e.g., Stramski et al., 2001).

Fig. 2 illustrates the range of variation in spectral shapes of $b_{bp}(\lambda)$ in comparison with $b_{bw}(\lambda)$. Each spectrum is normalized by the integral of the entire spectrum of 400–700 nm or 400–750 nm. For conciseness we present only endmember spectra of $b_{bp}(\lambda)$ considered realistic to represent natural waters. Three endmembers corresponding to extreme values of γ of $b_{bp}(\lambda)$ are shown. For suspended particles in open oceans γ are found to vary from 0 to 3 (endmembers 1 and 2) (Reynolds et al., 2001; Loisel et al., 2006); for coastal particulate assemblages reported values of γ fall in a much narrower range of 0–1.4 (endmembers 1 and 3) (Babin et al., 2003a; Stramski et al., 2004b, 2007; Sydor, 2006; Snyder et al., 2008; Neukermans et al., 2014, 2016; Zheng et al., 2014; Slade and Boss, 2015). Some of the studies cited above report the spectral slope of $b_p(\lambda)$ and here we consider those values equivalent to that of $b_{bp}(\lambda)$ owing to scarcity of field-measured $b_{bp}(\lambda)$ data. This is acceptable since the ratio of $b_{bp}(\lambda)/b_p(\lambda)$ is spectrally insensitive (Stramski et al., 2004a) and we are trying to identify only endmembers of this parameter.

To understand the variability of $b_{bp}(\lambda)$ it is helpful to examine it from a mechanistic standpoint (Fig. 3). In a diluted medium where single-scattering dominates, $b_{bp}(\lambda)$ can be calculated as the sum of backscattering cross sections $\sigma_{bb}(\lambda)$ of all suspended particles per unit volume of water. For each individual particle, $\sigma_{bb}(\lambda)$ can be calculated as $Q_{bb}(\lambda)\ \pi\ D^2/4$. The Q_{bb} factor depends on particle size, shape, internal structure, and complex refractive index (relative to water) $m(\lambda)$ of all materials inside the particle. The real part of the index, n (main factor affecting scattering), depends mainly on density of dry mass (Aas, 1996; Woźniak and Stramski, 2004), whereas the imaginary part, n' (main factor affecting absorption), essentially quantifies the average "darkness" of materials packed inside a particle. For organic-dominated particles including living phytoplankton and organic detritus, water content dilutes the dry mass and decreases the value of n. In addition, inhomogeneity of n introduced by internal structures such as gas vesicles and mineral shells enhances light scattering. For example, gas vesicles can enhance the scattering efficiency of Microcystis cells by 90% to one order of magnitude (Dubelaar et al., 1987; Klemer et al., 1996; Volten et al., 1998; Matthews and Bernard, 2013). Coccolithophore cells are known to be effective scatterers (Balch et al., 1991) owing to their external calcite plates which has a high n-value of ~1.17 (Woźniak and Stramski, 2004). In contrast, opal (hydrated amorphous silica, $SiO_2{\cdot}nH_2O$) in diatoms has a n-value of only ~1.07 (Morel and Bricaud, 1986; Aas, 1996; Woźniak and Stramski, 2004), which is almost the same as that of organic particles (~1.05, Morel and Bricaud, 1986; Bricaud et al., 1988; Aas, 1996; Stramski et al., 2001).

If we ignore particle internal structure and assume that particles suspended in water are randomly oriented so that the effect of particle shape can be averaged out, we can simplify each particle as a homogeneous sphere and the single-particle $Q_{bb}(\lambda)$ factor can be derived from the formula given by Bohren and Huffman (1983, p. 383) or van de Hulst (1957, p. 35) as

$$Q_{bb}\ (\lambda) = \frac{\int_{\pi/2}^{\pi} (i_1(\theta,n,n',D,\lambda) + i_2(\theta,n,n',D,\lambda))\sin\theta d\theta}{(n_w \pi D/\lambda)^2}, \quad (1)$$

where i_1 and i_2 are the scattered irradiances per unit incident irradiance (dimensionless irradiances) for incident light parallel and perpendicular to the scattering plane, respectively. They can be calculated using Mie (1976) theory and we used the "FASTMIE" code (https://scattport.org/) written by Wayne H. Slade. Results are shown in Fig. 4 for weakly to highly absorbing organic (n = 1.05) and mineral (n = 1.15) particles.

Fig. 4 provides insights to help understand the range of variability in the slope parameter γ of $b_{bp}(\lambda)$. For a monodispersed particle assemblage, the power spectral slope γ can be calculated as $\frac{\log[Q_{bb}(\lambda_2,D)\ /\ Q_{bb}(\lambda_1,D)]}{\log(\lambda_1\ /\ \lambda_2)}$, where we choose λ_1 = 400 nm and λ_2 = 700 nm. Among all cases in Fig. 4, the steepest spectral slope γ is ~3.8 and corresponds to non-absorbing colloids (D/λ < ~0.4). The second steepest γ is ~1.7 which is found for organic particles in the size range of D/λ = 20–60, followed by a slope of ~1.1 for mineral particles in the size range of D/λ = 2–10. These results are consistent with the upper bound of γ = 1.4 measured in coastal waters (Fig. 2) and indicate that submicron sized particles are generally not important for b_{bp} in coastal waters, whereas the steep endmember of γ = 3 found in open ocean waters can only be explained by a significant contribution of colloidal particles to $b_{bp}(\lambda)$.

3.3. Tier-3 to Tier-4: Attributing total absorption coefficient to components

The Tier-3 variables such as $a(\lambda)$ and $b_b(\lambda)$ are total optical properties but remote sensing of water quality often entails partitioning them into individual components. Partitioning of $a(\lambda)$ is challenging because the absorption bands of different components overlap and their spectral shapes vary. Partitioning of $b_{bp}(\lambda)$ has not been done so far; there is not even a field methodology that separately measures its components for natural particulate assemblages. In this section, we discuss uncertainties involved in the partitioning of $a(\lambda)$ into pure water, $a_w(\lambda)$, phytoplankton, $a_{ph}(\lambda)$, suspended mineral and nonalgal organic particles, $a_d(\lambda)$, and CDOM, $a_g(\lambda)$, components, all of which are categorized as Tier-4 variables except a_w (Fig. 1). These components are defined on a rather arbitrary basis and largely limited by current

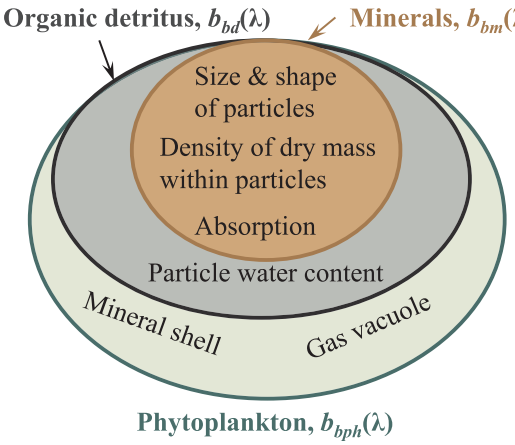

Fig. 3. Schematic diagram illustrating main factors that drive variations in particulate light backscattering coefficient $b_{bp}(\lambda)$ contributed by typical natural constituents such as minerals, phytoplankton, and organic detritus.

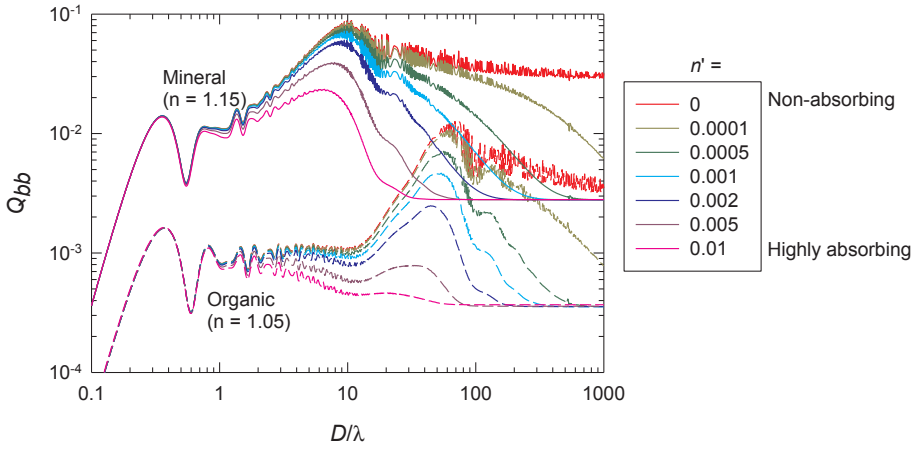

Fig. 4. Single-particle backscattering efficiency factors calculated for particles suspended in water with various size (relative to wavelength) and composition (different n and n' values) using Eq. (1) based on Mie theory. Note that λ is wavelength of light in vacuum.

technical capabilities to separately measure them. Note that partitioning of $a(\lambda)$ into these components is physically sound because IOPs can be treated as linearly additive, i.e., we can write $a(\lambda) = a_w(\lambda) + a_{ph}(\lambda) + a_d(\lambda) + a_g(\lambda)$; this is not the case for apparent optical properties such as $K_d(\lambda)$, which depends not only on IOPs but also illumination conditions.

3.3.1. Variability of pure water absorption coefficient

Pure water absorption coefficient $a_w(\lambda)$ depends on temperature and salinity. The temperature dependency is generally small but can be significant in the vicinity of discrete bands associated with overtones and harmonics of the vibrational modes of the O—H bond (Pegau et al., 1997; Pope and Fry, 1997; Sullivan et al., 2006; Röttgers et al., 2014). For example, local maxima of temperature-dependency were found at around 516, 606, 739, and 837 nm, where $a_w(\lambda)$ changes by ~0.3, 0.5, 0.6, and 0.4% per °C, respectively (Pegau et al., 1997; Pope and Fry, 1997; Röttgers et al., 2014). The salinity dependency remains small with no more than ± 0.05% per PSU (practical salinity units) within 400–900 nm (Pegau et al., 1997; Sullivan et al., 2006; Röttgers et al., 2014).

Two endmembers of normalized $a_w(\lambda)$ spectra are shown in Fig. 5, which were calculated using the formula given by Röttgers et al. (2010). Differences in these two endmembers are associated mainly with the use of two extreme temperatures (−2 and 35 °C) found in natural seawater. Salinity effect is negligible when temperature varies within such a large range. Note that $a_w(\lambda)$ in the spectral region shorter than 550 nm in Fig. 2a corresponds to the lowest values adopted by Röttgers et al. (2010) but there is still significant disagreement among different studies which can differ by up to > 1 order of magnitude (Pegau et al., 1997). Lee et al. (2015b) found it appealing to use even lower values within 350–550 nm to achieve a closure for remote-sensing reflectance measured in "clearest" subtropical gyre waters. The lower $a_w(\lambda)$ values was partly confirmed by Mason et al. (2016) using a novel diffuse reflector that is more reflective than Spectralon (Labsphere Inc.). At longer wavelengths (550–800 nm), the discrepancy in estimated values of a_w among different investigators is smaller but still between 5 and 10% (Pegau et al., 1997), and the actual uncertainty in determination of each individual spectrum can be even greater (± 15%) (Smith and Baker, 1981).

The uncertainty in measurement of $a_w(\lambda)$ and its temperature/salinity dependency deserve attention should any information contained in the red and NIR bands be used as a basis for inverting $R_{rs}(\lambda)$ to derive IOPs (e.g., Shi and Wang, 2014) or water quality parameters such as [Chl-a] (e.g., Gitelson et al., 2007). In these spectral regions the contribution of pure water to total light absorption coefficient are significant and therefore the use of accurate $a_w(\lambda)$ values is essential. The temperature/salinity dependency in $a_w(\lambda)$ can be accounted for using formulas provided by Sullivan et al. (2006) covering 400–750 nm or by

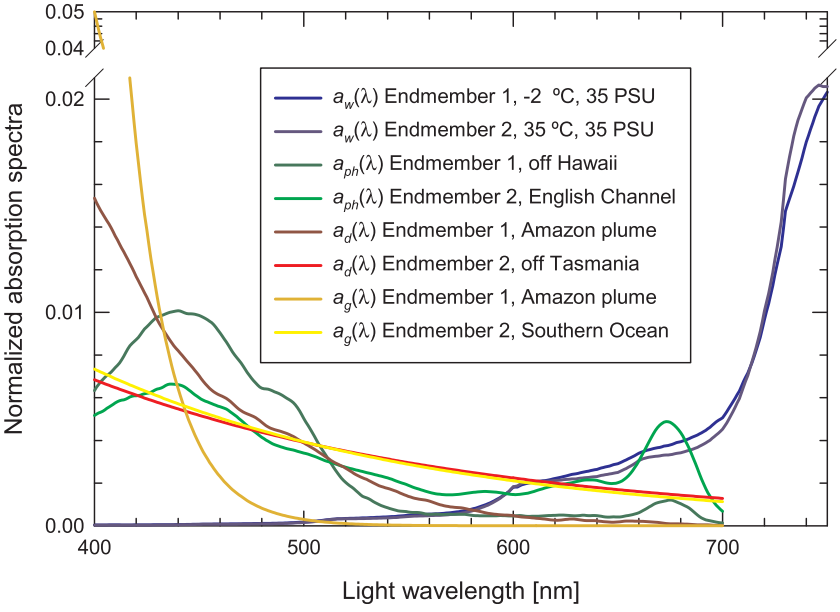

Fig. 5. Same as Fig. 2 but for light absorption coefficients. Sampling location of each endmember is also labeled.

Röttgers et al. (2010) and Röttgers et al. (2014) covering 400–14000 nm.

3.3.2. Variability of CDOM absorption coefficient

The endmembers of $a_g(\lambda)$, $a_d(\lambda)$, and $a_{ph}(\lambda)$ are taken from a global dataset assembled by Zheng and Stramski (2013) using mainly SeaWiFS Bio-optical Archive and Storage System (SeaBASS) data (Fig. 5). CDOM absorption coefficient $a_g(\lambda)$ decays with λ and the endmembers of $a_g(\lambda)$ were selected based on minimum and maximum values of the spectral steepness. After fitting an exponential function of λ with a single spectral slope S_g to the measured data within 400–550 nm, we obtained the two endmembers of 0.0062 and 0.0513 nm^{-1}, respectively (Fig. 5).

Light absorption of CDOM in the visible spectral region arises mainly from proteins, humic acids, and fulvic acids (Carder et al., 1989; Wozniak et al., 2005; Loiselle et al., 2009) (Fig. 6). Terrestrial originated CDOM is mainly a product of partially oxidized lignins and tannins (Boyle et al., 2009). Autochthonous phytoplankton-derived CDOM is believed to be produced mainly by bacteria which transform uncolored organic substance into colored molecules (Rochelle-Newall and Fisher, 2002b; Coble, 2007). CDOM may also be excreted by zooplankton (Steinberg et al., 2004). Whether phytoplankton can directly exude CDOM is still a debatable question (Rochelle-Newall and Fisher, 2002b; Castillo et al., 2010). The absorption spectral shape of autochthonous fulvic-acid-type CDOM produced by healthy phytoplankton is more variable than those of terrestrial originated humic and fulvic acids (Loiselle et al., 2009). The spectral slope of fulvic acids tends to be steeper than that of humic acids for both marine and terrestrial CDOM (Carder et al., 1989; Loiselle et al., 2009), followed by proteins (Wozniak et al., 2005) although there are some overlaps among these groups. Within each group the absorption efficiency may vary by more than two orders of magnitude (Wozniak et al., 2005). Many organic materials commonly found in natural waters essentially do not absorb visible light, such as aromatic amino acids, mycosporine-like amino acids, purine and pyridine compounds, and unoxidized lignins (Wozniak et al., 2005).

There is a vast body of literature on variation of S_g in the UV associated with various sources and processes such as photo-bleaching and microbial consumption. For example, inland, estuarine, and coastal marine waters that receive significant amount of terrestrial-originated CDOM are found to have flatter S_g than open oceans (Green and Blough, 1994; Del Vecchio and Subramaniam, 2004). CDOM produced by degrading phytoplankton assumes a flatter S_g in 300–500 nm compared with ambient CDOM (Zhang et al., 2009b). In contrast, photo-bleaching (Del Vecchio and Blough, 2002) and microbial activities (Nelson et al., 2004) tend to steepen S_g by breaking down flat-slope CDOM into steep-slope products. These trends are observed for S_g in the UV and whether they hold for the visible spectral region remains to be further investigated. For example, Loiselle et al. (2009) found opposite trends with photobleaching between S_g values calculated for the spectral regions of < 450 nm and > 500 nm.

3.3.3. Variability of nonalgal particulate absorption coefficient

The two endmembers of $a_d(\lambda)$ were selected in the same fashion as those for $a_g(\lambda)$ (Fig. 5). The exponential spectral slope, S_d, of the endmembers which characterizes overall spectral shape of $a_d(\lambda)$ ranges from 0.0056 to 0.0193 nm^{-1}, which is narrower than that exhibited in $a_g(\lambda)$. Interestingly, the two steep-slope endmembers for $a_d(\lambda)$ and $a_g(\lambda)$ are both found in waters affected by the Amazon river plumes, whereas the flat-slope ones are both found in or near the Australian section of the Southern Ocean, which suggest possible linkages in absorption properties of dissolved and particulate matter in a specific region.

Chemical composition and particle size distribution are two main factors that determine the light absorption of suspended particles comprising both organic and mineral materials. Light absorption by the organic portion of nonalgal particles arises largely from various proteins and humic matter (Fig. 6) (Wozniak et al., 2005), similar to CDOM except that those materials are packed in particles. In addition, non-photosynthetic pigments including phaeo-pigments and carotenoids absorb in the visible range, leading to departure of $a_d(\lambda)$ from a perfect exponential function of λ.

The most common inorganic chromophorous agent is iron (Babin and Stramski, 2004; Estapa et al., 2012) (Fig. 3a). The presence of iron uplifts the absorption spectrum of $a_d(\lambda)$ in the spectral region around 500 nm (Babin and Stramski, 2004; Bowers and Binding, 2006). Other minerals common to marine environments such as aluminosilicates, silicates, and carbonates generally show negligible absorption in the visible range (Babin and Stramski, 2004). Mineral absorption coefficient can be enhanced by coexisting CDOM via electrochemical adsorption of CDOM onto the mineral surfaces (Binding et al., 2008). In addition, black carbon can be important to particulate light absorption in coastal waters near urban areas (Stramska et al., 2008) but has not been well studied.

Similar to $b_{bp}(\lambda)$, $a_d(\lambda)$ can be calculated as the sum of absorption cross section, $\sigma_a(\lambda) = Q_a(\lambda)\,\pi\,D^2/4$, of all nonalgal particles per unit volume of water, where $Q_a(\lambda)$ is the absorption efficiency factor and is proportional to $n'(\lambda)D/\lambda$ (van de Hulst, 1957), independently of n. Fig. 7 shows $Q_a(\lambda)$ calculated as a function of D/λ for particles of different composition using the formula from van de Hulst (1957). A key feature is that the increase of Q_a slows down towards large values of $n'(\lambda)D/\lambda$ owing to enhanced self-shading effect with a maximum threshold of 1 because a particle cannot absorb more light than what it physically intercepts. This feature implies that $a_d(\lambda)$ tends to be less wavelength-dependent for larger particles or particles composed of darker materials.

3.3.4. Variability of phytoplankton absorption coefficient

Photo-synthetic and accessory pigments dominate the light absorption of phytoplankton cells. Almost all phytoplankton absorption spectra share a primary peak in the blue ~440 nm and a secondary peak in the red ~670 nm. Accordingly, the two endmembers of $a_{ph}(\lambda)$ were selected based on extreme values of the blue-to-red phytoplankton absorption band ratio, $a_{ph}(440)$:$a_{ph}(670)$, spanning from 1.4 to 9.1 (Fig. 5). These two endmembers define a broad range of overall spectral shape of $a_{ph}(\lambda)$ across the visible range, which is associated mainly with cell size and intracellular pigment concentration, i.e., the degree of pigment packaging. The pigment packaging effect on $a_{ph}(\lambda)$ is essentially the same effect as particle size and darkness of material on the spectral slope of $a_d(\lambda)$. The spectrum of $a_{ph}(\lambda)$ tends to be flatter with lower blue-to-red $a_{ph}(\lambda)$ band ratio for larger and more pigment-rich cells, and vice versa.

A comparison between Figs. 2 and 5 demonstrates that the spectral

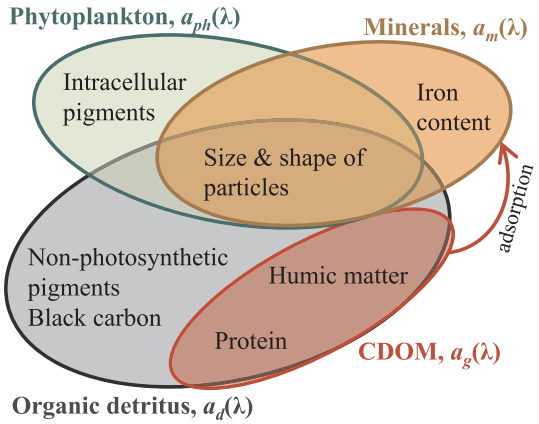

Fig. 6. Same as Fig. 3 but for light absorption coefficients contributed by CDOM, minerals, phytoplankton, and organic detritus. Note that mineral light absorption coefficient can be affected by the adsorption of CDOM onto surfaces of minerals.

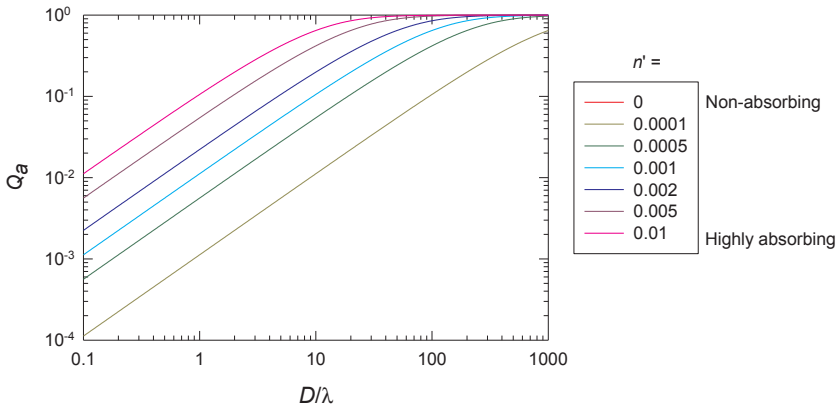

Fig. 7. Same as Fig. 4 but for particulate absorption efficiency factor calculated with the van de Hulst (1957) formula.

shape of $a_g(\lambda)$, $a_d(\lambda)$, and $a_{ph}(\lambda)$ vary more than $b_{bp}(\lambda)$ does in coastal waters. As a result, the spectral shape of $R_{rs}(\lambda)$ is dictated more by absorption coefficients whereas the magnitude of $R_{rs}(\lambda)$ reflects a combined effect of both absorption and backscatter.

3.4. Tier-4 to Tier-5: Deriving mass concentrations from inherent optical properties

Many applications require water quality parameters be reported in mass concentrations. The conversion from IOPs to mass concentrations is hence involved, which we categorize as Tier-5 variables (Fig. 1). Uncertainties introduced in this step arise mainly from the variability in mass-specific absorption and backscattering coefficients among various water constituents, leading to mismatches between dominant optical and mass contributors.

3.4.1. Variability of mass-specific optical properties of suspended particles

The [SPM] is a commonly used parameter to characterize particle loading. The mass-specific IOPs of suspended particles are governed by their composition and size distribution. Many studies have reported the general variability of mass-specific IOPs resulting from the combined effect of both size and composition. Only few have examined the two effects separately. Results of these studies on mass-specific particulate absorption, $a_p^*(\lambda) \equiv a_p(\lambda)/[SPM]$, and scattering coefficients, $b_p^*(\lambda) \equiv b_p(\lambda)/[SPM]$, are compared in Table 1 (Stramski et al., 2004b, 2007; Bowers et al., 2009; Woźniak et al., 2010).

Table 1 shows that the variability of $a_p^*(\lambda)$ in response to changes of particle size D_{V50} is quite variable with no obvious trend. For example, $a_p^*(400)$ can vary by as much as 7-times for a group of global soil minerals with D_{V50} ranging ~3-folds, or as little as 2-times for another group of San Diego coastal particles with D_{V50} ranging ~4-folds. The lack of trend suggests that $a_p^*(\lambda)$ depends weakly on particle size and is primarily affected by variations in particle composition, which is also supported by limited amount of measurement data. An experiment of five pairs of particulate samples, each pair of the same composition but different size distribution, reveals some 0.7–0.9-fold of variability in $a_p^*(\lambda)$ per 1-fold change of D_{V50} ranging within 1–5 μm (Stramski et al., 2007). In contrast, $a_p^*(400)$ ranges by ~7 folds for a set of global soil mineral samples as $n'(400)$ changes by ~6-fold (Stramski et al., 2007), and by ~4.6 folds for San Diego atmospheric dry deposits as $n'(400)$ changes by ~4-fold (Stramska et al., 2008).

These measurement results are consistent with theoretical calculations of single-particle volume-specific absorption cross-section, $\sigma_a(\lambda)/V$, the variability of which is equivalent to that of $a_p^*(\lambda)$ for a hypothetical particulate assemblage consisting of identical particles. Calculation results at an example wavelength of $\lambda = 550$ nm are shown in Fig. 8a, which shows that $\sigma_a(\lambda)/V$ is fairly flat across a broad range of D for each curve but changes significantly for particles with different composition (represented by n'). Thus, the use of $a_p^*(\lambda)$ as an avenue for estimating [SPM] depends on the uniformity of particle composition which can be quite stable, e.g., one case reported for San Diego coastal waters (Woźniak and Stramski, 2004).

In contrast to the relatively low sensitivity of $a_p^*(\lambda)$ to particle size variation, $b_p^*(\lambda)$ shows a trend of increasing variability with particle size in the size range of $D_{V50} > 1$ μm (Table 1). For the smallest particles ($D_{V50} = 1$–5 μm) $b_p^*(555)$ varies by a factor of only 1.5–1.9 when D_{V50} varies by 2–3 folds. For larger particles ($D_{V50} = 6.4$–187 μm) $b_p^*(\lambda)$ varies by a factor of 3.5–16.8 when D_{V50} varies by 2–5 folds. Although we cannot exclude the contribution from sample-to-sample variations in organic/mineral proportions to the observed variability in $b_p^*(\lambda)$, it is likely that particle size plays an important role in view of theoretical considerations. Fig. 8b shows volume-specific scattering

Table 1
Variability of SPM-specific absorption and scattering coefficients of suspended particles in association with particle size and composition. D_{V50}, median diameter of the particle volume distribution. Max, maximum value. Min, minimum value. N, number of samples.

Particle source	Mineral/Organic	Size characterized by D_{V50} [μm]	Ratio of Max:Min $a_p^*(400)$	Ratio of Max:Min $b_p^*(555)$	N	Reference
Asian dust	Mineral-dominated	1–2.5	4.6	1.5	6	Stramski et al. (2004b)
Global soil/dust particles[a]	Mineral-dominated	1.6–4.7	7	1.6	10	Stramski et al. (2007)
Iron-depleted single-mineral species	Mineral	2.0–4.1	n/a[b]	1.9	9	
San Diego coastal particles	Mineral-dominated	3.7–15	2	3.5	15	Woźniak et al. (2010)
Arctic under-ice bloom/bottom resuspension	Ranging from mineral- to organic-dominated	6.4–17.9	4.3	5.7 (532 nm)	4	Neukermans et al. (2014)
San Diego coastal particles	Mineral-organic-mixed	7–34	2.9	4.4	20	Woźniak et al. (2010)
San Diego atmospheric dry deposits	n/a	8.5–18.5	4.6	3.5	18	Stramska et al. (2008)
San Diego coastal particles	Organic-dominated	13–39	2.2	6	9	Woźniak et al. (2010)
Britain coastal particles	Mineral-dominated	57–187	n/a	16.8 (670 nm)	78	Bowers et al. (2009)

[a] Note that the organic-dominated KUW samples used in the original study are excluded for present calculation.
[b] n/a, not available or undetermined.

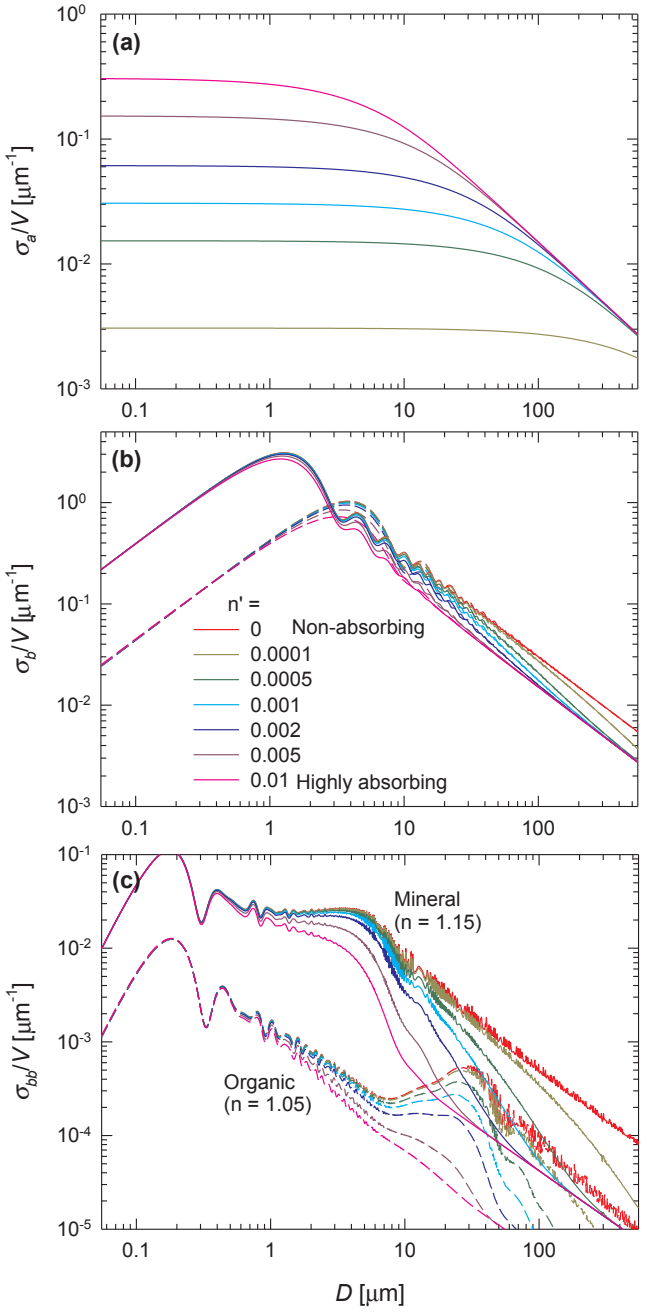

Fig. 8. Volume-normalized single-particle (a) absorption, (b) scattering, and (c) backscattering cross sections calculated for particles suspended in water with various size and composition. Panels (a) and (b) are obtained with the van de Hulst (1957) formula; (c) with Mie theory. λ = 550 nm.

cross-section, $\sigma_b(\lambda)/V$, calculated with Eq. (1). For both organic and mineral particles there is a maximum $\sigma_b(\lambda)/V$ located at around 3–5 μm for organic particles and 1–2 μm for mineral particles, which explains the small variability observed for particles near these size ranges. For larger particles, the larger variability of $b_p^*(\lambda)$ can be explained by the rapid changes in $\sigma_b(\lambda)/V$ with particle size.

We also calculated the single-particle volume-specific backscattering cross-section, $\sigma_{bb}(\lambda)/V$ (Fig. 8c), calculated with Mie theory. Compared with $\sigma_b(\lambda)/V$ (Fig. 8b), there is a broader size range within which σ_{bb}/V is relatively insensitive to variation of size for particles of the same composition. This explains the small variability in the mass-specific backscattering coefficient, $b_{bp}^*(\lambda)$, found in European and French Guyana coastal waters, where particle size varies within 10–140 μm but $b_{bp}^*(\lambda)$ at multiple wavelengths in the visible and NIR domain varies by only a factor of 3–4 and much of this variability could be caused by the varying degree of organic and mineral proportions (Neukermans et al., 2012). Similarly, the comparison between Figs. 8b and 8c also explains the smaller range of variability in $b_{bp}^*(532)$ (~2.3 times) than that in $b_p^*(532)$ (~5.6 times) as seen in four Arctic particulate assemblages with D_{V50} varying within 6.4–17.9 μm and with both organic-dominated and mineral-dominated particulate samples (Neukermans et al., 2014).

3.4.2. Variability of chlorophyll-specific phytoplankton absorption coefficient

The [Chl-*a*] is another frequently used satellite water quality product. The derivation of [Chl-*a*] from satellite data relies mostly on the absorption signal of phytoplankton. The variability of chlorophyll-specific absorption coefficient, $a_{ph}^*(\lambda)$, is spectrally minimal around the red absorption peak (~670 nm) owing to smallest influence from accessory pigments, and is higher around the blue absorption peak (~440 nm) (e.g., Bricaud et al., 1995; Stramski et al., 2001). Values of $a_{ph}^*(\lambda)$ determined based on data collected globally exhibit > 2 orders of magnitude variability around the blue and red absorption peaks with [Chl-*a*] spanning ~4 orders of magnitude (Table 2). The lowest phytoplankton absorption per unit [Chl-*a*] generally decreases from open ocean, to upwelling zone, to semi-enclosed coastal waters and enclosed inland waters, with no significant difference in $a_{ph}^*(\lambda)$ ranges between large-river estuaries and other "regular" coastal waters. It is common to see that a small coastal area exhibits similar or even higher degree of variability in $a_{ph}^*(\lambda)$ compared with a very large oceanic region.

Much of this variability is explained by the degree of pigment-packaging effect associated with cell size and intracellular pigment concentration. For example, the average $a_{ph}^*(670)$ of three smallest species (D = 0.7–1.4 μm) in the culture dataset assembled by Stramski et al. (2001) is 2-times higher than that of the two largest species (D = 12–28 μm); for 11 similar sized cells (D = 4–8 μm), the $a_{ph}^*(670)$ decays by a factor of ~3 with intracellular chlorophyll concentration, C_{cell}, ranging within 2–20 kg m^{-3}, which can be described mathematically as $a_{ph}^*(670) = 0.0834 C_{cell}^{-0.555}$ (R^2 = 0.71, N = 11). Additional variability in $a_{ph}^*(\lambda)$ arises from pigment composition. Presence of photoprotective pigments in high-light acclimated cells (Neukermans et al., 2014) or photosynthetic pigments in low-light acclimated cells (Bricaud et al., 1995; Babin et al., 2003a) enhances the light absorption independently from [Chl-*a*] thus induces a tendency of increasing $a_{ph}^*(\lambda)$.

Despite the large variability of $a_{ph}^*(\lambda)$ in each dataset, the variability at any given [Chl-*a*] rarely exceeds a factor of 5 (see references in Table 2). In addition, the calculation of $a_{ph}^*(\lambda)$ is still subject to significant measurement uncertainties for both $a_{ph}(\lambda)$ and [Chl-*a*]. McKee et al. (2014) suggest that uncertainties of measured $a_{ph}^*(\lambda)$ vary somewhere between ± 33% and ± 83%. These uncertainties imply a variability of a factor of 2, 3, and 11, respectively if we divide the upper bounds of the uncertainty ranges by the lower bounds. Therefore, the actual variability in $a_{ph}^*(\lambda)$ is likely to be less than the reported ranges summarized in Table 2. Thus, the use of a [Chl-*a*]-dependent $a_{ph}^*(\lambda)$ formula is a promising avenue to derive [Chl-*a*] from satellite-derived $a_{ph}(\lambda)$.

3.4.3. Variability of carbon-specific CDOM absorption coefficient

Satellite data have also been used to derive the concentration of Dissolved Organic Carbon, [DOC], through the light absorption coefficient of CDOM which is the colored fraction of the total DOC pool. Observed values of DOC-specific CDOM absorption coefficient, $a_g^*(\lambda) \equiv a_g(\lambda)/[\text{DOC}]$, vary dramatically (Table 3). An important reason is because CDOM is a variable portion of total DOC, with the remaining portion of DOC essentially non-chromophoric and therefore not quantifiable with optical methods. Although the magnitude of $a_g^*(\lambda)$ are shown to be strongly related to the spectral slope of $a_g(\lambda)$ in the

Table 2
Variability of chlorophyll-specific absorption coefficient of phytoplankton at the blue and red absorption maxima. Samples were taken from the surface layer unless otherwise noted. Methods of [Chl-*a*] measurements are specified for each study. *N*, number of samples.

Location	a_{ph}^*(440) range [$m^2\,mg^{-1}$]	a_{ph}^*(670) range [$m^2\,mg^{-1}$]	[Chl-*a*] range [mg m^{-3}]	*N*	Reference
Open oceans					
Arabian Sea	0.03–0.14	0.015–0.05	0.15–2.8[a]	101[§]	Sathyendranath et al. (1999)
From Bay of Biscay to the Canary Islands	0.036–0.38	0.016–0.126	0.06–2.0[c]	30	Babin et al. (2003b)
Subtropical gyre to Chilean upwelling zone	0.043–0.11	0.017–0.035	0.017–1.5[c]	66[§]	Bricaud et al. (2010)
Patagonian shelf-break	0.018–0.173	0.009–0.046	0.1–22.3[a]	226[‡]	Ferreira et al. (2013)
A time-series station in Caribbean Sea with seasonal upwelling	0.02–0.16	0.015–0.035	0.07–8.5[c]	69	Lorenzoni et al. (2015)
Coastal waters					
Baltic Sea	0.010–0.083	0.0077–0.049	4.35–38.7[c]	54	Babin et al. (2003b)
North Sea	0.003–0.10	0.0014–0.055	0.21–48.7[c]	88	
English Channel	0.0068–0.18	0.0015–0.092	0.28–30.2[c]	77	
Adriatic Sea	0.011–0.11	0.010–0.054	0.83–30.6[c]	38	
Mediterranean coast	0.013–0.11	0.0045–0.045	0.09–8.5[c]	51	
Estuaries in Queensland, Australia	0.02–0.11	0.015–0.06	0.2–8.8[c]	71	Blondeau-Patissier et al. (2009)
Long Island Sound	≤0.0059 –	0.002–0.042	0.7–80.6[a]	33	Aurin et al. (2010)
Off east coast of Malaysian Peninsular	0.004–0.23	0.001–0.027	0.11–7.7[b]	174	Bowers et al. (2012)
East China Sea	0.01–0.3	0.005–0.05	0.3–10[a]	86	Lei et al. (2012)
Hudson Bay	0.018–0.124	0.01–0.065	0.08–1.5[c]	54	Xi et al. (2013)
Large-river estuaries and plumes					
Mississippi River Plume	0.02–0.10	0.02–0.09	0.68–12[c]	22	D'Sa et al. (2006)
Orinoco River plume	0.019–0.16	0.014–0.04	0.15–8.1[a]	73	Odriozola et al. (2007)
St. Lawrence Estuary and Gulf	0.013–0.14	0.008–0.036	0.06–16.2[c]	76	Roy et al. (2008)
Yellow River plume	–	0.002–0.035	0.65–13.5[a]	62	Xing et al. (2008)
Yangtze River plume	0.017–0.16	0.008–0.055	0.1–6.1[c]	143[‡]	Wang et al. (2014)
Inland lakes					
Lake Erie, USA	0.013–0.51	0.007–0.157	0.3–70[b]	90	Binding et al. (2008)
Lake Taihu, China	0.016–0.18	0.006–0.057	2.1–104[b]	57	Le et al. (2009)
Mixed water types					
St. Lawrence Estuary and Gulf; Pacific and Atlantic Oceans; Mediterranean Sea	0.01–0.18	0.005–0.06	0.02–25[a,b,c]	815[§]	Bricaud et al. (1995)

[a] Chl-*a* and pheopigments measured with fluorometric methods.
[b] Chl-*a* and pheopigments measured with spectrophotometric methods.
[c] Total Chl-*a* measured with the HPLC method.
[§] Sampling depth varies within the euphotic zone.
[‡] Sampling at surface and the Chl maxima layer.

Table 3
Variability of DOC-specific absorption coefficient of CDOM. Max, maximum value. Min, minimum value. *N*, number of samples.

Location	Ratio of Max:Min $a_g^*(\lambda)$	λ [nm]	*N*	Reference
Coastal waters				
Middle Atlantic Bight	6.6	355	672	Mannino et al. (2008)
Chesapeake Bay	6.1	355	111	Rochelle-Newall and Fisher (2002a)
Delaware Bay and Middle Atlantic Bight	25	355	208	Del Vecchio and Blough (2004)
South Atlantic Bight	21	350	115	Kowalczuk et al. (2010)
South Baltic Sea	3.1	355	198	Ferrari et al. (1996)
Danish coastal waters	7.5	375	89	Stedmon et al. (2000)
Large-river plumes				
Pearl River estuary	4.2	355	18	Chen et al. (2004)
Mississippi River plume	55	355	222	Fichot and Benner (2011)
Mackenzie River plume	7.7	440	241	Matsuoka et al. (2012)
Inland waters				
Rivers in Georgia, USA	2.4	440	12	Yacobi et al. (2003)
Lakes in Netherlands	2.5	440	13	Dekker (1993)
Lake Taihu	2.7	355	40	Zhang and Fell (2007)
	4	440	40	

275–295 nm region (Helms et al., 2008; Fichot and Benner, 2011, 2012), passive satellite sensors do not have the capability to make measurements in these bands. Consequently, the derivation of DOC from the light absorption coefficient is plausible only under specific conditions. For example, the quantity of uncolored DOC relative to CDOM is negligible, or uncolored DOM varies in proportion with CDOM, or the uncolored DOC is invariable, forming a stable background.

A more tractable problem to pursue is the estimation of CDOM absorption coefficient normalized by its own carbon. Such studies require separation of CDOM from non-chromophoric DOC and are rarely available in literature. Twardowski and Donaghay (2002) discussed reported values of carbon-normalized CDOM absorption coefficient and concluded that the difference is within 35%. Table 3 shows that compared with regions where mixing between coastal and oceanic waters happens, $a_g^*(\lambda)$ is generally more constrained in inland waters where CDOM generally dominates DOC. This suggests that carbon-normalized CDOM absorption coefficient might be quite constrained, at least locally.

4. Use of ocean color radiometric data for coastal pollution applications

Satellite OCR data can be used in a variety of ways to monitor and assess coastal and inland water pollution and its impacts. Representative examples of these applications are provided below, accompanied with insights from Section 3 on uncertainties that can be

used to explain the varying degree of robustness for the different tiers of OCR products (see Fig. 1). The order in which these examples are given follows the ordering of uncertainty tiers and is also based on whether the target parameter of an application is directly related with satellite-derived reflectance. In some cases the target is optically significant or resultant from optical processes, e.g., oil spills, phytoplankton blooms, and turbid plumes. In other instances, ocean color is used as a proxy or indicator for the target parameter that is optically inactive or insignificant but known to be strongly associated with optically significant materials, e.g., CDOM can be a semi-conservative tracer for salinity, and turbid plumes generated by discharge of terrestrial runoff can be an indicator for pollutants and pathogens.

4.1. Oil spill remote sensing

Ocean color radiometry data have traditionally been used to detect the areal coverage of oil spills and natural oil seepages, complementing high-resolution, all weather but coverage-limited Synthetic Aperture Radar (SAR) observations (e.g., Digiacomo et al., 2004). Surface slicks can be detected based on the reflectance contrast with surrounding waters under favorable sun-sensor geometry and sea surface roughness conditions (Hu et al., 2003). In offshore waters, the contrast of sun glint can be used to identify oil slicks (Hu et al., 2009), although it can be difficult to distinguish sun glitter between uncontaminated waters and those covered by spread sheen oil (Fingas and Brown, 2014). Large oil spills such as the BP Deepwater Horizon spill can also be readily detected from satellite RGB (Red-Green-Blue) imagery (Leifer et al., 2012) or based on spectral contrast in $nL_w(\lambda)$ (Bulgarelli and Djavidnia, 2012). In these applications satellite remote sensing provides a qualitative evaluation on presence or absence of oil spills. In particular, the spatial extent of oil coverage and duration of spill coverage revealed from satellite imagery provides fundamental information for assessing ecological impacts of natural and anthropogenic oils, such as inhibition of gas exchange at the air–water interface and changes in phytoplankton biomass (e.g., Leifer et al., 2012; Fingas, 2014; Fingas and Brown, 2014).

While such information is also useful for conducting spill response and post-spill ecological impact assessments and remediation efforts, what is truly desired is the oil thickness because only oils that are at least 0.5 mm thick are “actionable” from a response-team’s standpoint, e.g., dark oil and emulsified oil (Fingas and Brown, 2014). Thinner sheen oils are considered non-recoverable and it is typically unnecessary to initiate extensive countermeasures. Currently, there are limited in-water validated remote-sensing methods that provide robust estimation of oil thickness in the range relevant to oil spill cleanup efforts, owing partly to a lack of *in situ* techniques for oil thickness measurement (Fingas and Brown, 2014).

However, the NIR-SWIR bands (0.7–2.5 μm) appear to represent a promising spectral range where useful information can be extracted for this purpose. Remote-sensing reflectance measurements for oil emulsion collected from the 2010 Deepwater Horizon spill exhibit significant changes in both spectral shape and magnitude with respect to changes in oil thickness at the millimeter level across the spectral range from UV through SWIR (0.35–2.5 μm) (Clark et al., 2010). The most sensitive responses in $R_{rs}(\lambda)$ were observed in discrete NIR-SWIR bands whereas sensitivity in the UV–visible bands is relatively low. This is largely because the crude oil from BP Deepwater Horizon well is 3–5 orders of magnitude more absorbing than pure water in the UV–visible spectral range owing to presence of asphaltines, but 1–2 orders of magnitude less absorbing around specific NIR-SWIR bands (Clark et al., 2010). These features have been used to develop algorithms for mapping the thickness and total volume of thick oil (> 0.5 mm) using Airborne Visible/Infrared Imaging Spectrometer (AVIRIS), MODIS, and MERIS (Clark et al., 2010; De Carolis et al., 2014; Sicot et al., 2015). Currently the use of remote-sensing data in the NIR-SWIR bands for oil-thickness estimation is in a rather preliminary stage. The chemical composition of crude oil is highly variable with extraction location (Fingas, 2014) and more experiments are needed to obtain fundamental knowledge on the spectral light absorption coefficients of various types of crude oils in the UV-SWIR spectral range.

Most oil spills are fairly small-scale (vice the spatially extensive Deepwater Horizon event); as such, imagery from higher-resolution sensors such as Landsat-8 and Sentinel-2 can be an effective tool in their mapping. These sensors provide data at 20–60 m resolution at discrete NIR-SWIR bands and can potentially be useful for oil thickness assessments. Alternatively, the 250-m bands on MODIS and SGLI and the 300 m bands on OLCI data provide reduced spatial resolution, but significantly greater areal coverage with more frequent revisits than Landsat-8 and Sentinel-2. Effective synergies can be realized through the combination of data from these sensors.

While remote sensing of any water quality parameter will typically benefit from a multitude of observations and diverse approaches, this is particularly the case for oil spill applications. Different types of satellite sensors have their own respective strengths and weaknesses. For example, cloud cover, darkness and lack of sun glint conditions often preclude the availability and utility of suitable visible observations; SAR observations become the only option in such conditions particularly given their all-weather capabilities and relatively high spatial resolution (e.g., Brekke and Solberg, 2008; Shcherbak et al., 2008). Further, coordinated use of multi-sensor satellite data (e.g., visible/infrared sensors, SAR, altimetry, scatterometry) enables not only spill detection, but broader synergistic assessment of the dynamics, evolution, and fate and transport of oil slicks (see Shcherbak et al., 2008). This is particularly crucial given surface oil is exposed to dynamic and diverse oceanographic and meteorological phenomena such as currents, fronts, internal waves, Langmuir cells, etc.

4.2. Water turbidity and clarity

OCR data have been used extensively to characterize, quantify, and monitor water turbidity and clarity in coastal ocean and inland waters (see IOCCG, 2008 for overview). Turbidity is the cloudiness or haziness of a fluid caused by suspended particles which deflect light away from the incident direction. Higher turbidity often implies loadings of nutrients and other dissolved and particulate contaminants, and a variety of associated physical and biological impacts (Bisson and Bilby, 1982; Olsen et al., 1982; Newcombe and Macdonald, 1991; Balogh et al., 1997; Fabricius, 2005; Hirsch, 2012). Clarity is a measure of distance of light penetration in various directions. It can be used to evaluate the impact of suspended sediment on aquatic ecosystems including light availability for phytoplankton and submerged aquatic vegetation (e.g., Longstaff and Dennison, 1999; Moore and Wetzel, 2000; Peralta et al., 2002). Another important aspect of this concept is visual clarity which affects predator–prey interactions (Abrahams and Kattenfeld, 1997) and human underwater activities. Albeit two sides of the same coin, turbidity and clarity as derived from remote sensing are subject to different levels of uncertainty. As explained in detail below, both turbidity and clarity can be considered Tier-3 products (Fig. 1) because they can be well-predicted from total inherent optical properties. However, turbidity is related predominantly to the scattering property whereas clarity is affected by both scattering and absorption properties.

4.2.1. Turbidity

The traditional method for determination of turbidity is by using a nephelometer. There are two benchmark methods which specify mainly spectral and angular ranges of detected light: The US Environmental Protection Agency (EPA) Method 180.1 (USEPA, 1993) (EPA method, hereafter) and the International Organization for Standardization (ISO) 7027 (ISO, 1999) (ISO method, hereafter). Nephelometers conforming to the EPA method measure turbidity values in Nephelometric Turbidity Unit (NTU), whereas those compliant with the ISO method report values in Formazin Nephelometric Unit (FNU) (Table 4). The two

Table 4
Comparison between traditional nephelometers and satellite nephelometry.

	Nephelometric instruments NTU (EPA Method 180.1)	FNU (ISO 7027)	Satellite nephelometry
Incident light	Light in a broad band from UV to IR with peak intensity at 1000–1500 nm	Light in a narrow band of 830–890 nm	Sun light that reaches ground
Spectral range of scattered and detected light	Peak response within 400–600 nm	830–890 nm	Typically multiple bands from visible to NIR, sensor dependent
Detector center angle relative to incident angle	90°	90 ± 2.5°	> 90°; dependent on Sun-sensor geometry
Detector acceptance angle	60° maximum	20 − 30°	< 0.1°; dependent on sensor and spatial resolution; calculated as FOV/number of pixels within FOV
Sampling volume	Typically a few to tens of mL; instrument dependent		Varies by sensor and by water properties; calculated as (pixel size)^2/$K_d(\lambda)$

methods share the same formazin standard for calibration and main detection angle at ~90° from the direction of incident light. Detectors at forward, backward, and transmitted angles are optional to both methods which can be used to normalize detected light at the right angle and obtain turbidity values in Nephelometric Turbidity Ratio Unit (NTRU) or Formazin Nephelometric Ratio Unit (FNRU). The most significant difference between the two is the wavelength of detected light. Whereas the EPA method requires the detection of scattered "white" light with peak sensitivity in the green, the ISO counterpart favors a NIR light source. In terms of applicable turbidity ranges, these two methods were originally developed for regulatory purposes, i.e., assessing drinking water quality with turbidity values lower than 40 NTU or FNU, with dilution required for samples with higher turbidity. Natural water samples can be orders of magnitude more turbid. Many nephelometers are designed to accommodate the larger dynamic range by allowing manual and automatic adjustment of detector's amplification factor to avoid the necessity of sample dilution.

Nephelometer-derived turbidity in NTU and FNU appears to be closely related with *in situ* measured $R_{rs}(\lambda)$ values across different coastal water bodies. One of the most commonly used wavelengths to match $R_{rs}(\lambda)$ with turbidity measurements is 645 nm, partly because of the availability of this band on MODIS at 250-m resolution. Empirical relationships between $R_{rs}(645)$ and turbidity in NTU (actually NTRU, to be exact in this case) in Tampa Bay (Chen et al., 2007), turbidity in FNU in Bay of Biscay (Petus et al., 2010), and coastal waters off Belgium and French Guyana (Dogliotti et al., 2015) agree fairly well, especially in the range of 2–7 NTU/FNU where the three relationships differ by < 10% (Fig. 9). Note that only formulas that used *in situ* measured or satellite-derived but field-validated $R_{rs}(\lambda)$ data are included for this comparison to minimize uncertainties associated with $R_{rs}(\lambda)$.

The robustness of the $R_{rs}(645)$-turbidity relationship in spite of different optical geometry and light wavelengths used in the reflectance and turbidity measurements can be partly explained by the following factors. Turbidity measured by nephelometers essentially characterizes variation in light side-scattering coefficient, $b_s(\lambda)$. The determination of $b_s(\lambda)$ with the ISO method using light at ~860 nm is subject to only negligible variation in $a(\lambda)$ because at this wavelength pure water absorption dominates. Although the determination of $b_s(\lambda)$ with the EPA method is affected by more variation in total light absorption in the green bands, this effect is reduced by normalizing side-scattering with forward-scattering signals. In comparison, *in situ* measured $R_{rs}(645)$ varies largely with the coefficient $b_b(645)$ because at this wavelength phytoplankton, CDOM, and nonalgal particulate absorption coefficients are typically small (e.g., Babin et al., 2003b) compared with pure water contribution (~0.3 m^{-1}). The $b_s(\lambda)$ is expected to covary in a constrained fashion with $b_b(\lambda)$ in view of the flat angular shape of natural particulate SPF across 90 − 180° (Petzold, 1972). The discrepancy in scattering angle is further reduced by multiple-scattering effects which allow more side and forward-scattered light contributions to $R_{rs}(\lambda)$ (see discussions in Section 3.2.4). The spectral shapes of the $b_{bp}(\lambda)$ and $b_p(\lambda)$ are often flat in coastal waters (see discussion in Section 3.2.5) and therefore differences in light wavelengths between reflectance and turbidity measurements are also unlikely to significantly affect the $R_{rs}(645)$-turbidity relationship.

To conclude, there appears to be a globally applicable relationship between turbidity and $R_{rs}(\lambda)$ at bands with relatively low variability in $a(\lambda)$. We therefore deem satellite-derived turbidity a Tier-3 product subject to similar level of uncertainty as total IOPs (Fig. 1), and propose using satellite nephelometry (Table 4) as a promising tool to map turbidity distributions in global coastal and inland waters. An important advantage of satellite nephelometry is that any single sensor can provide synoptic turbidity data at regional to global scales without the issue of inter-instrument discrepancy which is a potential concern for interpreting data collected with multiple *in situ* nephelometers.

One problem that needs to be addressed in satellite nephelometry is the loss of sensitivity (also known as saturation) in $R_{rs}(\lambda)$ beyond a

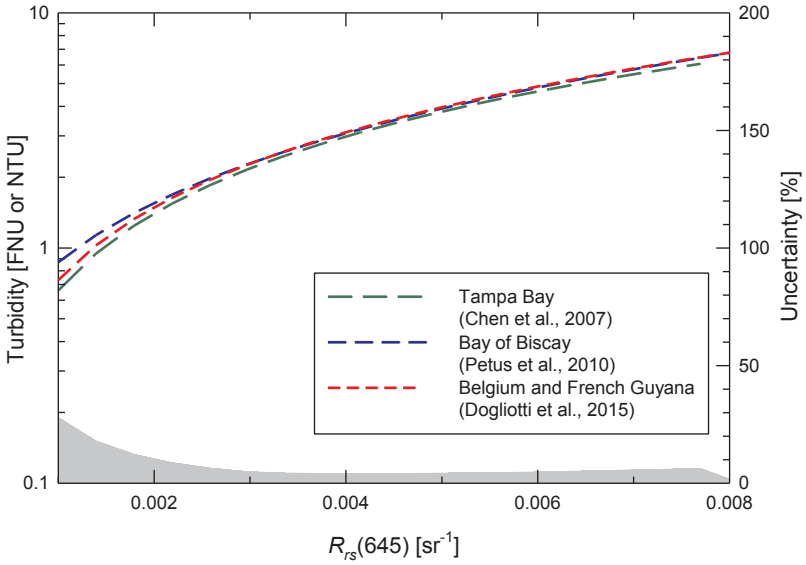

Fig. 9. Regression relationships between turbidity and *in situ* measured or verified remote-sensing reflectance. The left-hand axis refers to the colored curves, and the right-hand axis refers to the grey-shaded area. (For interpretation of the references to color in this figure legend, the reader is referred to the web version of this article.)

certain level of turbidity depending on the magnitudes of CDOM and pure water absorption coefficients, which are wavelength-dependent. (Froidefond et al., 2002; Petus et al., 2010; Dogliotti et al., 2015). This issue is caused by the increasing degree of particulate dominance in $a(\lambda)$ and $b_b(\lambda)$ with increasing turbidity (Doxaran et al., 2002b). In theory, $R_{rs}(\lambda)$ is a function of the ratio of $b_b(\lambda)/a(\lambda)$ which is contributed by water molecules, CDOM, and suspended particles. In coastal and inland waters molecular scattering can easily be dwarfed by particulate scattering so that $b_b(\lambda) \approx b_{bp}(\lambda)$. When the concentration of suspended particles is sufficiently high, the magnitude of CDOM and pure water absorption can also become insignificant compared with particulate absorption so that $a(\lambda) \approx a_p(\lambda)$. Under such conditions $R_{rs}(\lambda)$ is a function of the particulate optical property $b_{bp}(\lambda)/a_p(\lambda)$ which is independent of particulate concentration for the same assemblage of particles; hence the loss of sensitivity to turbidity.

This problem can be treated by selecting appropriate bands for different turbidity ranges. The criterion for band selection is essentially a balance between achieving sufficient SNR in $R_{rs}(\lambda)$ and avoiding loss of sensitivity to turbidity variation. First of all, the selected band must allow sufficient $b_b(\lambda)/a(\lambda)$ ratio so that the water is not too "dark". The other requirement is that $a_w(\lambda)$ must be sufficiently large at the selected band so as not to be dwarfed by $a_p(\lambda)$, leading to loss of sensitivity in $R_{rs}(\lambda)$. Dogliotti et al. (2015) suggest to use the 645-nm band for $R_{rs}(645) < 0.05/\pi$, switch to the 859-nm band for $R_{rs}(645) > 0.07/\pi$, and adopt a linearly weighted combination of the two bands for intermediate values of $R_{rs}(645)$. Shen et al. (2010) proposed a similar transition approach for deriving [SPM] from satellite data. Although the exact value or range of $R_{rs}(645)$ beyond which the switch to $R_{rs}(859)$ should be made is subject to vary with $b_{bp}(\lambda)/a_p(\lambda)$ and can be achieved in a more rigorous fashion (e.g., Ody et al., 2016), the idea is clear. At the lowest turbidity range ($< \sim 2.5$ FNU) with $R_{rs}(645) < \sim 0.01/\pi$, higher random errors can be seen between the $R_{rs}(645)$ and turbidity data (Dogliotti et al., 2015). Such noise can be reduced by using a green band around 550 nm (e.g., Shen et al., 2010) where $R_{rs}(\lambda)$ assumes appreciable magnitude in waters with low turbidity and does not lose sensitivity until turbidity reaches ~2.4 NTU (Froidefond et al., 2002). In fact, $nL_w(\lambda)$ at around 550 nm has been widely used for detecting terrestrial runoff plumes presumably dominated by minerals (e.g., Nezlin and DiGiacomo, 2005). Strong correlation between $b_{bp}(\lambda)$ and $R_{rs}(\lambda)$ around the green bands is also known for waters with organic-dominated particle assemblages (Stramski et al., 1999). Thus, $R_{rs}(\lambda)$ at the green (~550 nm), red (~645 nm), and NIR (~859 nm), where $a_w(\lambda)$ spans two orders of magnitude from $O(10^{-2})$, to $O(10^{-1})$, and to $O(1)$ m^{-1}, respectively, can be used for deriving

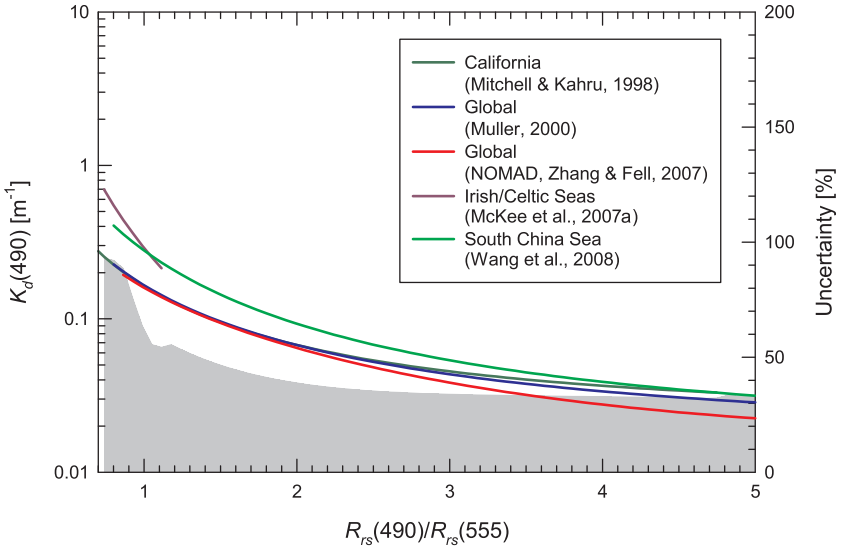

Fig. 10. Regression relationships between coefficient $K_d(490)$ and band ratio of *in situ* measured remote-sensing reflectance. The left-hand axis refers to the colored curves, and the right-hand axis refers to the grey-shaded area. (See above-mentioned references for further information. For interpretation of the references to color in this figure legend, the reader is referred to the web version of this article.)

turbidity of natural waters covering a large dynamic range from < 1 to ~400 NTU/FNU.

4.2.2. Clarity

The reason to define water clarity is to address two aspects of environmental effect of suspended sediment: Light penetration and visual clarity. Light penetration can be characterized by the coefficient $K_d(\lambda)$. We consider $K_d(\lambda)$ as a Tier-3 variable because it can be reliably written as a function of $a(\lambda)$ and $b(\lambda)$ (Kirk, 1984):

$$K_d(\lambda) \approx \sqrt{a(\lambda)[a(\lambda) + (0.473\cos\theta_{sun} - 0.218)b(\lambda)]}/\cos\theta_{sun}, \quad (2)$$

where θ_{sun} here represents the in-water solar zenith angle and varies within 0–48.8°, and therefore the contribution of $b(\lambda)$ to $K_d(\lambda)$ is compromised by a factor of 0.0936–0.255. In practice, many previous formulations of $K_d(\lambda)$ from OCR data, typically at the wavelength of 490 nm − $K_d(490)$, have utilized empirical model approaches (e.g., Austin and Petzold, 1986; Mueller, 2000; Morel et al., 2007). Fig. 10 compares empirical relationships between $K_d(490)$ and the commonly used ratio $R_{rs}(490)/R_{rs}(555)$ based on *in situ* data collected from different regions. Assuming that the largest difference among formulas established for various regions represents uncertainty of using one formula across all regions, we calculated the uncertainty as the maximum difference divided by the average of all relationships. Fig. 10 shows that the uncertainty in $K_d(490)$ derived from the reflectance band ratio is generally ~30% in clear waters, but more than twice as high in coastal waters. The larger uncertainty in turbid waters can be explained by the fact that $R_{rs}(\lambda)$ starts losing sensitivity to increase of turbidity and $K_d(490)$.

Thus, derivation of $K_d(\lambda)$ products in the more complex turbid waters entails algorithms that take into account the issue of sensitivity loss in $R_{rs}(\lambda)$ at short bands. Recent efforts have demonstrated the use of red bands greatly improves the estimation of $K_d(490)$ in turbid coastal waters (see Doron et al., 2007; Wang et al., 2009a). The improvement is expected because the magnitude of $R_{rs}(\lambda)$ in the red bands, when sufficiently high as is the case in turbid waters, indicates to some extent the strength of particulate scattering thereby accounting for a mechanism that is missing when only using blue-to-green reflectance band ratios. However, the mechanistic and potentially most robust way to derive $K_d(\lambda)$ should rely on the theoretical formula such as Eq. (2) using the so-called semi-analytical approaches, which first derive IOPs from $R_{rs}(\lambda)$ and then calculate $K_d(\lambda)$ from the IOPs taking into account sun angle (e.g., Lee et al., 2005, 2013), although there are still uncertainties in the derivation of total $b(\lambda)$ from the satellite-derived $b_b(\lambda)$.

Another important aspect of water clarity is visual clarity, which affects predator-prey interactions, diving activities, and human perception of water quality and fishability. A traditional tool to characterize vertical range of visibility is the Secchi Disk which has a long record dating back to 1865 and provides significant and broad historical context (Wernand, 2010). Preisendorfer (1986) suggests that the depth beyond which Sechi Disk disappears to human eyes is inversely proportional to $c(\lambda) + K_d(\lambda)$; whereas Lee et al. (2015a, 2016) recently argue that the Sechi Disk depth is approximately $\sim 1/K_d^{tr}$, where K_d^{tr} is the diffuse attenuation coefficient at the "transparent window" (minimum diffuse attenuation coefficient) of the water body within the visible domain (410–665 nm). *In situ* observations show that the Sechi Disk depth can differ significantly from the horizontal range of visibility (Steel and Neuhausser, 2002), which is determined by $c(\lambda)$ and is more relevant to underwater visibility (Davies-Colley and Smith, 2001). Several studies have attempted to derive $c(\lambda)$ from $R_{rs}(\lambda)$ (Loisel and Stramski, 2000; Roesler and Boss, 2003; Doron et al., 2007), despite that $R_{rs}(\lambda)$ results primarily from $b_b(\lambda)$ as opposed to total $b(\lambda)$ and $b_b(\lambda)$ is a small and variable portion of $b(\lambda)$. Therefore, a satellite-derived visual clarity product is expected to be subject to this uncertainty. In contrast, light penetration characterized by $K_d(\lambda)$ is a stronger function of $a(\lambda)$ especially at larger sun angles owing to the small weighting factor of $b(\lambda)$. In that regard, we expect that a satellite-derived light penetration product (e.g., $K_d(490)$) should be more robust than a visual clarity product (e.g., $c(\lambda)$).

4.3. Suspended particulate matter

The definitions of both turbidity and clarity are somewhat ambiguous in spite of their environmental significance whereas the [SPM] is more clearly defined. A widely used approach to derive [SPM] is to use also $R_{rs}(645)$ (Hu et al., 2004; Miller and McKee, 2004; Rodríguez-Guzmán and Gilbes-Santaella, 2009; Petus et al., 2010; Ondrusek et al., 2012). Fig. 11 compares several empirical relationships between [SPM] and $R_{rs}(645)$ based on field data from various coastal regions in the world. The observed inter-formula difference is lowest (~50%) for $R_{rs}(645)$ higher than ~0.007 sr^{-1}, and highest (~100%) for $R_{rs}(645)$ lower than ~0.003 sr^{-1}, presumably owing to decreased SNR and increased effect by variations in light absorption coefficient at lower [SPM] (Neil et al., 2011). Note that the level of uncertainty reflected in the inter-formula difference is much higher than that in the turbidity-vs-$R_{rs}(645)$ relationship (Fig. 8), owing largely to the uncertainty of mass-specific optical property of suspended particles (see Section 3.4.1).

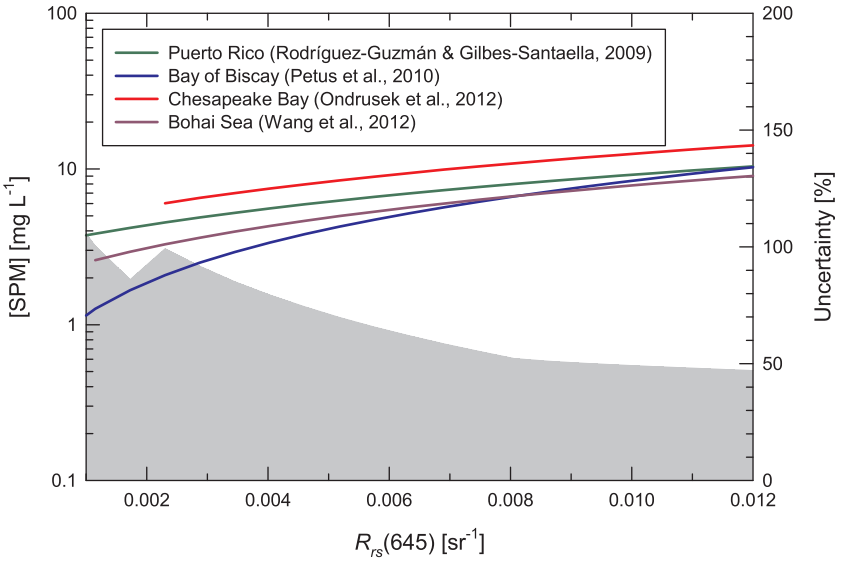

Fig. 11. Regression relationships between [SPM] and *in situ* measured remote-sensing reflectance. The left-hand axis refers to the colored curves, and the right-hand axis refers to the grey-shaded area. (For interpretation of the references to color in this figure legend, the reader is referred to the web version of this article.)

Other empirical algorithms for [SPM] include the use of reflectance band ratios (Doxaran et al., 2002a, 2002b; D'Sa et al., 2007; Zhang et al., 2010), reflectance band difference (Hu et al., 2004), and $R_{rs}(\lambda)$-derived $K_d(490)$ (Son and Wang, 2012). Compared with [SPM] derived from $R_{rs}(\lambda)$ at a single band, these methods generally exhibit improved accuracy owing to cancellation of errors that spectrally covary. From a mechanistic standpoint, however, all empirical algorithms are subject to the same degree of uncertainty induced by the mismatch between materials that contribute significantly to $R_{rs}(\lambda)$ and those that dominate [SPM]. For instance, CDOM is irrelevant to [SPM] but can significantly reduce $R_{rs}(\lambda)$ depending on λ and CDOM concentration. The contribution of phytoplankton pigments to light absorption, and thus to $R_{rs}(\lambda)$, tends to be disproportionately high compared with its contribution to mass of total suspended particles.

Uncertainties associated with such a mismatch can potentially be reduced if a two-step, IOP-based algorithm is used, namely, the inversion of $R_{rs}(\lambda)$ for $b_{bp}(\lambda)$ using semi-analytical models (AOP-to-IOP) followed by derivation of [SPM] from $b_{bp}(\lambda)$ (IOP-to-mass), e.g., (e.g., Zawada et al., 2007; Stramski et al., 2008). Field observations in coastal waters show that the correlation between $b_{bp}(\lambda)$ and [SPM] is often higher than that between $R_{rs}(\lambda)$ and [SPM] (e.g., D'Sa et al., 2007), whereas the difference between these correlations is not appreciable in open ocean waters (Stramski et al., 2008) where optically significant materials tend to covary and the influence from the mismatch is minimized. From a conceptual standpoint, uncertainty associated with particle size distribution and distinct mineral and organic mass-specific scattering coefficients still remains in this two-step approach even if $b_{bp}(\lambda)$ is perfectly derived from $R_{rs}(\lambda)$. In practice, the performance of this two-step approach always depends of course on how well all uncertainty factors are accounted for and the ultimate outcome may not necessarily appear satisfying (e.g., Zawada et al., 2007). In view of these factors, the two-step approach may not necessarily provide superior performance than the empirical band-ratio algorithms. However, the two-step approach is still worth pursuing especially for applications in coastal waters because of the complicated nature of water quality remote-sensing as has been discussed in Section 3, which entails characterizing critical optical processes and properties at a higher level of detail. Knowledge gained with this approach is expected to lead to improved techniques for ocean color inversion and for constraining the variability of mass-specific optical properties, thus continued improvement of the performance of this approach. In addition, another important benefit of the two-step approach is a potential for decoupling the estimation of [SPM] from [Chl-*a*] and CDOM estimates, which is not possible with empirical band-ratio algorithms when different variables are derived from the same band-ratio (Stramski et al., 2008).

One alternative but rarely investigated way to derive [SPM] from remote-sensing data is through the coefficient $a_d(\lambda)$. The reason owes to the difficulty to derive $a_d(\lambda)$ from $R_{rs}(\lambda)$. In fact, in turbid coastal waters $a_d(\lambda)$ often correlates with [SPM] better than $b_{bp}(\lambda)$ or $b_p(\lambda)$ does (Table 5). In 5 out of 6 regions [SPM] exhibits stronger or comparable degree of correlation with particulate absorption $a_d(\lambda)$ than with scattering coefficients $b_{bp}(\lambda)$ or $b_p(\lambda)$. Table 5 also illustrates the decoupling of correlation between $a_d(\lambda)$-vs-[SPM] and $b_{bp}(\lambda)$-vs-[SPM] relationships. Whereas both $a_d(\lambda)$ and $b_{bp}(\lambda)$ correlate well with [SPM] in the Rhode River (Gallegos et al., 1990) and the Mackenzie Estuary (Doxaran et al., 2012; Bélanger et al., 2013), neither are a good predictor of [SPM] in French Guyana (Loisel et al., 2009) (not shown) or Hudson Bay (Xi et al., 2013, 2015). Whereas $b_{bp}(\lambda)$ appears to be a better predictor of [SPM] than $a_d(\lambda)$ in Mississippi estuary (D'Sa et al., 2007), $a_d(\lambda)$ seems significantly more relevant to [SPM] than $b_{bp}(\lambda)$ in Queensland estuaries (Clementson et al., 2007, 2008a, 2008b; Blondeau-Patissier et al., 2009) and Lake Taihu (Zhang, 2008; Sun et al., 2009). The decoupling highlights the fact that particulate absorption and scattering coefficients are driven by different factors (see Sections 3.2.5,3.3.3, and 3.3.4; Figs. 3 and 6). Therefore, the selection of [SPM] predictor should be made on a case-by-case basis depending on particle composition and size distribution. In the case when $a_d(\lambda)$ correlates better than $b_{bp}(\lambda)$ with [SPM], a partitioning model that derives $a_d(\lambda)$ from total $a(\lambda)$ (e.g., Zheng et al., 2015b) may help obtain more accurate [SPM] product.

From an environmental standpoint, the light absorption property $a_d(\lambda)$ of suspended particles might be more relevant to water quality than its mass concentration [SPM]. This idea was proposed by Davies-Colley and Smith (2001) that the magnitude of $a_d(\lambda)$ might indicate the capacity of suspended sediment to adsorb contaminants because light absorption is proportional to the concentration of chemically-adsorbing surface area of particles. However, to our best knowledge we are not aware of concurrent characterization of $a_d(\lambda)$ and adsorptive pollutants, which prevents us from making a conclusive statement on this assumption. This topic also requires further attention and research.

4.4. Chl-a and CDOM

The [Chl-*a*] is another fundamental parameter of water quality, which can be used for detecting algal blooms and assessing eutrophication. The most commonly used approach for estimating [Chl-*a*] from space likewise involves reflectance band ratios. A comparison of various regional formulas deriving [Chl-*a*] from $R_{rs}(490)/R_{rs}(555)$ is shown in Fig. 12a. A large uncertainty on the order of 100% is seen across the selected regions, which highlights the issue of using one single relationship between [Chl-*a*] and reflectance band ratio for different regions or for the same region at different seasons. The issue arises mainly from the overlapping light absorption by non-phytoplankton materials (minerals, organic detritus, and CDOM) which typically do not covary with phytoplankton in coastal and inland waters. Other factors include variations in particulate backscattering coefficient and Chl-specific absorption coefficient. Within a specific region, the coefficient of determination between [Chl-*a*] and $R_{rs}(490)/R_{rs}(555)$ appears to be a strong function of absorption budgets composed of $a_{ph}(\lambda)$, $a_g(\lambda)$, and $a_d(\lambda)$ (Table 6 and Fig. 13). The correlations were generally better for waters with total absorption coefficient dominated by $a_{ph}(\lambda)$ or by $a_g(\lambda)$ that is well correlated with $a_{ph}(\lambda)$ (Fig. 13a), and generally lower for regions with higher contributions of $a_d(\lambda)$ to total absorption (Fig. 13b). Comparisons among empirical relationships

Table 5
The coefficient of determination, R^2, between IOPs and [SPM] in various waters around the world. All regressions were performed on log-transformed data. *N*, number of samples.

Location	$a_d(\lambda)$ vs. [SPM]			$b_{bp}(\lambda)$ vs. [SPM]			$b_p(\lambda)$ vs. [SPM]			Reference
	R^2	*N*	λ [nm]	R^2	*N*	λ [nm]	R^2	*N*	λ [nm]	
Rhode River on Chesapeake Bay	0.87	9	400				0.95	14	720	Gallegos et al. (1990)
Mackenzie Estuary	0.98	98	440	0.98	35	715	0.98	35	555	Doxaran et al. (2012) and Bélanger et al. (2013)
Mississippi Estuary	0.64	51	443	0.87	51	555				D'Sa et al. (2007)
Queensland Estuaries, Australia	0.88	57	443	0.44	97	555				Blondeau-Patissier et al. (2009) Clementson et al. (2007) and Clementson et al. (2008a, 2008b)
Lake Taihu, China	0.83	37	440	0.48	78	532	0.69	78	532	Zhang (2008) and Sun et al. (2009)
Hudson Bay	0.64–0.68	54	440	0.56	98	532	0.32	98	532	Xi et al. (2013, 2015)

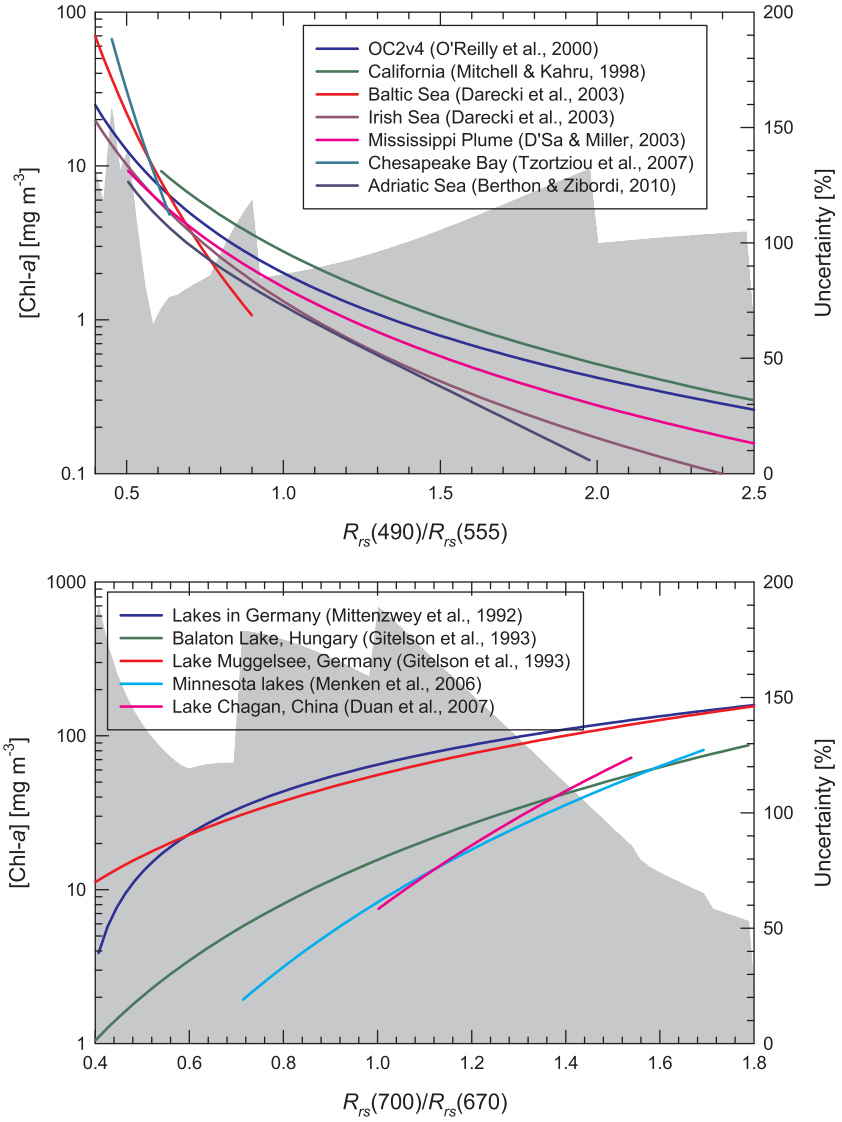

Fig. 12. Regression relationships between [Chl-*a*] and (a) blue-to-green and (b) red band-ratios of *in situ* measured remote-sensing reflectance. The left-hand axis refers to the colored curves, and the right-hand axis refers to the grey-shaded area. (For interpretation of the references to color in this figure legend, the reader is referred to the web version of this article.)

established between CDOM absorption $a_g(\lambda)$ and reflectance band ratios show a similar level of uncertainty (100–120%, Fig. 14) compared with [Chl-*a*] derived from blue-to-green reflectance band-ratios (Fig. 12a).

In the case of high phytoplankton biomass, the use of red bands is advantageous to the blue-green bands in a sense that phytoplankton absorption dwarfs non-phytoplankton absorption in this spectral region (Dall'Olmo et al., 2003, 2005; Gower et al., 2005, 2008; Gitelson et al., 2007, 2009). To use the red band effectively, phytoplankton absorption coefficient must be non-negligible compared with the strong pure water absorption ($O(10^{-1})$ m^{-1}). In addition, it also requires a strong total particulate scattering that outcompetes the total absorption to provide sufficient SNR in $R_{rs}(\lambda)$. These requirements are not too restrictive for application in many productive coastal and inland waters with highly scattering mineral particles. However, the uncertainty in [Chl-*a*] derived from the red bands appears to be even greater than that derived from the blue-to-green bands. Fig. 12b shows empirical relationships established between [Chl-*a*] and $R_{rs}(700)/R_{rs}(670)$ for various inland lakes around the world and a typical level of uncertainty is around 150%. The large variability might be associated with different magnitudes of particulate backscattering coefficient $b_{bp}(\lambda)$ in these lakes.

Unlike [SPM] which is related with total (non-water) IOPs, the [Chl-*a*] and CDOM contribute only a portion to total IOPs and to improve the accuracy of the associated satellite products it is essential to move beyond the reflectance band ratio approach. In this case the overall framework requires one additional step on top of the two-step algorithm, namely the partitioning of total absorption $a(\lambda)$ into various components including $a_{ph}(\lambda)$ (see Section 3.4.2 for variability in the relationship between $a_{ph}(\lambda)$ and [Chl-*a*]) and $a_g(\lambda)$. In this regard, techniques like the one developed by Zheng et al. (2015b) is promising because it treats the partitioning problem on a case-by-case basis, similar to the statistical advantage gained by the ensemble-based approach developed by Cao and Miller (2015). They show that the accuracy of $R_{rs}(\lambda)$-derived $a_g(\lambda)$ can be improved by first categorizing the input $R_{rs}(\lambda)$ into one of several pre-defined ensembles and then applying ensemble-specific parameters to the derivation of $a_g(\lambda)$ from $R_{rs}(\lambda)$.

4.5. Contaminants and pathogens

For quantitative assessment of human health and ecological risks which are of ultimate interest to many water quality managers, the desired targets are pollutants (e.g., nutrients, pesticides, heavy metals) and pathogens (e.g., Fecal Indicator Bacteria (FIB), Vibrios, viruses) (Belkin and Colwell, 2005; Fleming et al., 2006; Johnson et al., 2012) which do not typically dominate $R_{rs}(\lambda)$ and cannot be detected directly by satellite. The most widely used optical proxies for pollutants and pathogens are products associated with suspended particles, e.g., water

Table 6
The coefficient of determination, R^2, between [Chl-a] and reflectance band ratio, $R_{rs}(490)/R_{rs}(555)$, in association with relative contributions and inter-correlations of the three absorption components. $a_{d,n}(443)$, $a_{ph,n}(443)$, and $a_{g,n}(443)$, the absorption coefficients of nonalgal particles, phytoplankton, and CDOM normalized to the sum of the three. All regression analysis were performed on log-transformed data. N, number of samples. NOMAD, NASA bio-Optical Marine Algorithm Dataset.

Location	Median of			Correlation coefficient R			[Chl-a] vs. $R_{rs}(490)/R_{rs}(555)$			Reference
	$a_{d,n}(443)$ [%]	$a_{ph,n}(443)$ [%]	$a_{g,n}(443)$ [%]	$a_{ph,n}(443)$ vs. $a_{d,n}(443)$	$a_{ph,n}(443)$ vs. $a_{g,n}(443)$	$a_{d,n}(443)$ vs. $a_{g,n}(443)$	N	R^2	N	Fit type	
Southeast Pacific	12.6	80.2	6.6	−0.8305	−0.9453	0.6034	20	0.99	31	3rd poly	Bricaud et al. (2010)
Waters off California	7.0	35.2	57.0	0.7160	−0.9896	−0.8089	49	0.96	286	3rd poly	Mitchell and Kahru (1998)
Chukchi Sea	8.1	13.6	77.0	0.4043	−0.9523	−0.6641	32	0.88	22	3rd poly	Matsuoka et al. (2007)
East China Sea	9.4	51.4	38.0	−0.6592	−0.9555	0.4080	26	0.86	38	3rd poly	NOMAD
Labrador Sea	13.6	44.3	43.3	−0.2556*	−0.9066	−0.1762*	44	0.88	13	3rd poly	Cota et al. (2003)
Patagonia Shelf	10.2	66.1	24.6	−0.2583	−0.9092	−0.1674*	96	0.83	72	3rd poly	Ferreira et al. (2009, 2013)
Adriatic Sea	18.5	54.1	25.4	−0.5675	−0.6417	−0.2672*	39	0.77	109	3rd poly	Berthon and Zibordi (2004)
Baltic Sea	19.6	31.1	48.8	−0.2498*	−0.8558	−0.2871	54	0.77	49	3rd poly	Darecki et al. (2003)
Orinoco Estuary	3.5	3.0	91.7	−0.0076*	−0.4397	−0.8948	45	0.58	22	3rd poly	Odriozola et al. (2007)
Chesapeake Bay	33.7	36.0	26.3	−0.6782	−0.5580	−0.2313	90	0.32	40	Linear	Tzortziou et al. (2007)

* Numbers are statistically insignificant.

turbidity, clarity, and [SPM]. Many studies to date have focused on detecting and tracking in space and time the extent of turbid plumes defined with these optical proxies, which can arise from terrestrial discharge or resuspension of sediments (e.g., Walker, 1996; Nezlin et al., 2008; Reifel et al., 2009). This type of studies implies that waters with higher particulate loading are more likely to be contaminant- and pathogen-laden, which is a viable assumption because suspended particles are known to concentrate nutrients (Hirsch, 2012), adsorb pollutants (Uncles et al., 1988; Lick, 2010), and promote pathogen growth (Sherer et al., 1992; Droppo et al., 2009; Johnson et al., 2012). As a first approximation, such an approach provides an estimate of overall likelihood of water contamination. Other satellite-derived optically significant parameters can also be used as proxies of pollutants and pathogens. For instance, the peak of satellite-derived [Chl-a] serves as a precursor of cholera outbreaks in Bay of Bengal and coastal Mozambique (Jutla et al., 2010).

With respect to quantification of contaminant loadings through OCR data, some studies have gone a step further by making coincident optical and environmental measurements in the field (Nezlin et al., 2008; Reifel et al., 2009). However, correlations between what can be directly detected from space versus the specific water quality parameters (e.g., bacteria, toxicity, nutrients) are often weak. This has to do with the fact that high [SPM] is not a sufficient condition for elevated level of pollutants and pathogens. For instance, not all suspended particles are equally effective at inoculating surface water with FIB; it is now known that bottom sediments tend to be more enriched with FIB than terrestrial runoff, and resuspended sediments are the major contributors of elevated FIB concentrations in water (Pachepsky and Shelton, 2011). Sediments are also a known reservoir of pathogenic Vibrios (Johnson et al., 2012; Huehn et al., 2014), which is the most significant human pathogen occurring in seawater (Oliver, 2005). This knowledge sheds light on improving the prediction of the pathogen-related health risks by weighing the impacts of sediment- and runoff-originated plumes differently. Discrimination between the two types of plumes is possible because they are driven by different physical forcings, which has been demonstrated in the upper Chesapeake Bay with the use of wind and streamflow data (Zheng et al., 2015a). This example supports the notion that future capacity-building efforts to monitor and predict contaminants must also address understanding processes that govern the sources and transport of contaminants, pathogens, and suspended particles. More work is also needed in the area of coincident optical and environmental measurements to develop robust optical proxies and indicators for various pollutants and pathogens. That said, the work completed to date has indicated great potential in using OCR data for detection and monitoring of contaminant-laden plumes, particularly in the identification of hotspots, which provides guidance for allocating limited *in situ* sampling resources.

4.6. Eutrophication and hypoxia

Coastal eutrophication is caused by elevated nutrient loading (e.g., nitrogen, phosphorous) from river discharge, wet and dry atmospheric deposition, urban and agricultural terrestrial runoff, and discharge of municipal and industrial wastewater (Cloern, 2001). The [Chl-a] and primary productivity estimated from [Chl-a] can be used to approximate the quantity of nutrient uptake and subsequent assimilation by phytoplankton. The anomaly of phytoplankton biomass and productivity relative to a “norm” (if it can be somehow defined for a given region) can serve as an indicator of eutrophication. There are increasing efforts to incorporate satellite-derived [Chl-a] into coastal eutrophication assessments, often coupled with *in situ* measurements and physical and/or biogeochemical model output (Sørensen et al., 2002; IOCCG, 2008; Banks et al., 2012; Schaeffer et al., 2012). Phytoplankton biomass can also be evaluated with pigment fluorescence signal, although it is a rather qualitative proxy because phytoplankton fluorescence is subject to large variability associated with taxonomic specificity, illumination

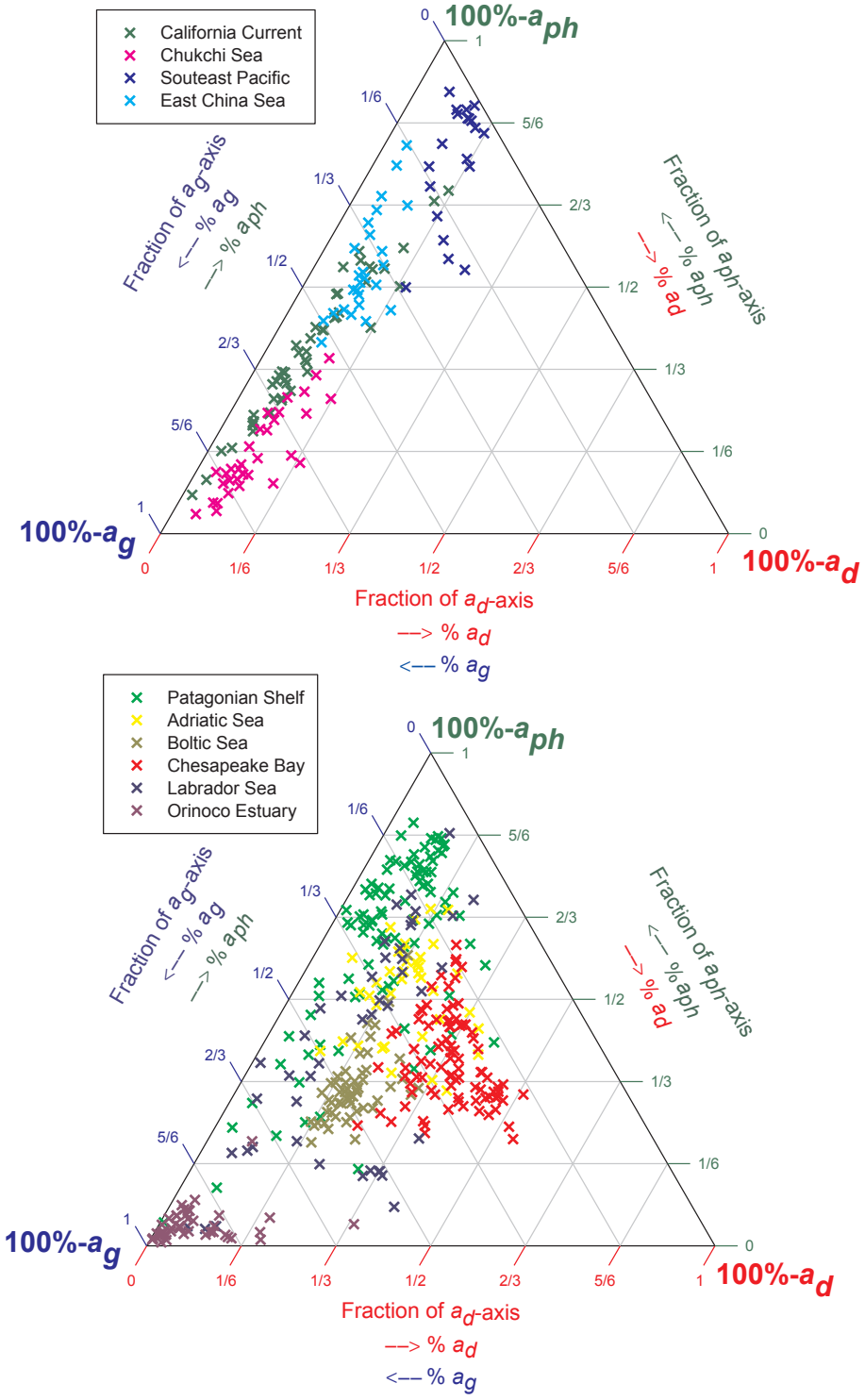

Fig. 13. Contributions of phytoplankton, CDOM, and non-algal particulate absorption coefficients to total non-water absorption for waters with relatively (a) higher and (b) lower degrees of correlation between [Chl-*a*] and R_{rs}(490)/R_{rs}(555). See Table 6 for references of data from each region.

conditions, and nutritional status (Babin et al., 1996). The fluorescence-based approach is applicable in waters with sufficiently low turbidity to avoid "drowning" of fluorescence signal by elastic scattering (see Section 3.2.3). Hu et al. (2015) used fluorescence data to identify phytoplankton blooms within a CDOM-rich plume, which cannot be revealed with reflectance band ratio algorithms because of strong CDOM absorption that makes the water very dark in the blue bands.

Eutrophication is believed to be linked to exacerbated situations of low-oxygen waters known as "hypoxia/anoxia" or "dead zones" (Officer et al., 1984; Rabalais and Turner, 2001; Druon et al., 2004). Hypoxic or anoxic waters are widespread in the world (Diaz and Rosenberg, 2008; Turner et al., 2008; Conley et al., 2011). The dynamics of dissolved oxygen concentration is driven by rate of replenishment arising from algal photosynthesis and vertical entrainment of air or aerated water, and rate of consumption caused by respiration and degradation of organic substance (Officer et al., 1984; Eldridge and Roelke, 2011). Current patterns of hypoxia in a specific region can be a result of historical oxygen depletion that has accumulated over the course of many years (Diaz and Rosenberg, 2008). Therefore, monitoring and prediction of hypoxic waters entail models that take into account all factors detailed above; satellite-derived data such as [Chl-*a*] and surface water temperature are only important inputs to the predictive models.

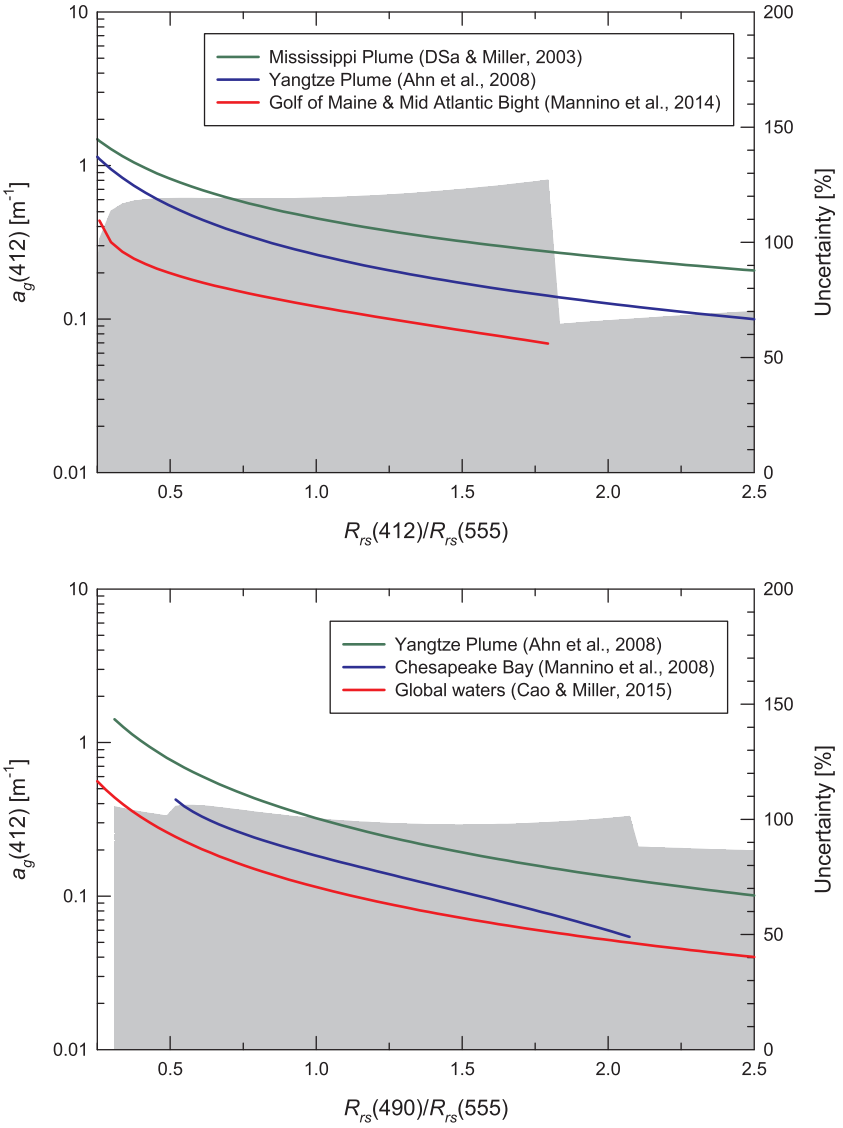

Fig. 14. Regression relationships between CDOM absorption coefficient $a_g(412)$ and (a) purple-to-green and (b) blue-to-green band-ratios of *in situ* measured remote-sensing reflectance. The left-hand axis refers to the colored curves, and the right-hand axis refers to the grey-shaded area. (For interpretation of the references to color in this figure legend, the reader is referred to the web version of this article.)

Anoxic waters sometimes create distinctive optical features that can be directly detected from satellite. Milky blue-green waters formed by upwelled H_2S-rich water, locally referred to as "aoshio", have been affecting Tokyo Bay since the 1950s (Furukawa and Okada, 2006). The unique color was attributed to light scattering by spherical elemental sulfur particles of 0.2–2 μm in diameter and manganese-rich particles with widely varying size and shape, creating reflectance spectra with a maximum at around 550 nm (Takeda et al., 1991). Waters with similar appearance were also observed by satellite off the northern Benguela upwelling system, where massive eruption and subsequent oxidation of H_2S released from sediments produce elemental sulfur particles (Weeks et al., 2004; Ohde et al., 2007; Ohde and Mohrholz, 2011). Oxidation of H_2S may yield particles of other compositions such as gypsum ($CaSO_4{\cdot}2H_2O$), which is common to the Salton Sea in California since the 1970s and plumes of gypsum have been detected remotely even from simple true-color imagery (Tiffany et al., 2007; Reifel et al., 2010). The release of H_2S from sediments is also common to other permanently anoxic systems such as the Baltic Sea, the Black Sea, the Cariaco basin, and the Indian shelves (Middelburg and Levin, 2009; Naqvi et al., 2010). Although we are not aware of demonstration of remote sensing techniques of H_2S-affected waters in these regions, similar milky blue-green waters could in principle occur through similar mechanisms and be detected remotely.

4.7. Harmful algal blooms

Eutrophication sometimes also increases the frequency of HABs by changing the amount and composition of nutrients available in coastal waters (Anderson et al., 2002, 2012; Kemp et al., 2005; Heisler et al., 2008), which have deleterious effects on the coastal marine ecosystem via the production of toxins and depletion of oxygen when they decay. A detailed description on the remote sensing of HABs is beyond the scope of this review and has been overviewed elsewhere (Cullen et al., 1997; Schofield et al., 1999; Stumpf and Tomlinson, 2005; Pettersson and Pozdnyakov, 2013; Bernard et al., 2014).

In short, remote detection of a HAB is possible only if the harmful algal assemblage have a dominant or unique surface optical expression. For example, the hypoxia-causing organism *Aureococcus anophagefferens* can dominate total water optical properties and create "brown tides" (Stumpf and Tomlinson, 2005); "green tides" formed by floating macroalgae are clearly distinguishable from space because the water is largely hidden underneath the algal materials and thus pure water contributes little to light emerging from these waters (Hu, 2009; Shi and Wang, 2009). Some other harmful algae may introduce more subtle optical features which can be more difficult to detect: Bloom waters of Karenia brevis are known to have lower backscattering-to-absorption ratio and are thus darker compared with surrounding waters that have lower concentration of toxic cells (Mahoney, 2003; Schofield et al.,

2006; Cannizzaro et al., 2008); dense Microcystis blooms exhibit distinctive curvature in the red spectral region compared with non-bloom waters (Wynne et al., 2008; Lunetta et al., 2015); toxic Microcystis cells can potentially be distinguished from non-toxic ones because non-toxic cells absorb strongly around 627 nm whereas toxic ones absorb more strongly in the UV (Kardinaal et al., 2007). Furthermore, some HAB species form subsurface blooms which often serve as a reservoir for surface HABs occurrence (Schofield et al., 2006; Seegers et al., 2015) and it is difficult to detect them, although subsurface algal bloom could potentially be detected under specific conditions (Moore et al., 2013) owing to the quenching of fluorescence signal emitted by subsurface phytoplankton bloom (personal communication with R. Kudela).

Perhaps the most difficult type of HAB events to detect and predict are those that are able to produce destructive amount of toxins even at low algal biomass such as the *Karenia spp*, *Alexandrium spp*, and *Pseudonitzschia spp*. In such cases remote sensing techniques can be used to detect ecological and environmental conditions potentially favorable for HAB presence (Tomlinson et al., 2009), e.g., HABs found only during certain times of year, or in specific water masses defined by temperature/salinity, or following certain types of events such as rainfall/discharge. Future research should also look for environmental and optical precursors of HABs for early warning purposes. One potential type of precursor could be changes in component optical properties that consistently occur prior to outbreaks of toxic HABs. Analysis of *in situ* data prior to known HAB events are necessary to make significant progress in this direction.

5. Summary points and future directions

Overall, this contribution has demonstrated the utility, and associated uncertainties, of OCR data and derived products for a variety of water quality applications and services. It is envisioned that OCR data will increasingly provide invaluable information for managers and decision-makers as they attempt to accurately detect, monitor, and forecast the abundance, fate, and transport of contaminants in marine, estuarine, and inland waters, as well as better understand and forecast important coastal phenomena and processes such as HABs, eutrophication, and hypoxia. Below we summarize main points identified in this review and suggest future research directions.

5.1. Summary points

(1) For satellite sensors that have a wide swath with viewing zenith angle tilting up to ~60°, derivation of absorption and backscattering coefficients using water-leaving radiance detected at off-nadir angles can be subject to large errors owing to the anisotropic nature of upwelling light field. This is especially the case for turbid waters, for pixels close to the edge of a swath, and when the solar zenith angle is large. For these scenarios caution must be taken to account for the bidirectional effect with an accuracy suited to the requirements of an application.

(2) Effect of inelastic scattering on $R_{rs}(\lambda)$ can be negligible in turbid waters dominated by nonalgal suspended particles which contribute strong elastic scattering to the total signal. Conversely, fluorescence can be important in waters depleted with nonalgal particles and enriched with phytoplankton or CDOM, such as phytoplankton blooms or clear "tea-colored" plumes.

(3) Although dominated by multiple-scattered photons, $R_{rs}(\lambda)$ correlates robustly with inherent optical properties, namely coefficients $a(\lambda)$ and $b_b(\lambda)$, over a broad range of water turbidity. However, in highly turbid waters the validity of linking backscattering coefficient to $R_{rs}(\lambda)$ needs to be reassessed because the scattering angles that contribute most significantly to apparent backscattering may have shifted to forward angles through accumulation of scattering angles during the multiple-scattering process.

(4) Should red and NIR bands be involved for deriving water quality parameters from $R_{rs}(\lambda)$, it is important to take into account the temperature and salinity dependency as well as measurement uncertainty of $a_w(\lambda)$, especially if waters spanning a large temperature or salinity range are compared, e.g., temperature variation across seasons in temperate regions, or salinity variation along an estuary from freshwater to seawater.

(5) The most important chromophorous agents in natural nonalgal organic materials appear to be proteins and humic matter which includes partially oxidized lignins and tannins; in minerals iron plays a decisive role.

(6) In addition to particle size, shape, and orientation, the light scattering property of mineral particles is determined largely by mineral density; light scattering by organic particles (such as living and dead algal cells, heterotrophic microorganisms, and peat) is affected mainly by water content and density of dry organic materials. In addition, light scattering of algal cells can be disturbed around strong absorption bands and enhanced by presence of internal structures such as gas vacuoles and calcite scales (but not opal shells).

(7) In the visible spectral region, the coefficients $a_g(\lambda)$, $a_d(\lambda)$, and $a_{ph}(\lambda)$ are much more wavelength-dependent than $b_{bp}(\lambda)$. Thus, variation in the spectral shape of $R_{rs}(\lambda)$ in waters dominated by particulate scattering is dictated by absorption coefficients whereas its magnitude reflects a combined effect of both backscattering and absorption coefficients. Consequently, quantification of light absorption spectrum relies on the premise that the troughs in the $R_{rs}(\lambda)$ spectrum sufficiently reflect the "deepness" caused by light absorption. In that regard, higher water turbidity provides more leeway for detection of absorption signal. After all, further increase of absorption coefficient is undetectable if the water-leaving radiance has already been diminished.

(8) The regression relationships between water turbidity and $R_{rs}(\lambda)$ data collected in various locations converge, suggesting that there is great potential to estimate water turbidity around the world from satellite-derived $R_{rs}(\lambda)$ using a single algorithm without the need to tune it based on local optical properties. The potentially large dynamic range in turbidity can be accommodated by using a green, red, and a NIR band where $a_w(\lambda)$ spans two orders of magnitude. The use of green band where $a_w(\lambda)$ is smaller allows sufficient $R_{rs}(\lambda)$ signal when turbidity is low, whereas the use of NIR band with larger $a_w(\lambda)$ essentially provides ample leeway for quantification of higher turbidity in a sense that $R_{rs}(\lambda)$ maintains its sensitivity to turbidity variations because $a_w(\lambda)$ is sufficiently large to impose a meaningful influence that is independent from $a_p(\lambda)$ upon $R_{rs}(\lambda)$.

(9) The degree of correlation between [SPM] and $a_d(\lambda)$ is decoupled from that between [SPM] and $b_{bp}(\lambda)$ or $b_p(\lambda)$ because variability of these optical properties is driven by different factors. Specifically, variability of [SPM]-normalized $a_d(\lambda)$ appears to be driven more by "darkness" of particulate matter and less by particle size, whereas variability of [SPM]-normalized $b_{bp}(\lambda)$ and $b_p(\lambda)$ appears to be driven by density of dry materials, water content in organic materials, and particles size, with generally greater size-dependency when particles are larger. Therefore, the selection of optical proxy of [SPM] from between $a_d(\lambda)$ and $b_{bp}(\lambda)$ should be made on a case-by-case basis.

(10) In turbid waters enriched with nonalgal absorbing particles, the derivation of [Chl-*a*] using the reflectance band ratio approach is subject to large or even unbounded errors owing to nonalgal materials that influence $R_{rs}(\lambda)$ but do not contribute to [Chl-*a*]. For such waters we recommend the derivation of [Chl-*a*] via the route of $R_{rs}(\lambda) \rightarrow a(\lambda) \rightarrow a_{ph}(\lambda) \rightarrow$ [Chl-*a*], which requires robust models that invert the AOP to obtain IOPs and partition total IOPs to components including phytoplankton, as well as knowledge about [Chl-*a*]-specific $a_{ph}(\lambda)$. Although on global scale the [Chl-*a*]-normalized $a_{ph}(\lambda)$ around the blue and red absorption peaks varies

by > 2 orders of magnitude, at any given [Chl-*a*] it rarely exceeds a factor of 5 (perhaps less considering the uncertainties in measurement techniques). This suggests that the magnitude of [Chl-*a*] is an indicator of overall trophic conditions in a specific water body, which constrains the cell size range and variability of intracellular pigments in phytoplankton species acclimated to that water. Thus, the use of a [Chl-*a*]-dependent formula to derive [Chl-*a*] from satellite-derived $a_{ph}(\lambda)$ is a promising direction to pursue.

(11) For waters with light absorption dominated by phytoplankton or by CDOM that is well correlated with phytoplankton, the correlation between reflectance band-ratios and [Chl-*a*] appears to be strong at local scales, which justifies the use of locally-parameterized empirical algorithms to derive [Chl-*a*] in this case.

(12) There is a chance to optically and remotely detect anoxic waters that have come up to the surface or where the sediments underneath release H_2S gas to surface layer. Oxygen oxidation generates elemental sulfur particles and sometimes manganese- or calcium-rich particles depending on water chemistry. The sulfur and mineral particles enhance the light scattering in these waters and create a distinct turquoise color detectable from space.

5.2. Future directions

(1) Ocean color algorithm development continues to be an active area of research. In particular there is the need for more robust atmospheric corrections in coastal regions influenced by absorbing aerosols, for inversion models to derive total IOPs from $R_{rs}(\lambda)$, and for methods to partition total IOPs into components associated with different aspects of water quality.

(2) It is important to develop more direct ecological and water quality parameters of interest to coastal water quality managers and decision-makers. To accomplish this task, optical measurements will have to be made in parallel with characterizations of a variety of water quality issues including toxins, pathogens, priority pollutants, biochemical and chemical oxygen demands, and etc., which necessitates a higher level of collaboration between optical oceanographers and environmental scientists in the future.

(3) Forecasting of autochthonous water quality issues such as HABs will benefit from the identification of optical, ecological, and environmental precursors. In particular, the search for optical precursors may entail examination of subtle spectral features which can be better enabled by hyperspectral sensors.

(4) To differentiate allochthonous issues that do not have distinctive optical features such as contaminants or pathogens attached to sediment plumes, study of environmental processes associated with their source, transport, and transformation is critical. For example, turbid plumes arising from bottom resuspension should raise more concern about pathogen exposure than plumes generated by terrestrial runoffs. Runoff generated over different land covers such as urban, industrial, or agricultural land, likely contains different types of contaminants and pathogens. Progress in detecting and forecasting these water-quality issues will benefit from combinations of ocean color data with dynamic biogeochemical and hydrodynamic modeling.

(5) Estimation of oil thickness at the scale > 0.5 mm is a new research area and much needed for post-spill cleanup purpose. Measurements from the Deep Water Horizon oil spill have revealed great potential for using the NIR and SWIR bands for this purpose. Optical characterization of more petroleum samples from major wells around the world should be conducted. We envision that a global petroleum spectra database can be established; with the availability of such a database and with each tanker registering the extraction location of the oil being carried, oil thickness of future spills can be estimated with algorithms tailored to each type of petroleum and thus better accuracy might be achieved.

Acknowledgements

This work was supported by NOAA's Ocean Remote Sensing (ORS) Program. The contents of this article are solely the opinions of the authors and do not constitute a statement of policy, decision, or position on behalf of the NOAA or the U.S. Government.

References

Aas, E., 1996. Refractive index of phytoplankton derived from its metabolite composition. J. Plankton Res. 18, 2223–2249.
Abrahams, M.V., Kattenfeld, M.G., 1997. The role of turbidity as a constraint on predator-prey interactions in aquatic environments. Behav. Ecol. Sociobiol. 40, 169–174.
Anderson, D., Glibert, P., Burkholder, J., 2002. Harmful algal blooms and eutrophication: Nutrient sources, composition, and consequences. Estuaries 25, 704–726.
Anderson, D.M., Cembella, A.D., Hallegraeff, G.M., 2012. Progress in understanding harmful algal blooms: paradigm shifts and new technologies for research, monitoring, and management. Ann. Rev. Mar. Sci. 4, 143–176.
Antoine, D., Morel, A., Leymarie, E., Houyou, A., Gentili, B., Victori, S., Buis, J.-P., Buis, N., Meunier, S., Canini, M., Crozel, D., Fougnie, B., Henry, P., 2013. Underwater radiance distributions measured with miniaturized multispectral radiance cameras. J. Atmos. Ocean. Technol. 30, 74–95.
Aurin, D.A., Dierssen, H.M., Twardowski, M.S., Roesler, C.S., 2010. Optical complexity in Long Island Sound and implications for coastal ocean color remote sensing. J. Geophys. Res. 115, C07011.
Austin, R.W., Petzold, T.J., 1986. Spectral dependence of the diffuse attenuation coefficient of light in ocean waters. Opt. Eng. 25, 471–479.
Babin, M., Morel, A., Fournier-Sicre, V., Fell, F., Stramski, D., 2003a. Light scattering properties of marine particles in coastal and open ocean waters as related to the particle mass concentration. Limnol. Oceanogr. 48, 843–859.
Babin, M., Morel, A., Gentili, B., 1996. Remote sensing of sea surface sun-induced chlorophyll fluorescence: consequences of natural variations in the optical characteristics of phytoplankton and the quantum yield of chlorophyll a fluorescence. Int. J. Remote Sens. 17, 2417–2448.
Babin, M., Stramski, D., 2004. Variations in the mass-specific absorption coefficient of mineral particles suspended in water. Limnol. Oceanogr. 49, 756–767.
Babin, M., Stramski, D., Ferrari, G.M., Claustre, H., Bricaud, A., Obolensky, G., Hoepffner, N., 2003b. Variations in the light absorption coefficients of phytoplankton, nonalgal particles, and dissolved organic matter in coastal waters around Europe. J. Geophys. Res. 108, 3211.
Balch, W.M., Holligan, P.M., Ackleson, S.G., Voss, K.J., 1991. Biological and optical properties of mesoscale coccolithophore blooms in the Gulf of Maine. Limnol. Oceanogr. 36, 629–643.
Balogh, S.J., Meyer, M.L., Johnson, D.K., 1997. Mercury and suspended sediment loadings in the Lower Minnesota River. Environ. Sci. Technol. 31, 198–202.
Banks, A.C., Prunet, P., Chimot, J., Pina, P., Donnadille, J., Jeansou, E., Lux, M., Petihakis, G., Korres, G., Triantafyllou, G., Fontana, C., Estournel, C., Ulses, C., Fernandez, L., 2012. A satellite ocean color observation operator system for eutrophication assessment in coastal waters. J. Mar. Syst. 94 (Supplement), S2–S15.
Bélanger, S., Cizmeli, S.A., Ehn, J., Matsuoka, A., Doxaran, D., Hooker, S., Babin, M., 2013. Light absorption and partitioning in Arctic Ocean surface waters: impact of multiyear ice melting. Biogeosciences 10, 6433–6452.
Belkin, S., Colwell, R.R. (Eds.), 2005. Oceans and Health: Pathogens in the Marine Environment. Springer.
Bernard, S., Pitcher, G., Evers-King, H., Robertson, L., Matthews, M., Rabagliati, A., Balt, C., 2014. Ocean colour remote sensing of harmful algal blooms in the Benguela system. In: Barale, V., Gade, M. (Eds.), Remote Sensing of the African Seas. Springer, Netherlands, pp. 185–203.
Berthon, J.-F., Zibordi, G., 2004. Bio-optical relationships for the northern Adriatic Sea. Int. J. Remote Sens. 25, 1527–1532.
Binding, C.E., Jerome, J.H., Bukata, R.P., Booty, W.G., 2008. Spectral absorption properties of dissolved and particulate matter in Lake Erie. Remote Sens. Environ. 112, 1702–1711.
Bisson, P.A., Bilby, R.E., 1982. Avoidance of suspended sediment by Juvenile Coho Salmon. North Am. J. Fish. Manag. 2, 371–374.
Blondeau-Patissier, D., Brando, V.E., Oubelkheir, K., Dekker, A.G., Clementson, L.A., Daniel, P., 2009. Bio-optical variability of the absorption and scattering properties of the Queensland inshore and reef waters, Australia. J. Geophys. Res. 114, C05003.
Blondeau-Patissier, D., Gower, J.F.R., Dekker, A.G., Phinn, S.R., Brando, V.E., 2014. A review of ocean color remote sensing methods and statistical techniques for the detection, mapping and analysis of phytoplankton blooms in coastal and open oceans. Prog. Oceanogr. 123, 123–144.
Bohren, C.F., Huffman, D.R., 1983. Absorption and Scattering of Light by Small Particles. Wiley.
Bowers, D.G., Binding, C.E., 2006. The optical properties of mineral suspended particles: a review and synthesis. Estuar. Coast. Shelf Sci. 67, 219–230.
Bowers, D.G., Braithwaite, K.M., Nimmo-Smith, W.A.M., Graham, G.W., 2009. Light scattering by particles suspended in the sea: The role of particle size and density. Cont. Shelf Res. 29, 1748–1755.
Bowers, D.G., Md-Suffian, I., Mitchelson-Jacob, E.G., 2012. Bio-optical properties of east coast Malaysia waters in relation to remote sensing of chlorophyll. Int. J. Remote Sens. 33, 150–169.
Boyle, E.S., Guerriero, N., Thiallet, A., Vecchio, R.D., Blough, N.V., 2009. Optical

properties of humic substances and CDOM: relation to structure. Environ. Sci. Technol. 43, 2262–2268.
Brekke, C., Solberg, A.H.S., 2008. Classifiers and confidence estimation for oil spill detection in ENVISAT ASAR images. Geosci. Remote Sens. Lett., IEEE 5, 65–69.
Bricaud, A., Babin, M., Claustre, H., Ras, J., Tièche, F., 2010. Light absorption properties and absorption budget of Southeast Pacific waters. J. Geophys. Res. 115, C08009.
Bricaud, A., Babin, M., Morel, A., Claustre, H., 1995. Variability in the chlorophyll-specific absorption coefficients of natural phytoplankton: analysis and parameterization. J. Geophys. Res. 100, 13321–13332.
Bricaud, A., Bédhomme, A.-L., Morel, A., 1988. Optical properties of diverse phytoplanktonic species: experimental results and theoretical interpretation. J. Plankton Res. 10, 851–873.
Buiteveld, H., Hakvoort, J.H.M., Donze, M., 1994. Optical properties of pure water. In: In: Jaffe, J.S. (Ed.), Ocean Optics XII Vol. 2258. SPIE, Bergen, Norway, pp. 174–183.
Bulgarelli, B., Djavidnia, S., 2012. On MODIS retrieval of oil spill spectral properties in the marine environment. IEEE Geosci. Remote Sens. Lett. 9, 398–402.
Cannizzaro, J.P., Carder, K.L., Chen, F.R., Heil, C.A., Vargo, G.A., 2008. A novel technique for detection of the toxic dinoflagellate, Karenia brevis, in the Gulf of Mexico from remotely sensed ocean color data. Cont. Shelf Res. 28, 137–158.
Cao, F., Miller, W.L., 2015. A new algorithm to retrieve chromophoric dissolved organic matter (CDOM) absorption spectra in the UV from ocean color. J. Geophys. Res. 120, 496–516.
Carder, K.L., Steward, R.G., Harvey, G.R., Ortner, P.B., 1989. Marine humic and fulvic acids: their effects on remote sensing of ocean chlorophyll. Limnol. Oceanogr. 34, 68–81.
Castillo, C.R., Sarmento, H., Álvarez-Salgado, X.A., Gasol, J.M., Marraséa, C., 2010. Production of chromophoric dissolved organic matter by marine phytoplankton. Limnol. Oceanogr. 55, 446–454.
Chami, M., McKee, D., Leymarie, E., Khomenko, G., 2006. Influence of the angular shape of the volume-scattering function and multiple scattering on remote sensing reflectance. Appl. Opt. 45, 9210–9220.
Chen, Z., Hu, C., Muller-Karger, F., 2007. Monitoring turbidity in Tampa Bay using MODIS/Aqua 250-m imagery. Remote Sens. Environ. 109, 207–220.
Chen, Z., Li, Y., Pan, J., 2004. Distributions of colored dissolved organic matter and dissolved organic carbon in the Pearl River Estuary, China. Cont. Shelf Res. 24, 1845–1856.
Choi, J.-K., Park, Y.J., Ahn, J.H., Lim, H.-S., Eom, J., Ryu, J.-H., 2012. GOCI, the world's first geostationary ocean color observation satellite, for the monitoring of temporal variability in coastal water turbidity. J. Geophys. Res. 117, C09004.
Clark, R.N., Swayze, G.A., Leifer, I., Livo, K.E., Kokaly, R.F., Hoefen, T., Lundeen, S., Eastwood, M., Green, R.O., Pearson, N., Sarture, C., McCubbin, I., Roberts, D., Bradley, E., Steele, D., Ryan, T., Dominguez, R., 2010. A method for quantitative mapping of thick oil spills using imaging spectroscopy, Open-File Report, report number, 2010-1167.
Clementson, L.A., Blondeau-Patissier, D., Brando, V.E., Fitzroy River Estuary February 2008 HPLC Pigment and Ocean Colour Data, Australian-waters Earth Observation Phytoplankton-type products (AEsOP), 2008a. < http://www.marlin.csiro.au/geonetwork/srv/eng/search#!dc570b6f-639c-6d44-e043-08114f8c18bc > .
Clementson, L.A., Daniel, P., Brando, V.E., Great Barrier Reef April 2008 HPLC Pigment and Ocean Colour Data, Australian-waters Earth Observation Phytoplankton-type products (AEsOP), 2008b. < http://www.marlin.csiro.au/geonetwork/srv/eng/search#!dbb7bf86-9eda-0f97-e043-08114f8cc2ac > .
Clementson, L.A., Schroeder, T., Daniel, P., Brando, V.E., Great Barrier Reef September 2007 HPLC Pigment and Ocean Colour Data, Australian-waters Earth Observation Phytoplankton-type products (AEsOP), 2007. < http://www.marlin.csiro.au/geonetwork/srv/eng/search#!dbb7bf86-9edc-0f97-e043-08114f8cc2ac > .
Cloern, J.E., 2001. Our evolving conceptual model of the coastal eutrophication problem. Mar. Ecol. Prog. Ser. 210, 223–253.
Coble, P.G., 2007. Marine optical biogeochemistry: the chemistry of ocean color. Chem. Rev.-Columbus 107, 402–418.
Conley, D.J., Carstensen, J., Aigars, J., Axe, P., Bonsdorff, E., Eremina, T., Haahti, B.-M., Humborg, C., Jonsson, P., Kotta, J., Lännegren, C., Larsson, U., Maximov, A., Medina, M.R., Lysiak-Pastuszak, E., Remeikaitė-Nikienė, N., Walve, J., Wilhelms, S., Zillén, L., 2011. Hypoxia is increasing in the coastal zone of the Baltic Sea. Environ. Sci. Technol. 45, 6777–6783.
Cota, G.F., Harrison, W.G., Platt, T., Sathyendranath, S., Stuart, V., 2003. Bio-optical properties of the Labrador Sea. J. Geophys. Res. 108, 3228.
Cullen, J.J., Ciotti, Á.M., Davis, R.F., Lewis, M.R., 1997. Optical detection and assessment of algal blooms. Limnol. Oceanogr. 42, 1223–1239.
D'Sa, E.J., Miller, R.L., Del Castillo, C., 2006. Bio-optical properties and ocean color algorithms for coastal waters influenced by the Mississippi River during a cold front. Appl. Opt. 45, 7410–7428.
D'Sa, E.J., Miller, R.L., McKee, B.A., 2007. Suspended particulate matter dynamics in coastal waters from ocean color: application to the northern Gulf of Mexico. Geophys. Res. Lett. 34, L23611.
Dall'Olmo, G., Gitelson, A.A., Rundquist, D.C., 2003. Towards a unified approach for remote estimation of chlorophyll-a in both terrestrial vegetation and turbid productive waters. Geophys. Res. Lett. 30, 1938.
Dall'Olmo, G., Gitelson, A.A., Rundquist, D.C., Leavitt, B., Barrow, T., Holz, J.C., 2005. Assessing the potential of SeaWiFS and MODIS for estimating chlorophyll concentration in turbid productive waters using red and near-infrared bands. Remote Sens. Environ. 96, 176–187.
Darecki, M., Weeks, A., Sagan, S., Kowalczuk, P., Kaczmarek, S., 2003. Optical characteristics of two contrasting Case 2 waters and their influence on remote sensing algorithms. Cont. Shelf Res. 23, 237–250.
Davies-Colley, R., Smith, D., 2001. Turbidity, suspended sediment, and water clarity: a review. J. Am. Water Resour. Assoc. 37, 1085–1101.
De Carolis, G., Adamo, M., Pasquariello, G., 2014. On the estimation of thickness of marine oil slicks from sun-glittered, near-infrared MERIS and MODIS imagery: the Lebanon oil spill case study. IEEE Trans. Geosci. Remote Sens. 52, 559–573.
Dekker, A.G., 1993. Detection of optical water quality parameters for eutrophic waters by high resolution remote sensing. Ph.D. Thesis. Vrije Universiteit, Amsterdam.
Dekker, A.G., Schaeffer, B.A., Greb, S., 2015. Toward a global water quality observing and forecasting system. Eos 96.
Del Vecchio, R., Blough, N.V., 2002. Photobleaching of chromophoric dissolved organic matter in natural waters: kinetics and modeling. Mar. Chem. 78, 231–253.
Del Vecchio, R., Blough, N.V., 2004. Spatial and seasonal distribution of chromophoric dissolved organic matter and dissolved organic carbon in the Middle Atlantic Bight. Mar. Chem. 89, 169–187.
Del Vecchio, R., Subramaniam, A., 2004. Influence of the Amazon River on the surface optical properties of the western tropical North Atlantic Ocean. J. Geophys. Res. 109, C11001.
Diaz, R.J., Rosenberg, R., 2008. Spreading dead zones and consequences for marine ecosystems. Science 321, 926–929.
Dierssen, H.M., Zimmerman, R.C., Leathers, R.A., Downes, T.V., Davis, C.O., 2003. Ocean color remote sensing of seagrass and bathymetry in the Bahamas Banks by high-resolution airborne imagery. Limnol. Oceanogr. 48, 444–455.
Digiacomo, P.M., Washburn, L., Holt, B., Jones, B.H., 2004. Coastal pollution hazards in southern California observed by SAR imagery: stormwater plumes, wastewater plumes, and natural hydrocarbon seeps. Mar. Pollut. Bull. 49, 1013–1024.
Dogliotti, A., Ruddick, K., Nechad, B., Doxaran, D., Knaeps, E., 2015. A single algorithm to retrieve turbidity from remotely-sensed data in all coastal and estuarine waters. Remote Sens. Environ. 156, 157–168.
Doron, M., Babin, M., Mangin, A., Hembise, O., 2007. Estimation of light penetration, and horizontal and vertical visibility in oceanic and coastal waters from surface reflectance. J. Geophys. Res. 112, C06003.
Doxaran, D., Ehn, J., Bélanger, S., Matsuoka, A., Hooker, S., Babin, M., 2012. Optical characterisation of suspended particles in the Mackenzie River plume (Canadian Arctic Ocean) and implications for ocean colour remote sensing. Biogeosciences 9, 3213–3229.
Doxaran, D., Froidefond, J.-M., Castaing, P., 2002a. A reflectance band ratio used to estimate suspended matter concentrations in sediment-dominated coastal waters. Int. J. Remote Sens. 23, 5079–5085.
Doxaran, D., Froidefond, J.-M., Lavender, S., Castaing, P., 2002b. Spectral signature of highly turbid waters: application with SPOT data to quantify suspended particulate matter concentrations. Remote Sens. Environ. 81, 149–161.
Droppo, I.G., Liss, S.N., Williams, D., Nelson, T., Jaskot, C., Trapp, B., 2009. Dynamic existence of waterborne pathogens within river sediment compartments. Implications for water quality regulatory affairs. Environ. Sci. Technol. 43, 1737–1743.
Druon, J.-N., Schrimpf, W., Dobricic, S., Stips, A., 2004. Comparative assessment of large-scale marine eutrophication: North Sea area and Adriatic Sea as case studies. Mar. Ecol. Prog. Ser. 272, 1–23.
Drusch, M., Del Bello, U., Carlier, S., Colin, O., Fernandez, V., Gascon, F., Hoersch, B., Isola, C., Laberinti, P., Martimort, P., Meygret, A., Spoto, F., Sy, O., Marchese, F., Bargellini, P., 2012. Sentinel-2: ESA's optical high-resolution mission for GMES operational services. Remote Sens. Environ. 120, 25–36.
Dubelaar, G.B., Visser, J.W., Donze, M., 1987. Anomalous behaviour of forward and perpendicular light scattering of a cyanobacterium owing to intracellular gas vacuoles. Cytometry 8, 405–412.
Eldridge, P.M., Roelke, D.L., 2011. Hypoxia in waters of the coastal zone: causes, effects, and modeling approaches. In: Wolanski, E., McLusky, D. (Eds.), Treatise on Estuarine and Coastal Science. Academic Press, Waltham, pp. 193–215.
Eplee, R.E., Meister, G., Patt, F.S., Barnes, R.A., Bailey, S.W., Franz, B.A., McClain, C.R., 2012. On-orbit calibration of SeaWiFS. Appl. Opt. 51, 8702–8730.
Estapa, M.L., Boss, E., Mayer, L.M., Roesler, C.S., 2012. Role of iron and organic carbon in mass-specific light absorption by particulate matter from Louisiana coastal waters. Limnol. Oceanogr. 57, 97–112.
Fabricius, K.E., 2005. Effects of terrestrial runoff on the ecology of corals and coral reefs: review and synthesis. Mar. Pollut. Bull. 50, 125–146.
Ferrari, G.M., Dowell, M.D., Grossi, S., Targa, C., 1996. Relationship between the optical properties of chromophoric dissolved organic matter and total concentration of dissolved organic carbon in the southern Baltic Sea region. Mar. Chem. 55, 299–316.
Ferreira, A., Garcia, C.A.E., Dogliotti, A.I., Garcia, V.M.T., 2013. Bio-optical characteristics of the Patagonia Shelf break waters: Implications for ocean color algorithms. Remote Sens. Environ. 136, 416–432.
Ferreira, A., Garcia, V.M.T., Garcia, C.A.E., 2009. Light absorption by phytoplankton, non-algal particles and dissolved organic matter at the Patagonia shelf-break in spring and summer. Deep Sea Res. Part I 56, 2162–2174.
Fichot, C.G., Benner, R., 2011. A novel method to estimate DOC concentrations from CDOM absorption coefficients in coastal waters. Geophys. Res. Lett. 38, L03610.
Fichot, C.G., Benner, R., 2012. The spectral slope coefficient of chromophoric dissolved organic matter (S275–295) as a tracer of terrigenous dissolved organic carbon in river-influenced ocean margins. Limnol. Oceanogr. 57, 1453–1466.
Fingas, M., 2014. Handbook of Oil Spill Science and Technology. Wiley.
Fingas, M., Brown, C., 2014. Review of oil spill remote sensing. Mar. Pollut. Bull. 83, 9–23.
Fleming, L.E., Broad, K., Clement, A., Dewailly, E., Elmir, S., Knap, A., Pomponi, S.A., Smith, S., Solo Gabriele, H., Walsh, P., 2006. Oceans and human health: emerging public health risks in the marine environment. Mar. Pollut. Bull. 53, 545–560.
Forget, P., Broche, P., Naudin, J.-J., 2001. Reflectance sensitivity to solid suspended sediment stratification in coastal water and inversion: a case study. Remote Sens. Environ. 77, 92–103.

Fournier, G.R., Forand, J.L., 1994. Analytic phase function for ocean water. In: In: Jaffe, J.S. (Ed.), Ocean Optics XII Vol. 2258. SPIE, Bergen, Norway, pp. 194–201.
Froidefond, J.M., Lavender, S., Laborde, P., Herbland, A., Lafon, V., 2002. SeaWiFS data interpretation in a coastal area in the Bay of Biscay. Int. J. Remote Sens. 23, 881–904.
Furukawa, K., Okada, T., 2006. Tokyo Bay: its environmental status—past, present, and future. In: Wolanski, E. (Ed.), The Environment in Asia Pacific Harbours. Springer, Netherlands, pp. 15–34.
Gallegos, C.L., Correll, D.L., Pierce, J.W., 1990. Modeling spectral diffuse attenuation, absorption, and scattering coefficients in a turbid estuary. Limnol. Oceanogr. 35, 1486–1502.
GEO, 2007. GEO Inland and Nearshore Coastal Water Quality Remote Sensing Workshop final report. Geneva, Switzerland.
GEO, 2011. Progress Report on GEO Inland and Near-Coastal Water Quality Remote Sensing Working Group. Frascati, Italy.
Gilerson, A., Zhou, J., Hlaing, S., Ioannou, I., Schalles, J., Gross, B., Moshary, F., Ahmed, S., 2007. Fluorescence component in the reflectance spectra from coastal waters. Dependence on water composition. Opt. Express 15, 15702–15721.
Gitelson, A.A., Gurlin, D., Moses, W.J., Barrow, T., 2009. A bio-optical algorithm for the remote estimation of the chlorophyll-a concentration in case 2 waters. Environ. Res. Lett. 4, 045003.
Gitelson, A.A., Schalles, J.F., Hladik, C.M., 2007. Remote chlorophyll-a retrieval in turbid, productive estuaries: Chesapeake Bay case study. Remote Sens. Environ. 109, 464–472.
Gleason, A.C.R., Voss, K.J., Gordon, H.R., Twardowski, M., Sullivan, J., Trees, C., Weidemann, A., Berthon, J.-F., Clark, D., Lee, Z.-P., 2012. Detailed validation of the bidirectional effect in various Case I and Case II waters. Opt. Express 20, 7630–7645.
Gordon, H.R., 1979. Diffuse reflectance of the ocean: the theory of its augmentation by chlorophyll a fluorescence at 685 nm. Appl. Opt. 18, 1161–1166.
Gordon, H.R., 1999. Contribution of Raman scattering to water-leaving radiance: a re-examination. Appl. Opt. 38, 3166–3174.
Gordon, H.R., Brown, O.B., Evans, R.H., Brown, J.W., Smith, R.C., Baker, K.S., Clark, D.K., 1988. A semianalytic radiance model of ocean color. J. Geophys. Res.: Atmos. 93, 10909–10924.
Gordon, H.R., McCluney, W.R., 1975. Estimation of the depth of sunlight penetration in the sea for remote sensing. Appl. Opt. 14, 413–416.
Gordon, H.R., Wang, M., 1994. Retrieval of water-leaving radiance and aerosol optical thickness over the oceans with SeaWiFS: a preliminary algorithm. Appl. Opt. 33, 443–452.
Gower, J., King, S., Borstad, G., Brown, L., 2005. Detection of intense plankton blooms using the 709 nm band of the MERIS imaging spectrometer. Int. J. Remote Sens. 26, 2005–2012.
Gower, J., King, S., Borstad, G., Brown, L., 2008. The importance of a band at 709 nm for interpreting water-leaving spectral radiance. Can. J. Remote. Sens. 34, 287–295.
Gower, J.F.R., Borstad, G.A., 1990. Mapping of phytoplankton by solar-stimulated fluorescence using an imaging spectrometer. Int. J. Remote Sens. 11, 313–320.
Gower, J.F.R., Doerffer, R., Borstad, G.A., 1999. Interpretation of the 685nm peak in water-leaving radiance spectra in terms of fluorescence, absorption and scattering, and its observation by MERIS. Int. J. Remote Sens. 20, 1771–1786.
Green, S.A., Blough, N.V., 1994. Optical absorption and fluorescence properties of chromophoric dissolved organic matter in natural waters. Limnol. Oceanogr. 39, 1903–1916.
Hawes, S.K., Carder, K.L., Harvey, G.R., 1992. Quantum fluorescence efficiencies of fulvic and humic acids: effects on ocean color and fluorometric detection. In: In: Gilbert, G.D. (Ed.), Ocean Optics XI Vol. 1750. pp. 212–223 San Diego, CA.
Heisler, J., Glibert, P.M., Burkholder, J.M., Anderson, D.M., Cochlan, W., Dennison, W.C., Dortch, Q., Gobler, C.J., Heil, C.A., Humphries, E., Lewitus, A., Magnien, R., Marshall, H.G., Sellner, K., Stockwell, D.A., Stoecker, D.K., Suddleson, M., 2008. Eutrophication and harmful algal blooms: A scientific consensus. Harmful Algae 8, 3–13.
Helms, J.R., Stubbins, A., Ritchie, J.D., Minor, E.C., Kieber, D.J., Mopper, K., 2008. Absorption spectral slopes and slope ratios as indicators of molecular weight, source, and photobleaching of chromophoric dissolved organic matter. Limnol. Oceanogr. 53, 955–969.
Hirsch, R.M., 2012. Flux of nitrogen, phosphorus, and suspended sediment from the Susquehanna River basin to the Chesapeake Bay during Tropical Storm Lee, September 2011, as an indicator of the effects of reservoir sedimentation on water quality: US Department of the Interior, US Geological Survey.
Hu, C., 2009. A novel ocean color index to detect floating algae in the global oceans. Remote Sens. Environ. 113, 2118–2129.
Hu, C., Barnes, B.B., Qi, L., Corcoran, A.A., 2015. A harmful algal bloom of Karenina brevis in the northeastern gulf of Mexico as revealed by MODIS and VIIRS: a comparison. Sensors 15, 2873–2887.
Hu, C., Chen, Z., Clayton, T.D., Swarzenski, P., Brock, J.C., Muller-Karger, F.E., 2004. Assessment of estuarine water-quality indicators using MODIS medium-resolution bands: initial results from Tampa Bay, FL. Remote Sens. Environ. 93, 423–441.
Hu, C., Li, X., Pichel, W.G., Muller-Karger, F.E., 2009. Detection of natural oil slicks in the NW Gulf of Mexico using MODIS imagery. Geophys. Res. Lett. 36, L01604.
Hu, C., Muller-Karger, F.E., Taylor, C., Carder, K.L., Kelble, C., Johns, E., Heil, C.A., 2005. Red tide detection and tracing using MODIS fluorescence data: a regional example in SW Florida coastal waters. Remote Sens. Environ. 97, 311–321.
Hu, C., Müller-Karger, F.E., Taylor, C., Myhre, D., Murch, B., Odriozola, A.L., Godoy, G., 2003. MODIS detects oil spills in Lake Maracaibo, Venezuela. Eos, Trans. Am. Geophys. Union 84, 313–319.
Huehn, S., Eichhorn, C., Urmersbach, S., Breidenbach, J., Bechlars, S., Bier, N., Alter, T., Bartelt, E., Frank, C., Oberheitmann, B., Gunzer, F., Brennholt, N., Böer, S., Appel, B., Dieckmann, R., Strauch, E., 2014. Pathogenic vibrios in environmental, seafood and clinical sources in Germany. Int. J. Med. Microbiol. 304, 843–850.
Huot, Y., Brown, C.A., Cullen, J.J., 2007. Retrieval of phytoplankton biomass from simultaneous inversion of reflectance, the diffuse attenuation coefficient, and Sun-induced fluorescence in coastal waters. J. Geophys. Res. 112, C06013.
IOCCG, 2008. Why Ocean Colour?: The Societal Benefits of Ocean-colour Technology, Reports of the International Ocean-Colour Coordinating Group, report number, 7.
IOCCG, 2010. Atmospheric Correction for Remotely-Sensed Ocean-Colour Products, Reports of the International Ocean-Colour Coordinating Group, report number, 10.
IOCCG, 2012a. Mission requirements for future ocean-colour sensors, Reports of the International Ocean-Colour Coordinating Group, report number, 13.
IOCCG, 2012b. Ocean-colour observations from a geostationary orbit, Reports of the International Ocean-Colour Coordinating Group, report number, 12.
Irons, J.R., Dwyer, J.L., Barsi, J.A., 2012. The next landsat satellite: the landsat data continuity mission. Remote Sens. Environ. 122, 11–21.
Islam, S.M., Tanaka, M., 2004. Impacts of pollution on coastal and marine ecosystems including coastal and marine fisheries and approach for management: a review and synthesis. Mar. Pollut. Bull. 48, 624–649.
ISO, 1999. ISO 7027: Water quality—Determination of turbidity. International Organization for Standardization.
Jerome, J.H., Bukata, R.P., Miller, J.R., 1996. Remote sensing reflectance and its relationship to optical properties of natural waters. Int. J. Remote Sens. 17, 3135–3155.
Johnson, C.N., Bowers, J.C., Griffitt, K.J., Molina, V., Clostio, R.W., Pei, S., Laws, E., Paranjpye, R.N., Strom, M.S., Chen, A., Hasan, N.A., Huq, A., Noriea, N.F., Grimes, D.J., Colwell, R.R., 2012. Ecology of Vibrio parahaemolyticus and Vibrio vulnificus in the Coastal and Estuarine Waters of Louisiana, Maryland, Mississippi, and Washington (United States). Appl. Environ. Microbiol. 78, 7249–7257.
Jonasz, M., Fournier, G., 2011. Light Scattering by Particles in Water: Theoretical and Experimental Foundations. Elsevier Science.
Jutla, A.S., Akanda, A.S., Islam, S., 2010. Tracking cholera in coastal regions using satellite observations. JAWRA J. Am. Water Resour. Assoc. 46, 651–662.
Kahru, M., Mitchell, B.G., 1998. Spectral reflectance and absorption of a massive red tide off southern California. J. Geophys. Res. 103, 21601–21609.
Kardinaal, W.E.A., Tonk, L., Janse, I., Hol, S., Slot, P., Huisman, J., Visser, P.M., 2007. Competition for light between toxic and nontoxic strains of the harmful cyanobacterium Microcystis. Appl. Environ. Microbiol. 73, 2939–2946.
Karydis, M., Kitsiou, D., 2013. Marine water quality monitoring: a review. Mar. Pollut. Bull. 77, 23–36.
Kemp, W.M., Boynton, W.R., Adolf, J.E., Boesch, D.F., Boicourt, W.C., Brush, G., Cornwell, J.C., Fisher, T.R., Glibert, P.M., Hagy, J.D., 2005. Eutrophication of Chesapeake Bay: historical trends and ecological interactions. Mar. Ecol. Prog. Ser. 303, 1–29.
Kirk, J., 1984. Dependence of relationship between inherent and apparent optical properties of water on solar altitude. Limnol. Oceanogr. 29, 350–356.
Klemer, A.R., Cullen, J.J., Mageau, M.T., Hanson, K.M., Sundell, R.A., 1996. Cyanobacterial buoyancy regulation: the paradoxical roles of carbon. J. Phycol. 32, 47–53.
Kowalczuk, P., Cooper, W.J., Durako, M.J., Kahn, A.E., Gonsior, M., Young, H., 2010. Characterization of dissolved organic matter fluorescence in the South Atlantic Bight with use of PARAFAC model: relationships between fluorescence and its components, absorption coefficients and organic carbon concentrations. Mar. Chem. 118, 22–36.
Kutser, T., Metsamaa, L., Dekker, A.G., 2008. Influence of the vertical distribution of cyanobacteria in the water column on the remote sensing signal. Estuar. Coast. Shelf Sci. 78, 649–654.
Le, C., Li, Y., Zha, Y., Sun, D., 2009. Specific absorption coefficient and the phytoplankton package effect in Lake Taihu, China. Hydrobiologia 619, 27–37.
Lee, Z.-P., Darecki, M., Carder, K.L., Davis, C.O., Stramski, D., Rhea, W.J., 2005. Diffuse attenuation coefficient of downwelling irradiance: an evaluation of remote sensing methods. J. Geophys. Res. 110, C02017.
Lee, Z., Carder, K.L., Mobley, C.D., Steward, R.G., Patch, J.S., 1998. Hyperspectral remote sensing for shallow waters. I. A semianalytical model. Appl. Opt. 37, 6329–6338.
Lee, Z., Carder, K.L., Mobley, C.D., Steward, R.G., Patch, J.S., 1999. Hyperspectral remote sensing for shallow waters: 2. Deriving bottom depths and water properties by optimization. Appl. Opt. 38, 3831–3843.
Lee, Z., Hu, C., Shang, S., Du, K., Lewis, M., Arnone, R., Brewin, R., 2013. Penetration of UV-visible solar radiation in the global oceans: Insights from ocean color remote sensing. J. Geophys. Res. 118, 4241–4255.
Lee, Z., Shang, S., Hu, C., Du, K., Weidemann, A., Hou, W., Lin, J., Lin, G., 2015a. Secchi disk depth: A new theory and mechanistic model for underwater visibility. Remote Sens. Environ. 169, 139–149.
Lee, Z., Shang, S., Qi, L., Yan, J., Lin, G., 2016. A semi-analytical scheme to estimate Secchi-disk depth from Landsat-8 measurements. Remote Sens. Environ. 177, 101–106.
Lee, Z., Wei, J., Voss, K., Lewis, M., Bricaud, A., Huot, Y., 2015b. Hyperspectral absorption coefficient of "pure" seawater in the range of 350–550 nm inverted from remote sensing reflectance. Appl. Opt. 54, 546–558.
Lei, H., Pan, D., Bai, Y., Tao, B., Sun, J., Zhang, L., Zhang, X., 2012. The proportions and variations of the light absorption coefficients of major ocean color components in the East China Sea. Acta Oceanol. Sin. 31, 45–61.
Leifer, I., Lehr, W.J., Simecek-Beatty, D., Bradley, E., Clark, R., Dennison, P., Hu, Y., Matheson, S., Jones, C.E., Holt, B., Reif, M., Roberts, D.A., Svejkovsky, J., Swayze, G., Wozencraft, J., 2012. State of the art satellite and airborne marine oil spill remote sensing: application to the BP Deepwater Horizon oil spill. Remote Sens. Environ. 124, 185–209.
Lick, W., 2010. Sediment and Contaminant Transport in Surface Waters. CRC Press.
Loisel, H., Mériaux, X., Poteau, A., Artigas, L.F., Lubac, B., Gardel, A., Caillaud, J., Lesourd, S., 2009. Analyze of the inherent optical properties of French guiana coastal

waters for remote sensing applications. J. Coastal Res. 1532–1536.
Loisel, H., Nicolas, J.-M., Sciandra, A., Stramski, D., Poteau, A., 2006. Spectral dependency of optical backscattering by marine particles from satellite remote sensing of the global ocean. J. Geophys. Res. 111, C09024.
Loisel, H., Stramski, D., 2000. Estimation of the inherent optical properties of natural waters from the irradiance attenuation coefficient and reflectance in the presence of Raman scattering. Appl. Opt. 39, 3001–3011.
Loiselle, S.A., Bracchini, L., Dattilo, A.M., Ricci, M., Tognazzi, A., Cózar, A., Rossi, C., 2009. The optical characterization of chromophoric dissolved organic matter using wavelength distribution of absorption spectral slopes. Limnol. Oceanogr. 54, 590–597.
Longstaff, B.J., Dennison, W.C., 1999. Seagrass survival during pulsed turbidity events: the effects of light deprivation on the seagrasses Halodule pinifolia and Halophila ovalis. Aquat. Bot. 65, 105–121.
Lorenzoni, L., Toro-Farmer, G., Varela, R., Guzman, L., Rojas, J., Montes, E., Muller-Karger, F., 2015. Characterization of phytoplankton variability in the Cariaco Basin using spectral absorption, taxonomic and pigment data. Remote Sens. Environ. 167, 259–268.
Lucke, R.L., Corson, M., McGlothlin, N.R., Butcher, S.D., Wood, D.L., Korwan, D.R., Li, R.R., Snyder, W.A., Davis, C.O., Chen, D.T., 2011. Hyperspectral Imager for the Coastal Ocean: instrument description and first images. Appl. Opt. 50, 1501–1516.
Lunetta, R.S., Schaeffer, B.A., Stumpf, R.P., Keith, D., Jacobs, S.A., Murphy, M.S., 2015. Evaluation of cyanobacteria cell count detection derived from MERIS imagery across the eastern USA. Remote Sens. Environ. 157, 24–34.
Mahoney, K.L., 2003. Backscattering of light by Karenia brevis and implications for optical detection and monitoring, Dissertation. University of Southern Mississippi.
Mannino, A., Russ, M.E., Hooker, S.B., 2008. Algorithm development and validation for satellite-derived distributions of DOC and CDOM in the US Middle Atlantic Bight. J. Geophys. Res. 113, C07051.
Mason, J.D., Cone, M.T., Fry, E.S., 2016. Ultraviolet (250–550 nm) absorption spectrum of pure water. Appl. Opt. 55, 7163–7172.
Matsuoka, A., Bricaud, A., Benner, R., Para, J., Sempéré, R., Prieur, L., Bélanger, S., Babin, M., 2012. Tracing the transport of colored dissolved organic matter in water masses of the Southern Beaufort Sea: relationship with hydrographic characteristics. Biogeosciences 9, 925–940.
Matsuoka, A., Huot, Y., Shimada, K., Saitoh, S.I., Babin, M., 2007. Bio-optical characteristics of the western Arctic Ocean: implications for ocean color algorithms. Can. J. Remote. Sens. 33, 503–518.
Matthews, M., Bernard, S., 2013. Using a two-layered sphere model to investigate the impact of gas vacuoles on the inherent optical properties of Microcystis aeruginosa. Biogeosciences 10, 8139–8157.
Matthews, M.W., 2011. A current review of empirical procedures of remote sensing in inland and near-coastal transitional waters. Int. J. Remote Sens. 32, 6855–6899.
McKee, D., Cunningham, A., Dudek, A., 2007a. Optical water type discrimination and tuning remote sensing band-ratio algorithms: Application to retrieval of chlorophyll and Kd(490) in the Irish and Celtic Seas. Estuar. Coast. Shelf Sci. 73, 827–834.
McKee, D., Cunningham, A., Wright, D., Hay, L., 2007b. Potential impacts of nonalgal materials on water-leaving Sun induced chlorophyll fluorescence signals in coastal waters. Appl. Opt. 46, 7720–7729.
McKee, D., Röttgers, R., Neukermans, G., Calzado, V.S., Trees, C., Ampolo-Rella, M., Neil, C., Cunningham, A., 2014. Impact of measurement uncertainties on determination of chlorophyll-specific absorption coefficient for marine phytoplankton. J. Geophys. Res. 119, 9013–9025.
Middelburg, J.J., Levin, L.A., 2009. Coastal hypoxia and sediment biogeochemistry. Biogeosciences 6, 1273–1293.
Mie, G., 1976. Contributions to the Optics of Turbid Media: Particularly of Colloidal Metal Solutions. H.M.S.O, London.
Miller, R.L., McKee, B.A., 2004. Using MODIS Terra 250 m imagery to map concentrations of total suspended matter in coastal waters. Remote Sens. Environ. 93, 259–266.
Mitchell, B.G., Kahru, M., 1998. Algorithms for SeaWiFS standard products developed with the CalCOFI bio-optical data set. CALCOFI reports 39, 133–147.
Mobley, C.D., 1994. Light and Water: Radiative Transfer in Natural Waters. Academic Press.
Mobley, C.D., Sundman, L.K., Davis, C.O., Bowles, J.H., Downes, T.V., Leathers, R.A., Montes, M.J., Bissett, W.P., Kohler, D.D.R., Reid, R.P., Louchard, E.M., Gleason, A., 2005. Interpretation of hyperspectral remote-sensing imagery by spectrum matching and look-up tables. Appl. Opt. 44, 3576–3592.
Moore, K., Broughton, J., Kudela, R., 2013. Remote sensing of Akashiwo sanguinea in the vertical column. AGU Fall Meeting Abstracts, Vol. 1 (p. 1742).
Moore, K.A., Wetzel, R.L., 2000. Seasonal variations in eelgrass (Zostera marina L.) responses to nutrient enrichment and reduced light availability in experimental ecosystems. J. Exp. Mar. Biol. Ecol. 244, 1–28.
Morel, A., Antoine, D., Gentili, B., 2002. Bidirectional reflectance of oceanic waters: accounting for Raman emission and varying particle scattering phase function. Appl. Opt. 41, 6289–6306.
Morel, A., Bricaud, A., 1986. Inherent optical properties of algal cells including picoplankton: theoretical and experimental results. Can. Bull. Fish. Aquat. Sci. 214, 521–559.
Morel, A., Gentili, B., 1993. Diffuse reflectance of oceanic waters. II. Bidirectional aspects. Appl. Opt. 32, 6864–6879.
Morel, A., Gentili, B., 1996. Diffuse reflectance of oceanic waters. III. Implication of bidirectionality for the remote-sensing problem. Appl. Opt. 35, 4850–4862.
Morel, A., Huot, Y., Gentili, B., Werdell, P.J., Hooker, S.B., Franz, B.A., 2007. Examining the consistency of products derived from various ocean color sensors in open ocean (Case 1) waters in the perspective of a multi-sensor approach. Remote Sens. Environ. 111, 69–88.
Mouw, C.B., Greb, S., Aurin, D., DiGiacomo, P.M., Lee, Z., Twardowski, M., Binding, C., Hu, C., Ma, R., Moore, T., Moses, W., Craig, S.E., 2015. Aquatic color radiometry remote sensing of coastal and inland waters: Challenges and recommendations for future satellite missions. Remote Sens. Environ. 160, 15–30.
Mueller, J.L., 2000. SeaWiFS algorithm for the diffuse attenuation coefficient, K (490), using water-leaving radiances at 490 and 555 nm. SeaWiFS postlaunch calibration and validation analyses, part, 3, 24-27.
Naqvi, S.W.A., Bange, H.W., Farías, L., Monteiro, P.M.S., Scranton, M.I., Zhang, J., 2010. Marine hypoxia/anoxia as a source of CH_4 and N_2O. Biogeosciences 7, 2159–2190.
Neil, C., Cunningham, A., McKee, D., 2011. Relationships between suspended mineral concentrations and red-waveband reflectances in moderately turbid shelf seas. Remote Sens. Environ. 115, 3719–3730.
Nelson, N.B., Carlson, C.A., Steinberg, D.K., 2004. Production of chromophoric dissolved organic matter by Sargasso Sea microbes. Mar. Chem. 89, 273–287.
Neukermans, G., Loisel, H., Mériaux, X., Astoreca, R., McKee, D., 2012. In situ variability of mass-specific beam attenuation and backscattering of marine particles with respect to particle size, density, and composition. Limnol. Oceanogr. 57, 124–144.
Neukermans, G., Reynolds, R.A., Stramski, D., 2014. Contrasting inherent optical properties and particle characteristics between an under-ice phytoplankton bloom and open water in the Chukchi Sea. Deep Sea Res. Part II 105, 59–73.
Neukermans, G., Reynolds, R.A., Stramski, D., 2016. Optical classification and characterization of marine particle assemblages within the western Arctic Ocean. Limnol. Oceanogr. 61, 1472–1494.
Neville, R., Gower, J., 1977. Passive remote sensing of phytoplankton via chlorophyll α fluorescence. J. Geophys. Res. 82, 3487–3493.
Newcombe, C.P., Macdonald, D.D., 1991. Effects of Suspended Sediments on Aquatic Ecosystems. North Am. J. Fish. Manag. 11, 72–82.
Nezlin, N.P., DiGiacomo, P.M., 2005. Satellite ocean color observations of stormwater runoff plumes along the San Pedro Shelf (southern California) during 1997–2003. Cont. Shelf Res. 25, 1692–1711.
Nezlin, N.P., DiGiacomo, P.M., Diehl, D.W., Jones, B.H., Johnson, S.C., Mengel, M.J., Reifel, K.M., Warrick, J.A., Wang, M., 2008. Stormwater plume detection by MODIS imagery in the southern California coastal ocean. Estuar. Coast. Shelf Sci. 80, 141–152.
Odermatt, D., Gitelson, A., Brando, V.E., Schaepman, M., 2012. Review of constituent retrieval in optically deep and complex waters from satellite imagery. Remote Sens. Environ. 118, 116–126.
Odriozola, A.L., Varela, R., Hu, C., Astor, Y., Lorenzoni, L., Müller-Karger, F.E., 2007. On the absorption of light in the Orinoco River plume. Cont. Shelf Res. 27, 1447–1464.
Ody, A., Novoa, S., Doxaran, D., 2016. Multi-conditional algorithm for multi-sensor remote sensing of suspended particulate matter in low to highly turbid waters. Ocean Optics XXIII meeting. Victoria, British Columbia, Canada.
Officer, C.B., Biggs, R.B., Taft, J.L., Cronin, L.E., Tyler, M.A., Boynton, W.R., 1984. Chesapeake Bay Anoxia: origin, development, and significance. Science 223, 22–27.
Ohde, T., Mohrholz, V., 2011. Interannual variability of sulphur plumes off the Namibian coast. Int. J. Remote Sens. 32, 9327–9342.
Ohde, T., Siegel, H., Reißmann, J., Gerth, M., 2007. Identification and investigation of sulphur plumes along the Namibian coast using the MERIS sensor. Cont. Shelf Res. 27, 744–756.
Oliver, J., 2005. Vibrio vulnificus. In: Belkin, S., Colwell, R. (Eds.), Oceans and Health: Pathogens in the Marine Environment. Springer, US, pp. 253–276.
Olsen, C.R., Cutshall, N.H., Larsen, I.L., 1982. Pollutant—particle associations and dynamics in coastal marine environments: a review. Mar. Chem. 11, 501–533.
Ondrusek, M., Stengel, E., Kinkade, C.S., Vogel, R.L., Keegstra, P., Hunter, C., Kim, C., 2012. The development of a new optical total suspended matter algorithm for the Chesapeake Bay. Remote Sens. Environ. 119, 243–254.
Pachepsky, Y.A., Shelton, D.R., 2011. Escherichia Coli and Fecal Coliforms in Freshwater and Estuarine Sediments. Crit. Rev. Environ. Sci. Technol. 41, 1067–1110.
Park, Y.-J., Ruddick, K., 2005. Model of remote-sensing reflectance including bidirectional effects for case 1 and case 2 waters. Appl. Opt. 44, 1236–1249.
Pegau, W.S., Gray, D., Zaneveld, J.R.V., 1997. Absorption and attenuation of visible and near-infrared light in water: dependence on temperature and salinity. Appl. Opt. 36, 6035–6046.
Peralta, G., Pérez-Lloréns, J.L., Hernández, I., Vergara, J.J., 2002. Effects of light availability on growth, architecture and nutrient content of the seagrass Zostera noltii Hornem. J. Exp. Mar. Biol. Ecol. 269, 9–26.
Pettersson, L., Pozdnyakov, D., 2013. Potential of remote sensing for identification, delineation, and monitoring of harmful algal blooms. Monitoring of Harmful Algal Blooms (pp. 49–111): Springer, Berlin Heidelberg.
Petus, C., Chust, G., Gohin, F., Doxaran, D., Froidefond, J.-M., Sagarminaga, Y., 2010. Estimating turbidity and total suspended matter in the Adour River plume (South Bay of Biscay) using MODIS 250-m imagery. Cont. Shelf Res. 30, 379–392.
Petzold, T.J., 1972. Volume scattering functions for selected ocean waters, SIO Reference, report number, pp. 72–78.
Piskozub, J., McKee, D., 2011. Effective scattering phase functions for the multiple scattering regime. Opt. Express 19, 4786–4794.
Pope, R.M., Fry, E.S., 1997. Absorption spectrum (380–700 nm) of pure water. II. Integrating cavity measurements. Appl. Opt. 36, 8710–8723.
Preisendorfer, R.W., 1986. Secchi disk science: visual optics of natural waters1. Limnol. Oceanogr. 31, 909–926.
Rabalais, N.N., Turner, R.E., 2001. Hypoxia in the Northern Gulf of Mexico: Description, Causes and Change. Coastal Hypoxia: Consequences for Living Resources and Ecosystems (pp. 1–36): American Geophysical Union.
Reifel, K.M., Johnson, S.C., DiGiacomo, P.M., Mengel, M.J., Nezlin, N.P., Warrick, J.A., Jones, B.H., 2009. Impacts of stormwater runoff in the Southern California Bight: Relationships among plume constituents. Cont. Shelf Res. 29, 1821–1835.

Reifel, K.M., Swan, B.K., Ehrhardt, C.J., Jones, B.H., 2010. Optical characterization of a precipitation event in a moderately hypersaline lake. Geophys. Res. Lett. 37, L21603.
Reynolds, R.A., Stramski, D., Mitchell, B.G., 2001. A chlorophyll-dependent semi-analytical reflectance model derived from field measurements of absorption and backscattering coefficients within the Southern Ocean. J. Geophys. Res. 106, 7125–7138.
Rochelle-Newall, E.J., Fisher, T.R., 2002a. Chromophoric dissolved organic matter and dissolved organic carbon in Chesapeake Bay. Mar. Chem. 77, 23–41.
Rochelle-Newall, E.J., Fisher, T.R., 2002b. Production of chromophoric dissolved organic matter fluorescence in marine and estuarine environments: an investigation into the role of phytoplankton. Mar. Chem. 77, 7–21.
Rodríguez-Guzmán, V., Gilbes-Santaella, F., 2009. Using MODIS 250 m imagery to estimate total suspended sediment in a tropical open bay. Int. J. Syst. Appl. Eng. Dev. 3, 36–44.
Roesler, C.S., Boss, E., 2003. Spectral beam attenuation coefficient retrieved from ocean color inversion. Geophys. Res. Lett. 30, 1468.
Roesler, C.S., Perry, M.J., 1995. In situ phytoplankton absorption, fluorescence emission, and particulate backscattering spectra determined from reflectance. J. Geophys. Res. 100, 13279–13294.
Röttgers, R., Doerfer, R., McKee, D., Schönfeld, W., 2010. The Water Optical Properties Processor (WOPP): Pure water spectral absorbtion, scattering, and real part of refractive index model, Algorithm Technical Basis Document, report number, WR D6.
Röttgers, R., McKee, D., Utschig, C., 2014. Temperature and salinity correction coefficients for light absorption by water in the visible to infrared spectral region. Opt. Express 22, 25093–25108.
Roy, S., Blouin, F., Jacques, A., Therriault, J.-C., 2008. Absorption properties of phytoplankton in the Lower Estuary and Gulf of St. Lawrence (Canada). Can. J. Fish. Aquat. Sci. 65, 1721–1737.
Sathyendranath, S., Stuart, V., Irwin, B.D., Maass, H., Savidge, G., Gilpin, L., Platt, T., 1999. Seasonal variations in bio-optical properties of phytoplankton in the Arabian Sea. Deep Sea Res. Part II 46, 633–653.
Schaeffer, B.A., Hagy, J.D., Conmy, R.N., Lehrter, J.C., Stumpf, R.P., 2012. An approach to developing numeric water quality criteria for coastal waters using the SeaWiFS satellite data record. Environ. Sci. Technol. 46, 916–922.
Schofield, O., Grzymski, J., Bissett, W.P., Kirkpatrick, G.J., Millie, D.F., Moline, M., Roesler, C.S., 1999. Optical monitoring and forecasting systems for harmful algal blooms: possibility or pipe dream? J. Phycol. 35, 1477–1496.
Schofield, O., Kerfoot, J., Mahoney, K., Moline, M., Oliver, M., Lohrenz, S., Kirkpatrick, G., 2006. Vertical migration of the toxic dinoflagellate Karenia brevis and the impact on ocean optical properties. J. Geophys. Res. 111, C06009.
Seegers, B.N., Birch, J.M., Marin, R., Scholin, C.A., Caron, D.A., Seubert, E.L., Howard, M.D.A., Robertson, G.L., Jones, B.H., 2015. Subsurface seeding of surface harmful algal blooms observed through the integration of autonomous gliders, moored environmental sample processors, and satellite remote sensing in southern California. Limnol. Oceanogr. 60, 754–764.
Shcherbak, S.S., Lavrova, O.Y., Mityagina, M.I., Bocharova, T.Y., Krovotyntsev, V.A., Ostrovskii, A.G., 2008. Multisensor satellite monitoring of seawater state and oil pollution in the northeastern coastal zone of the Black Sea. Int. J. Remote Sens. 29, 6331–6345.
Shen, F., Verhoef, W., Zhou, Y., Salama, M.S., Liu, X., 2010. Satellite estimates of wide-range suspended sediment concentrations in Changjiang (Yangtze) estuary using MERIS data. Estuaries Coasts 33, 1420–1429.
Sherer, B.M., Miner, J.R., Moore, J.A., Buckhouse, J.C., 1992. Indicator bacterial survival in stream sediments. J. Environ. Qual. 21, 591–595.
Shi, W., Wang, M., 2007. Detection of turbid waters and absorbing aerosols for the MODIS Ocean color data processing. Remote Sens. Environ. 110, 149–161.
Shi, W., Wang, M., 2009. Green macroalgae blooms in the Yellow Sea during the spring and summer of 2008. J. Geophys. Res. 114.
Shi, W., Wang, M., 2014. Ocean reflectance spectra at the red, near-infrared, and shortwave infrared from highly turbid waters: a study in the Bohai Sea, Yellow Sea, and East China Sea. Limnol. Oceanogr. 59, 427–444.
Sicot, G., Lennon, M., Miegebielle, V., Dubucq, D., 2015. Estimation of the Thickness and Emulsion Rate of Oil Spilled at Sea Using Hyperspectral Remote Sensing Imagery in the Swir Domain. ISPRS – Int. Arch. Photogram., Remote Sens. Spatial Inf. Sci. XL-3/W3, 445–450.
Slade, W.H., Boss, E., 2015. Spectral attenuation and backscattering as indicators of average particle size. Appl. Opt. 54, 7264–7277.
Smith, R.C., Baker, K.S., 1981. Optical properties of the clearest natural waters (200–800 nm). Appl. Opt. 20, 177–184.
Snyder, W.A., Arnone, R.A., Davis, C.O., Goode, W., Gould, R.W., Ladner, S., Lamela, G., Rhea, W.J., Stavn, R., Sydor, M., Weidemann, A., 2008. Optical scattering and backscattering by organic and inorganic particulates in U.S. coastal waters. Appl. Opt. 47, 666–677.
Son, S., Wang, M., 2012. Water properties in Chesapeake Bay from MODIS-aqua measurements. Remote Sens. Environ. 123, 163–174.
Sørensen, K., Severinsen, G., Künitzer, A., 2002. Remote sensing's contribution to evaluating eutrophication in marine and coastal waters, report number, 79.
Stedmon, C.A., Markager, S., Kaas, H., 2000. Optical properties and signatures of chromophoric dissolved organic matter (CDOM) in Danish coastal waters. Estuar. Coast. Shelf Sci. 51, 267–278.
Steel, E.A., Neuhausser, S., 2002. Comparison of methods for measuring visual water clarity. J. N. Am. Benthol. Soc. 21, 326–335.
Steinberg, D.K., Nelson, N.B., Carlson, C.A., Prusak, A., 2004. Production of chromophoric dissolved organic matter (CDOM) in the open ocean by zooplankton and the colonial cyanobacterium Trichodesmium spp. Mar. Ecol. Prog. Ser. 267, 45–56.
Stramska, M., Stramski, D., 2005. Effects of a nonuniform vertical profile of chlorophyll concentration on remote-sensing reflectance of the ocean. Appl. Opt. 44, 1735–1747.
Stramska, M., Stramski, D., Cichocka, M., Cieplak, A., Woźniak, S.B., 2008. Effects of atmospheric particles from Southern California on the optical properties of seawater. J. Geophys. Res. 113, C08037.
Stramski, D., Babin, M., Woźniak, S.B., 2007. Variations in the optical properties of terrigenous mineral-rich particulate matter suspended in seawater. Limnol. Oceanogr. 52, 2418–2433.
Stramski, D., Boss, E., Bogucki, D., Voss, K.J., 2004a. The role of seawater constituents in light backscattering in the ocean. Prog. Oceanogr. 61, 27–56.
Stramski, D., Bricaud, A., Morel, A., 2001. Modeling the inherent optical properties of the ocean based on the detailed composition of the planktonic community. Appl. Opt. 40, 2929–2945.
Stramski, D., Reynolds, R.A., Babin, M., Kaczmarek, S., Lewis, M.R., Röttgers, R., Sciandra, A., Stramska, M., Twardowski, M.S., Franz, B.A., 2008. Relationships between the surface concentration of particulate organic carbon and optical properties in the eastern South Pacific and eastern Atlantic Oceans. Biogeosciences 5, 171–201.
Stramski, D., Reynolds, R.A., Kaczmarek, S., Uitz, J., Zheng, G., 2015. Correction of pathlength amplification in the filter-pad technique for measurements of particulate absorption coefficient in the visible spectral region. Appl. Opt. 54, 6763–6782.
Stramski, D., Reynolds, R.A., Kahru, M., Mitchell, B.G., 1999. Estimation of particulate organic carbon in the ocean from satellite remote sensing. Science 285, 239–242.
Stramski, D., Tegowski, J., 2001. Effects of intermittent entrainment of air bubbles by breaking wind waves on ocean reflectance and underwater light field. J. Geophys. Res. 106, 31345–31360.
Stramski, D., Woźniak, S.B., Flatau, P.J., 2004b. Optical properties of Asian mineral dust suspended in seawater. Limnol. Oceanogr. 49, 749–755.
Stumpf, R.P., Tomlinson, M.C., 2005. Remote sensing of harmful algal blooms. Remote sensing of coastal aquatic environments (pp. 277–296): Springer.
Sullivan, J.M., Twardowski, M.S., Zaneveld, J.R.V., Moore, C.M., Barnard, A.H., Donaghay, P.L., Rhoades, B., 2006. Hyperspectral temperature and salt dependencies of absorption by water and heavy water in the 400–750 nm spectral range. Appl. Opt. 45, 5294–5309.
Sun, D., Li, Y., Wang, Q., Gao, J., Lv, H., Le, C., Huang, C., 2009. Light scattering properties and their relation to the biogeochemical composition of turbid productive waters: a case study of Lake Taihu. Appl. Opt. 48, 1979–1989.
Sydor, M., 2006. Use of hyperspectral remote sensing reflectance in extracting the spectral volume absorption coefficient for phytoplankton in coastal water: remote sensing relationships for the inherent optical properties of coastal water. J. Coastal Res. 22, 587–601.
Sydor, M., Wolz, B.D., Thralow, A.M., 2002. Spectral analysis of bulk reflectance from coastal waters: deconvolution of diffuse spectra due to scattering and absorption by coastal water. J. Coastal Res. 18, 352–361.
Takeda, S., Nimura, Y., Hirano, R., 1991. Optical, biological, and chemical properties of Aoshio, hypoxic milky blue-green water, observed at the head of Tokyo Bay. J. Oceanogr. Soc. Jpn. 47, 126–137.
Terrill, E.J., Melville, W.K., Stramski, D., 2001. Bubble entrainment by breaking waves and their influence on optical scattering in the upper ocean. J. Geophys. Res. 106, 16815–16823.
Tiffany, M.A., Ustin, S.L., Hurlbert, S.H., 2007. Sulfide irruptions and gypsum blooms in the Salton Sea as detected by satellite imagery, 1979–2006. Lake Reservoir Manage. 23, 637–652.
Tomlinson, M., Wynne, T., Stumpf, R., 2009. An evaluation of remote sensing techniques for enhanced detection of the toxic dinoflagellate, Karenia brevis. Remote Sens. Environ. 113, 598–609.
Turner, R.E., Rabalais, N.N., Justic, D., 2008. Gulf of Mexico hypoxia: alternate states and a legacy. Environ. Sci. Technol. 42, 2323–2327.
Twardowski, M.S., Claustre, H., Freeman, S.A., Stramski, D., Huot, Y., 2007. Optical backscattering properties of the "clearest" natural waters. Biogeosciences 4, 1041–1058.
Twardowski, M.S., Donaghay, P.L., 2002. Photobleaching of aquatic dissolved materials: absorption removal, spectral alteration, and their interrelationship. J. Geophys. Res. 107, 3091.
Tyler, J.E., 1958. Radiance distribution as a function of depth in the submarine environment, SIO Reference, report number, pp. 58–25.
Tzortziou, M., Subramaniam, A., Herman, J.R., Gallegos, C.L., Neale, P.J., Harding, L.W., 2007. Remote sensing reflectance and inherent optical properties in the mid Chesapeake Bay. Estuar. Coast. Shelf Sci. 72, 16–32.
Uncles, R., Stephens, J., Woodrow, T., 1988. Seasonal cycling of estuarine sediment and contaminant transport. Estuaries 11, 108–116.
USEPA, 1993. Method 180.1 Determination of turbidity by nephelometry (revision 2.0). In: J.W. O'Dell (Ed.), Methods for the Determination of Inorganic Substances in Environmental Samples (EPA/600/R-93/100) (p. 10). Cincinnati, Ohio: U. S. Environmental Proctection Agency.
van de Hulst, H.C., 1957. Light Scattering by Small Particles. Wiley, New York.
Volten, H., De Haan, J., Hovenier, J., Schreurs, R., Vassen, W., Dekker, A., Hoogenboom, H., Charlton, F., Wouts, R., 1998. Laboratory measurements of angular distributions of light scattered by phytoplankton and silt. Limnol. Oceanogr. 43, 1180–1197.
Voss, K.J., Morel, A., Antoine, D., 2007. Detailed validation of the bidirectional effect in various Case 1 waters for application to ocean color imagery. Biogeosciences 4, 781–789.
Walker, N.D., 1996. Satellite assessment of Mississippi River plume variability: Causes and predictability. Remote Sens. Environ. 58, 21–35.
Wang, G., Cao, W., Yang, D., Xu, D., 2008. Variation in downwelling diffuse attenuation coefficient in the northern South China Sea. Chin. J. Oceanol. Limnol. 26, 323–333.
Wang, M., Shi, W., 2007. The NIR-SWIR combined atmospheric correction approach for MODIS ocean color data processing. Opt. Express 15, 15722–15733.

Wang, M., Son, S., Harding, L.W., 2009a. Retrieval of diffuse attenuation coefficient in the Chesapeake Bay and turbid ocean regions for satellite ocean color applications. J. Geophys. Res. 114.
Wang, M., Son, S., Shi, W., 2009b. Evaluation of MODIS SWIR and NIR-SWIR atmospheric correction algorithms using SeaBASS data. Remote Sens. Environ. 113, 635–644.
Wang, S.Q., Ishizaka, J., Yamaguchi, H., Tripathy, S.C., Hayashi, M., Xu, Y.J., Mino, Y., Matsuno, T., Watanabe, Y., Yoo, S.J., 2014. Influence of the Changjiang River on the light absorption properties of phytoplankton from the East China Sea. Biogeosciences 11, 1759–1773.
Waters, K.J., 1995. Effects of Raman scattering on the water-leaving radiance. J. Geophys. Res. 100, 13151–13161.
Weeks, S.J., Currie, B., Bakun, A., Peard, K.R., 2004. Hydrogen sulphide eruptions in the Atlantic Ocean off southern Africa: implications of a new view based on SeaWiFS satellite imagery. Deep Sea Res. Part I 51, 153–172.
Wei, J., Lee, Z., 2015. Retrieval of phytoplankton and colored detrital matter absorption coefficients with remote sensing reflectance in an ultraviolet band. Appl. Opt. 54, 636–649.
Wernand, M.R., 2010. On the history of the Secchi disc.
Westberry, T.K., Boss, E., Lee, Z., 2013. Influence of Raman scattering on ocean color inversion models. Appl. Opt. 52, 5552–5561.
Wozniak, B., Wozniak, S.B., Tyszka, K., Ostrowska, M., Majchrowski, R., Ficek, D., Dera, J., 2005. Modelling the light absorption properties of particulate matter forming organic particles suspended in seawater. Part 2. Modelling results. Oceanologia 47, 621–662.
Woźniak, S.B., Stramski, D., 2004. Modeling the optical properties of mineral particles suspended in seawater and their influence on ocean reflectance and chlorophyll estimation from remote sensing algorithms. Appl. Opt. 43, 3489–3503.
Woźniak, S.B., Stramski, D., Stramska, M., Reynolds, R.A., Wright, V.M., Miksic, E.Y., Cichocka, M., Cieplak, A.M., 2010. Optical variability of seawater in relation to particle concentration, composition, and size distribution in the nearshore marine environment at Imperial Beach, California. J. Geophys. Res. 115, C08027.
Wynne, T.T., Stumpf, R.P., Tomlinson, M.C., Warner, R.A., Tester, P.A., Dyble, J., Fahnenstiel, G.L., 2008. Relating spectral shape to cyanobacterial blooms in the Laurentian Great Lakes. Int. J. Remote Sens. 29, 3665–3672.
Xi, H., Larouche, P., Michel, C., Tang, S., 2015. Beam attenuation, scattering and backscattering of marine particles in relation to particle size distribution and composition in Hudson Bay (Canada). J. Geophys. Res. 120, 3286–3300.
Xi, H., Larouche, P., Tang, S., Michel, C., 2013. Seasonal variability of light absorption properties and water optical constituents in Hudson Bay, Canada. J. Geophys. Res. 118, 3087–3102.
Xing, X., Zhao, D., Liu, Y., Yang, J., Wang, L., 2008. In situ determination of sun-induced chlorophyll a fluorescence quantum yield in the North China Sea. Int. J. Remote Sens. 29, 851–865.
Xiong, X., Barnes, W.L., 2003. Early on-orbit calibration results from Aqua MODIS. Vol. 4881 (pp. 327–336).
Xiong, X., Butler, J., Chiang, K., Efremova, B., Fulbright, J., Lei, N., McIntire, J., Oudrari, H., Sun, J., Wang, Z., Wu, A., 2014. VIIRS on-orbit calibration methodology and performance. J. Geophys. Res.: Atmos. 119, 5065–5078.
Yacobi, Y.Z., Alberts, J.J., Takacs, M., McElvaine, M., 2003. Absorption spectroscopy of colored dissolved organic carbon in Georgia (USA) rivers: the impact of molecular size distribution, Vol. 62, p. 6.
Yang, Q., Stramski, D., He, M.-X., 2013. Modeling the effects of near-surface plumes of suspended particulate matter on remote-sensing reflectance of coastal waters. Appl. Opt. 52, 359–374.
Yoder, J.A., Antoine, D., Castillo, C.E.D., Evans, R.H., Mobley, C., Sarmiento, J.L., Sathyendranath, S., Schueler, C.F., Siegel, D.A., Wilson, C., 2011. Assessing the requirements for sustained ocean color research and operations, report number, 978-0-309-21044-7.
Zaneveld, J.R.V., 1982. Remotely sensed reflectance and its dependence on vertical structure: a theoretical derivation. Appl. Opt. 21, 4146–4150.
Zawada, D.G., Hu, C., Clayton, T., Chen, Z., Brock, J.C., Muller-Karger, F.E., 2007. Remote sensing of particle backscattering in Chesapeake Bay: a 6-year SeaWiFS retrospective view. Estuar. Coast. Shelf Sci. 73, 792–806.
Zhang, M., Tang, J., Dong, Q., Song, Q., Ding, J., 2010. Retrieval of total suspended matter concentration in the Yellow and East China Seas from MODIS imagery. Remote Sens. Environ. 114, 392–403.
Zhang, T., Fell, F., 2007. An empirical algorithm for determining the diffuse attenuation coefficient Kd in clear and turbid waters from spectral remote sensing reflectance. Limnol. Oceanogr.: Methods 5, 457–462.
Zhang, X., Hu, L., He, M.-X., 2009a. Scattering by pure seawater: Effect of salinity. Opt. Express 17, 5698–5710.
Zhang, X., Lewis, M., Johnson, B., 1998. Influence of bubbles on scattering of light in the ocean. Appl. Opt. 37, 6525–6536.
Zhang, Y., van Dijk, M.A., Liu, M., Zhu, G., Qin, B., 2009b. The contribution of phytoplankton degradation to chromophoric dissolved organic matter (CDOM) in eutrophic shallow lakes: Field and experimental evidence. Water Res. 43, 4685–4697.
Zhang, Y.L., 2008. Optical Properties of Lake Taihu and Radiative Transfer Simulation. In: In: Qin, B. (Ed.), Lake Taihu, China Vol. 87. Springer, Netherlands, pp. 69–113.
Zheng, G., DiGiacomo, P.M., Kaushal, S.S., Yuen-Murphy, M.A., Duan, S., 2015a. Evolution of sediment plumes in the Chesapeake bay and implications of climate variability. Environ. Sci. Technol. 49, 6494–6503.
Zheng, G., Stramski, D., 2013. A model based on stacked-constraints approach for partitioning the light absorption coefficient of seawater into phytoplankton and nonphytoplankton components. J. Geophys. Res. 118, 2155–2174.
Zheng, G., Stramski, D., Reynolds, R.A., 2014. Evaluation of the Quasi-Analytical Algorithm for estimating the inherent optical properties of seawater from ocean color: comparison of Arctic and lower-latitude waters. Remote Sens. Environ. 155, 194–209.
Zheng, G., Stramski, D., DiGiacomo, P.M., 2015b. A model for partitioning the light absorption coefficient of natural waters into phytoplankton, nonalgal particulate, and colored dissolved organic components: a case study for the Chesapeake Bay. J. Geophys. Res. 120, 2601–2621.